A Study of Radiative Charged Current Interactions in *ep* Collisions

Thesis submitted in accordance with the requirements of the
University of Liverpool for the degree of Doctor of Philosophy

by

Anna Lucy Burrage

December 2000

Oliver Lodge Laboratory
University of Liverpool

A Study of Radiative Charged Current Interactions in *ep* Collisions

Anna Lucy Burrage

Abstract

Using data from the H1 experiment at HERA, measurements have been made of the inclusive charged current cross sections and the exclusive radiative charged current channel. The data were taken between 1994 and 2000 with centre of mass energies of 300 GeV and 320 GeV, using proton and electron or positron colliding beams. The data sample corresponds to a total integrated luminosity of 115 pb^{-1}.

Measurements of the single and double differential charged current cross-sections, $\frac{d\sigma}{dx}$, $\frac{d\sigma}{dQ^2}$ and $\frac{d^2\sigma}{dxdQ^2}$, respectively, are obtained with different beam energies and types at the highest possible of values Q^2 and x. Calculations of the Standard Model of particle physics are compared with these data and found to be in agreement. Effects on these cross sections due to changes in beam energy and lepton type are observed.

The radiative charged current cross sections are measured for the first time at H1 and their significance with respect to the anomalous couplings of the WWγ vertex, $\Delta\kappa$ and λ, is discussed. The results presented are again shown to be in full agreement with the predictions from the Standard Model.

Authors Contribution

The analyses presented within this thesis are part of the Physics programme of the 'High p_t, high Q^2' (HiP) working group of the H1 Experiment at DESY in Hamburg, Germany. The data shown were taken by the H1 Collaboration during the years 1994 - 2000. All members of the Collaboration were involved in the data accumulation process.

The majority of the data analysis presented in this thesis is the author's own work. However, certain parts of the Charged Current (CC) analysis were a joint effort by the author and several colleagues, or - with respect to the CC results pre-1998 - the work of a group not including the author. The CC analysis from 1998 onwards has resulted in several publications, including a conference paper for the EPS99 Conference, Tampere, Finland [47]. The author's contribution to this analysis was the compilation of the data sample, calculation of the trigger efficiencies and studies of the background rejection. At the time of writing, this analysis is being prepared for publication in the European Physics Journal C [48].

A preliminary analysis of CC data taken in 1999-2000 was published in a conference paper for the ICHEP 2000 Conference in Osaka, Japan [9].

The radiative CC analysis is entirely the author's own work and is at present being prepared for publication.

The author was deeply involved with the day-to-day running of the H1 experiment. She has been an "expert on call" for the Forward Track Detector, a member of the shift crew and was responsible for the data quality monitoring for the HiP working group.

Contents

Chapter 1

Physics at HERA

HERA is an electron[1] - proton collider. It has been designed and used primarily to probe the quark and gluon structure of the proton which is now, partly due to endeavours at HERA, understood to an increasing degree [1] [2] [3] [4] [5] [6]. At HERA, the process which is experimentally observed and is of primary interest for measurements of proton structure is that of deep-inelastic lepton proton scattering (DIS). This chapter explains DIS processes: the kinematic framework within which they are described and the theories and equations which characterise and quantify the different types of DIS interactions.

1.1 Deep-Inelastic Scattering

A deep-inelastic scattering (DIS) event is characterised by an incoming lepton scattering off a proton via the exchange of a vector boson. A schematic diagram of this process is shown in figure 1.1.

The kinematics of a typical DIS event are parameterised in terms of the following quantities:

- Q^2 4 momentum transfer squared:

$$Q^2 = -q^2 = -(k - k')^2 \tag{1.1}$$

- x Björken-x, the fraction of the proton's momentum carried by the struck

---

[1] Electron denotes electron or positron throughout this thesis, unless otherwise specified.

quark:

$$x = \frac{Q^2}{2p.q} \tag{1.2}$$

- y Inelasticity variable, the fractional energy loss of the lepton in the proton rest frame:

$$y = \frac{p.q}{p.k} \tag{1.3}$$

where k (p) and k' (p') are the 4-momenta of the incoming and outgoing lepton (proton) and $q = k - k'$, shown in fig. 1.1. Both x and y are dimensionless variables. Q^2 has dimensions of energy squared. Natural units are used throughout this thesis.

Only two of the above variables can be independent. They are related by

$$Q^2 = sxy \tag{1.4}$$

and

$$W^2 = Q^2\left(\frac{1-x}{x}\right) \tag{1.5}$$

where s is the square of the centre of mass (COM) energy of the ep collision (neglecting radiation effects) and W is the invariant mass of the final state system (the scattered lepton and hadronic final state in fig. 1.1).

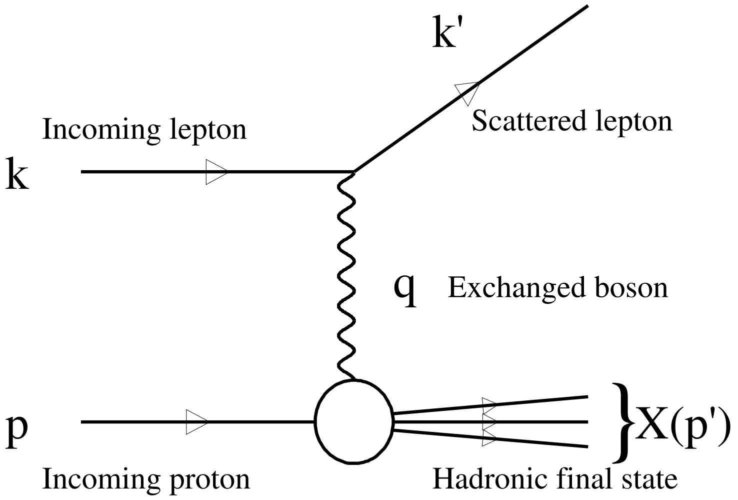

Figure 1.1: Feynman diagram for DIS.

A neutral current (NC) DIS process involves the exchange of a photon (γ) or a Z^0 boson. The final state contains a scattered electron and a hadronic system (X). At low values of Q^2, Z^0 boson exchange is highly suppressed with respect to γ exchange due to the large mass of the Z^0 boson (91.3 GeV [7]). A charged current (CC) interaction involves the exchange of a $W^{\pm}$ boson (mass 80.4 GeV [8]); the scattered lepton is an electron neutrino. The Feynman diagram for CC scattering is shown in fig. 1.2. On rare occasions, the $W^{\pm}$ boson exchanged during a CC process will itself emit a real photon. Radiation may also be emitted from the incoming or outgoing quarks or leptons. These processes are called 'radiative CC' and are described in more detail in section 1.2.

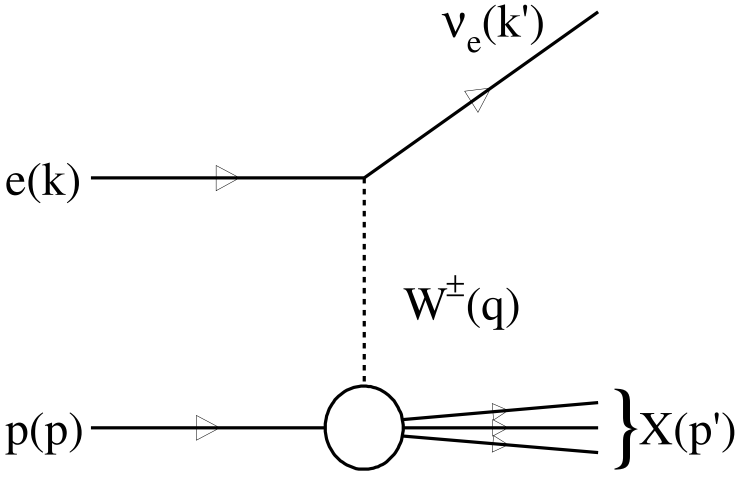

Figure 1.2: Feynman diagram for CC scattering.

Structure Functions

Structure functions relate to the properties and composition of the proton [10]. If the virtuality of the exchanged boson is high (i.e. $Q^2 \gtrsim 1$ GeV^2) then it is possible to begin to examine the substructure of the proton. The larger the Q^2 of the DIS interaction, the deeper the proton is probed and the higher the resolution of the contents.

The substructure of the proton may be expressed in terms of a minimum number of 'structure functions'. In the Quark Parton Model (QPM), where a parton is a point-like constituent of the proton, the structure functions are related to Q^2 independent parton distribution functions (PDFs), denoted $f(x)$. Quantum Chromodynamics (QCD) predicts the Q^2 evolution of the PDFs at fixed x and, hence, the PDFs are denoted $f(x, Q^2)$. The $F_1(x, Q^2)$ and $F_2(x, Q^2)$ structure functions are related to the cross sections for longitudinally and transversely polarised particles, and $F_3(x, Q^2)$ is related to that for parity violating processes.

Quark Parton Model

An intuitive understanding of the structure functions is obtained by considering the QPM in which quarks are the only constituents of the proton, and interact only electromagnetically or weakly. Each constituent carries a fraction x of the proton's momentum. The PDF describes the probability that the struck parton carries a proportion x of the total momentum p. The structure functions can be written as a charge weighted sum over all the quark distributions in the proton. Naively, one might expect that each of the 3 valence quarks carries an average of one third of the total momentum.

This simplisitic treatment of the partons in the QPM was motivated by the observation at early SLAC experiments [11] of *scaling* in which the structure functions depend only on x and not on the scale, Q^2, at which the proton is probed. However, detailed measurements at pre-HERA experiments [12] [13] and then H1 [3] [5] [14] and ZEUS [4] [6] have shown that, although scaling is observed over several decades in Q^2 for values of $x \sim 0.2$, a Q^2 dependence is observed at smaller and larger x. The QPM does not give an explanation for the observed scaling violations therefore a more advanced model is required.

Quantum Chromodynamics

QCD is the theory of the strong interaction and consequently describes a more sophisticated model of partonic structure. QCD describes a model of a proton containing the valence quarks surrounded by a cloud of gluons - the electrically neutral gauge bosons - and sea-quarks - the quark anti-quark pairs created by the gluons. Gluons are the strong interaction equivalent of photons in the electromagnetic interaction and are massless. They couple to the colour charge carried by other partons within the proton.

The self-interaction of the gluons leads to the strong variation of the coupling, $\alpha_s(Q^2)$, with the scale. At low momentum transfer (or large distance scales) the coupling becomes large. This leads to *confinement*, such that quarks may only exist within bound states of hadrons. At high momentum transfer (small distance scales) the coupling becomes small enough that the quarks behave as almost free particles, interacting with each other through the exchange of gluons. The quarks in the proton radiate gluons, leading to an increase in the effective number of partons visible with increasing Q^2, and a decrease in the average momentum carried by each parton.

Although QCD does not give absolute predictions for PDFs, the Q^2 evolution of the structure functions can be calculated in the HERA kinematic range using the DGLAP evolution equations, named after prominent QCD theorists [15]. These equations use the quark and gluon PDFs at a starting scale as input and predict the form of the PDFs, and hence structure functions, at a new scale. The DGLAP equations at HERA Q^2 scales agree well with the measurements made using data taken by H1, showing a logarithmic rise of F_2 with Q^2 at low x and fall of F_2 with Q^2 at high x. All QCD processes may be factorised into hard interactions, calculable in perturbative QCD (pQCD), and the PDFs for the initial state particles. These PDFs, although incalculable in pQCD, are universal for all hard interactions. That is, once measured from the data for one interaction, they can be used to make predictions for many others. The PDFs are therefore transportable between different types of experiment, i.e. *ep* or *pp*. Cross section calculations in this thesis use PDFs extracted from fits to data from many experiments.

1.1.1 The DIS Cross Section

DIS cross sections contain three types of term which describe different aspects of DIS interactions. These are **(a)** coupling terms, **(b)** propagator terms and **(c)** proton structure function terms. They are discussed here in the context of describing the behaviour of the cross section measurement made in this thesis.

The Born (first order) cross section equation for $ep \rightarrow \nu X$ (CC) scattering is

$$\frac{\mathrm{d}\sigma_{CC}^{e\pm p}}{\mathrm{d}x\mathrm{d}Q^2} = \frac{G_F^2 M_W^2}{2\pi x}\left(\frac{1}{M_W^2+Q^2}\right)^2 \phi_{CC}^{\pm}(x,Q^2) \tag{1.6}$$

where

- G_F is the Fermi coupling constant, $G_F^2 = \frac{\pi^2\alpha^2}{2\sin^4\theta_W M_W^4}$;
- M_W is the mass of the $W^\pm$ boson;
- $\sin\theta_W$ is the Weinberg mixing angle;
- α is the fine structure constant, $\alpha = e^2/4\pi$, and
- $\phi_{CC}^{\pm}$ is a combination of the proton structure function terms , $\tilde{W}_L$, $\tilde{W}_2$ and $x\tilde{W}_3$, and a function of the inelasticity, $Y_\pm = 1 + (1 \pm y^2)$,

$$\phi_{CC}^{\pm} = Y_+ \tilde{W}_2^{\pm}(x,Q^2) + y^2 \tilde{W}_L^{\pm}(x,Q^2) \mp Y_- x\tilde{W}_3^{\pm}(x,Q^2). \tag{1.7}$$

The equivalent Born cross section equation for $ep \rightarrow eX$ (NC) scattering is

$$\frac{\mathrm{d}\sigma_{NC}^{e\pm p}}{\mathrm{d}x\mathrm{d}Q^2} = \frac{2\pi\alpha^2}{x}\left[\left(\frac{1}{Q^4}\right)Y_+F_2 + \left(\frac{1}{Q^2+M_Z^2}\right)^2 a_e^2\kappa_w^2 Y_+ F_2^Z \mp 2\left(\frac{1}{Q^2(Q^2+M_Z^2)}\right)a_e\kappa_w Y_- xF_3^{\gamma Z}\right] \tag{1.8}$$

where

- M_Z is the mass of the Z^0 boson
- F_2, F_2^Z and $xF_3^{\gamma Z}$ are the structure functions relating to γ exchange, Z^0 exchange and γZ interference respectively,
- a_e is the axial vector coupling of the electron and κ_w is a function of the Weinberg angle:

$$\kappa_w = \frac{1}{4\sin^2\theta_W\cos^2\theta_W}. \tag{1.9}$$

The longitudinal component of the structure function (W_L or F_L) only becomes significant at high y (see equation 1.7) and can therefore be neglected within these derivations which relate to the low y domain. The cross sections equations 1.6 and 1.8 can be compared with respect to their component parts and conclusions can be drawn about the influence of each of the terms on the overall cross sections:

(a) Coupling terms

The similarity between the vertex coupling terms for CC and NC (the first term of equations 1.6 and 1.8) becomes apparent if the Fermi coupling constant G_F is expressed in terms of g, the electroweak coupling constant

$$G_F = \frac{g^2}{4\sqrt{2}M_W^2}. \tag{1.10}$$

If the expressions for e and g are substituted into the first terms of equations 1.6 and 1.8, the terms take the following form:

$$\text{CC} \quad \frac{G_F^2 M_W^4}{2\pi x} \Rightarrow \frac{g^4}{64\pi x} \qquad\qquad \text{NC} \quad \frac{2\pi\alpha}{x} \Rightarrow \frac{e^4}{8\pi x} \tag{1.11}$$

and e and g are related by

$$g^2 = \frac{e^2}{\sin^2\theta_W} \approx 4e^2. \tag{1.12}$$

This similarity indicates that in the high Q^2 region, $Q^2 \sim M_W^2$ or M_Z^2, it is expected that the cross sections are of the same order of magnitude. This feature of the cross sections is shown in fig. 1.3, the differential cross sections for NC and CC as a function of Q^2, where for high Q^2 the cross sections are indeed similar in magnitude.

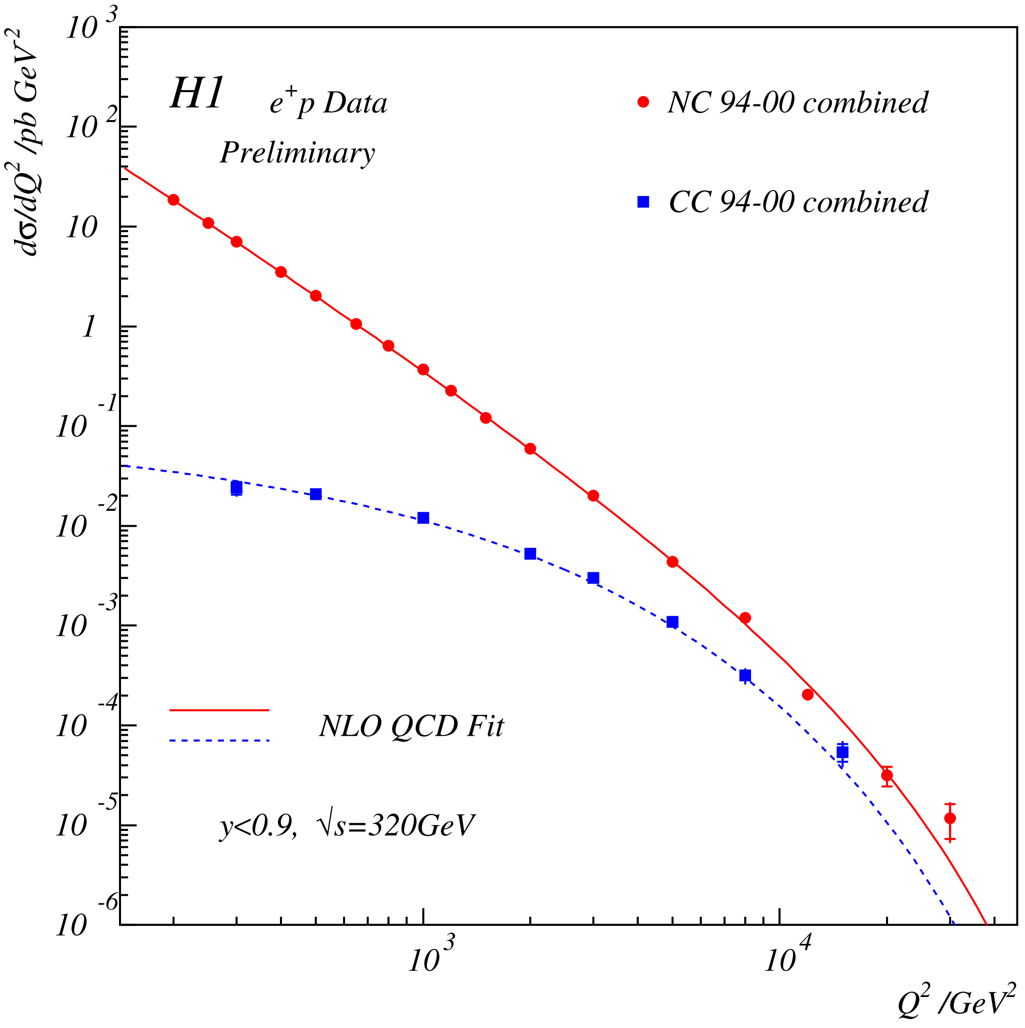

Figure 1.3: The Q^2 dependence of the CC and NC cross section measurements made using the combined 1994 - 2000 e^+p data taken by H1 [9]. The red solid circles are NC data and red solid line is the SM expectation for the NC cross section. The blue solid squares are CC data and the blue dashed line is the SM expectation for the CC cross section. Model expectations are determined from the NLO QCD fit to the 94-7 e^+p H1 data [9].

(b) Propagator terms

The propagator term relates to the exchanged boson itself and is the main factor which determines the Q^2 dependence of the cross sections. The terms in each case are:

$$\text{CC} \quad \left(\frac{1}{Q^2 + M_W^2}\right)^2 \tag{1.13}$$

$$\text{NC} \quad \left(\frac{1}{Q^4}\right), \quad \left(\frac{1}{Q^2 + M_Z^2}\right)^2, \quad \pm\left(\frac{1}{Q^2(Q^2 + M_Z^2)}\right) \tag{1.14}$$

In the CC case it is evident that the behaviour changes for $Q^2 \ll M_W^2$ and for $Q^2 \gtrsim M_W^2$:

(i) as $Q^2 \to 0$, the propagator term $\to$ a constant;

(ii) as $Q^2 \to \infty$, the propagator term $\to 1/Q^4$.

This behaviour is exhibited in fig.1.3 by the reduction in cross section size as a function of Q^2. Below $Q^2 \approx M_W^2$ the cross section is suppressed by the $1/M_W^4$ dependence and decreases slowly with respect to Q^2, influenced by other factors. Above $Q^2 \approx M_W^2$ it decreases rapidly exhibiting the $1/Q^4$ dependence.

For NC, the cross section displays a very simple $1/Q^4$ decrease until $Q^2 \approx M_Z^2$ when the contribution from the coupling and structure function terms, shown in equation 1.14, introduces a significant effect, as shown in figure 1.3.

At low Q^2, the CC cross section is suppressed with respect to the NC cross section due to the large W boson mass since, in this region, the NC cross section is dominated by photon exchange. However, at high Q^2 the cross sections are of comparable magnitude due to the similarity in mass of the W and Z bosons.

(c) Structure function term

As discussed previously, the structure function terms describe the proton substructure. Since the propagator probes the proton, the charge it carries becomes an important factor. For CC interactions the only propagator is the $W^{\pm}$ boson. The charge of the

W boson is determined by the charge of the incoming lepton. The structure functions $\tilde{W_2}$ and $x\tilde{W_3}$ are related to the charges of the quarks:

$$\tilde{W_2}^{\pm} = \frac{1}{2}W_2^{\pm}(x,Q^2) \qquad x\tilde{W_3}^{\pm} = \mp\frac{1}{2}xW_3^{\pm}(x,Q^2) \tag{1.15}$$

where

$$W_2^{+}(x,Q^2) = 2x[d(x,Q^2) + s(x,Q^2) + b(x,Q^2) + \bar{u}(x,Q^2) + \bar{c}(x,Q^2)] \tag{1.16}$$

$$xW_3^{+}(x,Q^2) = 2x[d(x,Q^2) + s(x,Q^2) + b(x,Q^2) - \bar{u}(x,Q^2) - \bar{c}(x,Q^2)] \tag{1.17}$$

$W_2^-(x,Q^2)$ and $xW_3^-(x,Q^2)$ take the same form as equations 1.16 and 1.17 respectively, but the quarks concerned are of the *up* type (u or c with charge $+\frac{2}{3}$) as opposed to the *down* type (d, s or b with charge -$\frac{1}{3}$) or vice-versa. d(x,Q^2) etc. are the PDFs of the particular quarks within the proton. The *top* quark is ignored here as its mass is too large to contribute within the kinematic range at HERA.

It follows that the structure function term ϕ_{CC} is dependent on the quark densities in the proton:

$$\phi_{CC}^{+} = x[\bar{u} + \bar{c}] + (1-y)^2 x[d + s + b] \tag{1.18}$$

$$\phi_{CC}^{-} = x[u + c] + (1-y)^2 x[\bar{d} + \bar{s} + \bar{b}] \tag{1.19}$$

In the high x domain of CC ep scattering, the $W^{\pm}$ will be sensitive to the quarks in the proton of the opposite sign. To exhibit this effect, the reduced cross section is introduced. The reduced cross section for CC (which is, in effect, the cross section with all kinematic factors removed) is given by

$$\tilde{\sigma}_{CC} = \frac{2\pi x}{G_F}\left[\frac{Q^2 + M_W^2}{M_W^2}\right]^2 \frac{\mathrm{d}^2\sigma_{CC}}{\mathrm{d}x\mathrm{d}Q^2} = \phi_{CC}^{+}(1 + \delta_{CC}^{weak}) \tag{1.20}$$

and fig. 1.4 shows this for different lepton beam types and indicates that different quarks are seen by the probe. The results with the electron beam are sensitive to the positively charged quarks in the proton, those with the positron beam to the negatively charged quarks: to first order there are 2 u valence quarks for every d in the proton which carry the largest momentum fractions, hence the cross section for e^-p scattering is larger.

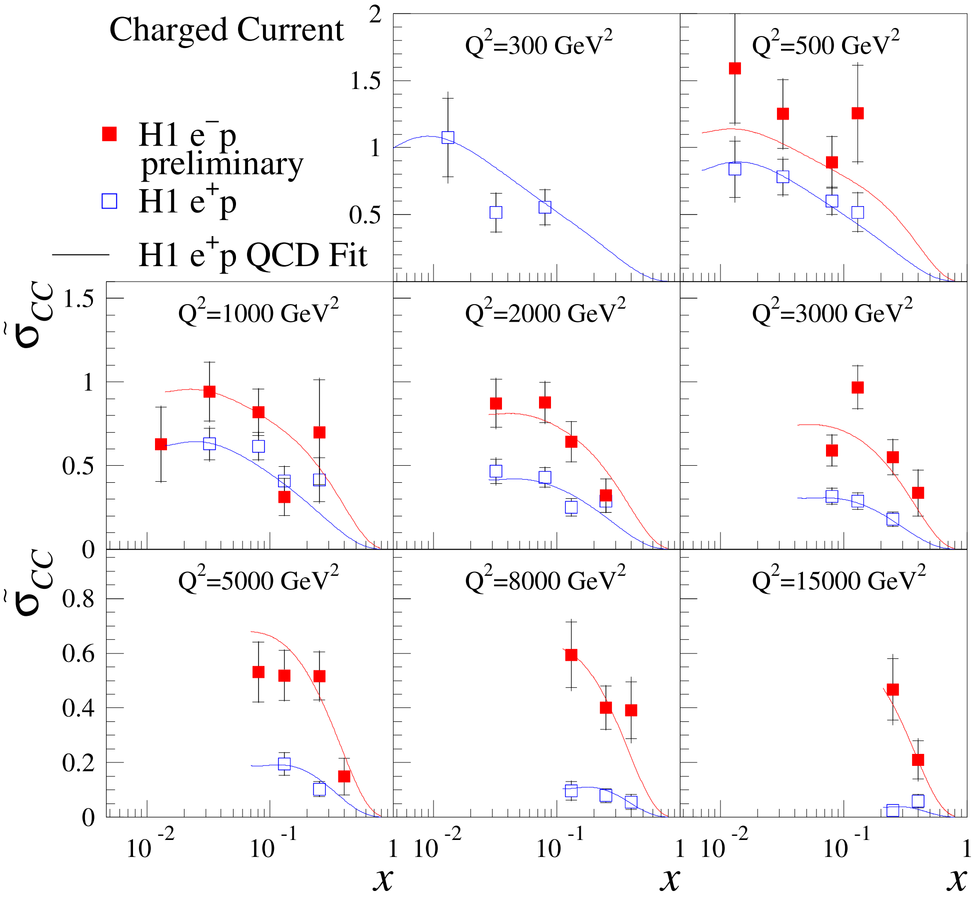

Figure 1.4: The x dependence of the reduced cross section in bins of Q^2 for both lepton beam types. Red (solid) squares are e^-p data and blue (open) squares are e^+p data. Lines are SM predictions.

In NC scattering, photons interact equally with the different quarks in the proton until, at high Q^2, the contribution of Z exchange becomes significant. The complex effects of the Z exchange and γZ interference become apparent at high Q^2, as seen in figure 1.5, where the interference is positive for e^-p scattering, and negative for e^+p scattering.

The sensitivity to the quark density within the proton for NC scattering where photon exchange dominates is given by a combination of the PDFs:

$$\phi^{\pm}_{NC} = Y_+ x \left[\frac{4}{9}(u + \bar{u} + c + \bar{c}) + \frac{1}{9}(d + \bar{d} + s + \bar{s} + b + \bar{b}) \right] \tag{1.21}$$

in which the u quark is shown to be the main contributor since at high x it is the valence quarks of the proton which are probed.

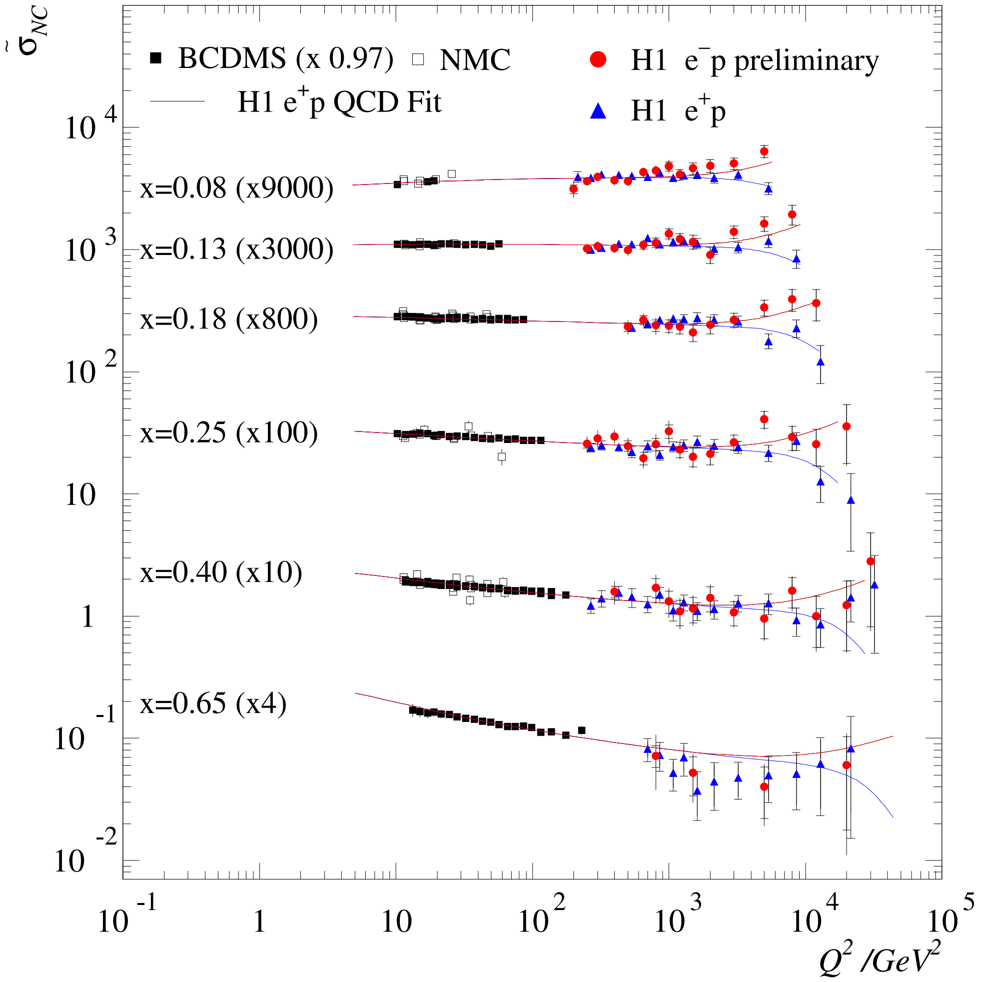

Figure 1.5: The Q^2 dependence of the reduced NC cross section. The red squares are the H1 e^-p data and the blue triangles are the H1 e^+p data taken in 1994-7. The lines are SM predictions.

1.2 Radiative Charged Current

In the Standard Model of Electroweak interactions, the couplings of the charged W boson to its neutral counterparts, the photon (γ) and the Z^0 boson, are fixed by the the non-abelian nature of the SU(2)xU(1) gauge symmetry. This thesis examines the WWγ triple boson vertex, which becomes accessible when the W boson exchanged during a CC event radiates a photon, shown in fig. 1.6: so-called 'radiative CC' events. The diagrams shown in fig. 1.7 illustrate that the photon can also be emitted from the lepton or quark lines, but these do not contribute to the understanding of the triple boson vertex.

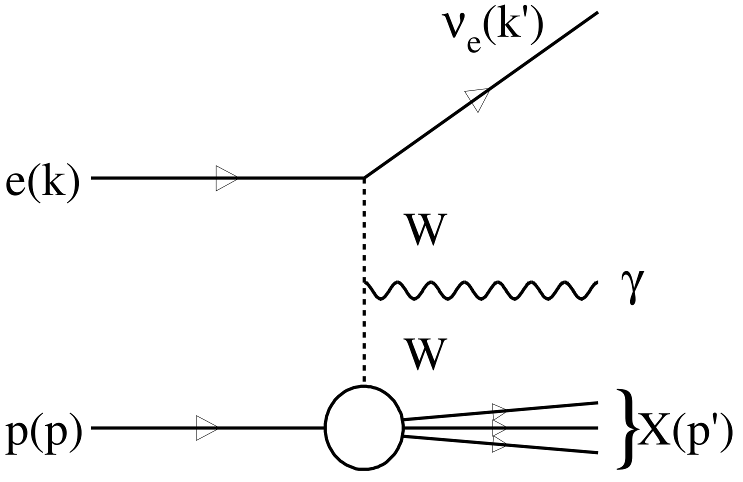

Figure 1.6: Feynman diagram for radiative CC scattering.

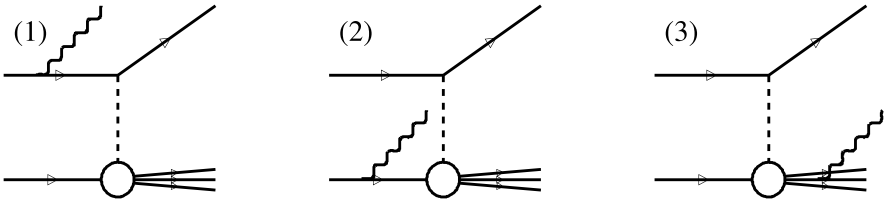

Figure 1.7: Feynman diagrams for scattering with radiation.

It is interesting to look for events with the topologies predicted for radiative CC within the phase space available at HERA for two reasons:

(i) to examine the *anomalous* couplings of the WWγ vertex, $\Delta\kappa$ and λ, which arise if the restrictions of the SU(2) gauge symmetry are released

(ii) to compare the cross sections calculated from the data for this process to Standard Model and Beyond the Standard Model (BSM) predictions.

The measurement of the tri-linear couplings of the electroweak gauge bosons is a stringent test of the SM. As such, it is also a useful probe for new physics. The most general Lorentz invariant parameterisation of the WWγ vertex can be defined in terms of 7 independent couplings. Assuming electromagnetic gauge invariance, C - and P- conservation, the 7 couplings can be reduced to 2 parameters: $\Delta\kappa$ and λ. Non-zero values of these anomalous couplings would be contrary to the expectation from the SM [17] [18]. The anomalous couplings themselves are terms which govern the behaviour of the magnetic dipole moment and electric quadrupole moment of the bosons, and hence their coupling to other bosons.

Radiative CC events are very rare at HERA so the anomalous coupling measurements are not expected to be competitive with those achieved by the LEP experiments due to the very limited statistical accuracy available [19]. However, the examination of the cross sections for events selected with the required topology for the different beam types and COM energies used at HERA will allow comparisons with SM expectation within the available phase space. The region of phase space probed differs considerably from that probed by the LEP experiments due to the different beam types and COM energies.

In addition, it is also currently of particular importance as the H1 experiment has observed an excess of 'single W production' events [21] which arise from the NC scattering interaction $ep \rightarrow eWX$ (see fig. 6.5 in section 6.5 for a Feynman diagram of this type of event). Analysis of radiative CC type interactions can be, with this in mind, a valuable consistency check with the NC single W production cross section [20] and a useful verification of the contribution to the event sample from radiative CC events.

1.2.1 The Radiative CC Cross Section

An intuitive idea of the expectations for the cross section for radiative CC may be constructed if the likely sources of radiation in CC events are separated out. Each contribution is shown in figs. 1.6 and 1.7. The likelihood of the incoming lepton or $W^{\pm}$ boson radiating a photon is the same whether the lepton is an electron or positron. Radiation from the incoming quark may be neglected as it will probably be emitted co-linear to the beam and, hence, follow the proton remnant down the beam-pipe.

The significant radiation, in addition to that from the incoming lepton and the W boson, is therefore expected to be that from the outgoing quark. Since the radiation term from $e^{+}p$ scattering is likely to have an outgoing u quark, the radiation contribution ($\propto$ charge^2) is naively expected to be slightly larger than that from $e^{-}p$ scattering, despite the cross section for CC scattering being shown to be contrary to this. However, this naive prediction will be discussed later in this section and compared to the measurements.

A more formal definition of the differential cross section for the $ep \rightarrow \nu\gamma X$ process is given by the following [16]:

- for e^+p

$$\frac{\mathrm{d}\sigma_{CC\gamma}^{e^+p}}{\mathrm{d}x} = \frac{\alpha^3}{4\pi^2 s}\frac{1}{\sin^4\theta_W x}\mathrm{d}^3PS\Big(\sum_{f=d,s,b} q_f|\mathcal{M}|^2 + \sum_{\bar{f}=\bar{u},\bar{c}} q_{\bar{f}}|\bar{\mathcal{M}}|^2\Big) \tag{1.22}$$

- for e^-p

$$\frac{\mathrm{d}\sigma_{CC\gamma}^{e^-p}}{\mathrm{d}x} = \frac{\alpha^3}{4\pi^2 s}\frac{1}{\sin^4\theta_W x}\mathrm{d}^3PS\Big(\sum_{f=u,c} q_f|\mathcal{M}|^2 + \sum_{\bar{f}=\bar{d},\bar{s},\bar{b}} q_{\bar{f}}|\bar{\mathcal{M}}|^2\Big) \tag{1.23}$$

where s is the COM energy and q_f are the parton distribution functions. The 3 - particle phase space is parameterised as follows:

$$\mathrm{d}^3PS = \frac{\pi E_{q'}E_\gamma}{4S_4}\mathrm{d}E_\gamma \mathrm{d}(\cos\theta_\gamma)\mathrm{d}(\cos\theta_{q'})\mathrm{d}\phi \tag{1.24}$$

where

$$S_4 = E_e + xE_p - E_\gamma - (E_e - xE_e - E_\gamma\cos\theta_\gamma)\cos\theta_{q'} + E_\gamma\cos\phi\sin\theta_{q'}\sin\theta_\gamma \tag{1.25}$$

and E_e and E_p are the energies of the lepton and proton beam respectively[2]. The neutrino momentum and overall azimuthal orientation have been integrated out. The $\mathcal{M}$ terms are the sum of the matrix elements of the Feynman diagrams for radiation from the initial lepton, initial quark and scattered quark - parts 1, 2 and 3 in fig. 1.7 respectively - and intermediate charged W boson, shown in fig. 1.6. These terms depend on the products of the particles 4-momenta. The anomalous couplings, $\Delta\kappa$ and λ, only contribute in terms involving radiation from the W boson.

Predictions using this formal cross section calculation, given in chapter 9, give results which are contrary to those discussed as a intuitive prediction. However, the data results are more closely in agreement with this idea, although they are inconclusive since the statistical sample of events is so limited.

1.3 Beyond the Standard Model

There are many different theories which propose physics beyond the Standard Model. These theories frequently predict the occurence of events which have a characteristic imbalance of transverse momentum, with or without the additional requirement of an isolated photon.

---

[2] These equations are valid for unpolarized electrons.

One such theory - that of the 'composite' model [22] - predicts 'excited neutrinos' which would give a signature of missing momentum and an isolated photon. Excited neutrinos would be observable if the neutrino in a CC event were to decay:

$$ep \rightarrow \nu^* X \rightarrow \nu\gamma X \tag{1.26}$$

If excited neutrinos were found, this would be convincing evidence for the substructure of fermions, which are currently believed to be point-like particles. ep collisions at HERA energies provide an excellent hunting ground for the observation of such states and an analysis is currently underway [23] to examine the possibility of the existence of such decays. Although no such evidence has yet been found, if the radiative CC analysis were to reveal an excess of events, excited neutrinos would be one possible explanation.

Another model which could produce possible candidates with the appropriate topology is *supersymmetry* (SUSY) with gauge mediated breaking [24]. This produces final states with high momentum, isolated photons but these models predict very large squark masses and have, to date, not been explored at HERA due to the extremely high COM collisions required.

Chapter 2

The H1 Detector at HERA

2.1 The HERA collider

The Hadron Electron Ring Anlage (HERA) is situated to the west of the city of Hamburg. It was built between 1984 and 1990 and is composed of two circular storage rings inside a tunnel approximately 30m below ground level. The tunnel has a circumference of 6.3km. Electrons or positrons are accelerated clockwise (if viewed from above) around one storage ring to 27.5 GeV, and in the other storage ring protons are accelerated to 920 GeV anti-clockwise. Collisions occur at two predetermined points on the ring and detectors are built around these points: H1 is at the northern interaction point and ZEUS is at the southern. The resulting COM energy $\sqrt{s}$ at these interaction points is approximately 320 GeV. Until 1998 the COM energy was 300 GeV due to a lower proton beam energy of 820 GeV.

The electrons and protons circle around the storage rings with currents of about 30 mA and 100 mA respectively, in a maximum of 220 bunches each separated by 96 ns. The storage rings intersect at the two interaction points. The typical number of colliding bunches which meet at the interaction points is 175. The non-colliding bunches are referred to as 'pilot bunches' and are used to determine certain background levels. These backgrounds are due to 'beam gas' and 'beam wall' interactions where a proton or electron from the beam interacts with residual gas in the beam pipe or with the beam pipe itself. The proton bunch has a complex structure: it has a longitudinal structure with a gaussian distribution of length $\sim$ 11cm. The beam undergoes compression to achieve this 11cm length but during this process some of the current becomes separated to form 'satellite' bunches, removed from the main bunches by 72cm. The maximum design luminosity of the system is at present 1.4×10^{30} $\mathrm{cm}^{-2}\mathrm{s}^{-1}$ but during the year to come (2001) this will undergo a significant upgrade.

2.2 The H1 Detector

The H1 detector, shown in figure 2.1, was designed to study a wide range of *ep* physics processes. Due to the variety of processes which occur in high energy electron - proton collisions, it was necessary for the design of H1 to satisfy the following criteria:

- hermetic coverage
- asymmetric detector design to compensate for different beam energies
- accurate tracking and calorimetry for momentum and energy measurement
- fast triggering
- luminosity measurement.

Descriptions in this section will be almost entirely restricted to the detector systems which are essential to the measurements presented in this thesis.

2.2.1 The Coordinate System

The H1 detector provides almost hermetic coverage of the space accessible to particles emanating from the electron - proton interactions. Points within the detector are defined using Cartesian coordinates (x, y, z) with respect to the origin, taken to be the nominal interaction point. The positive z direction follows the proton beam direction (right to left in fig. 2.1) through the detector. The y direction is vertically upwards, and x points horizontally towards the centre of the HERA ring. A spherical polar coordinate system (r, θ, ϕ) is used to describe angles in the detector, such that the polar angle $\theta = 0°$ is along the $+z$ axis and the azimuthal angle ϕ is an angle in the x-y plane. In accordance with H1 accepted convention, the 'forward' region refers to the region of low θ.

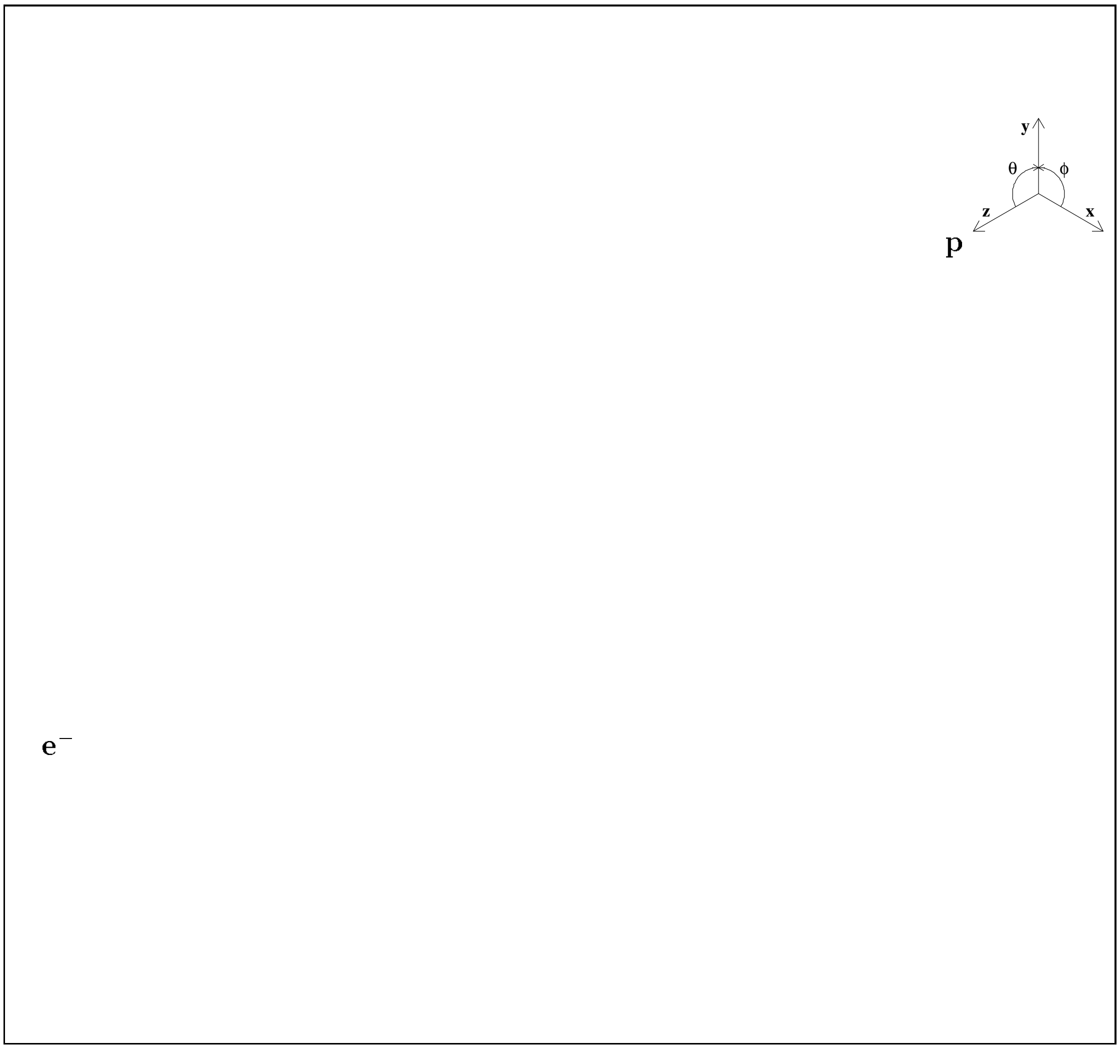

1	Beam pipe and beam magnets	9	Muon chambers
2	Central tracking device	10	Instrumented iron yoke
3	Forward tracking device	11	Forward muon toroid
4	Electromagnetic LAr calorimeter	12	Back. electromag. calorimeter (SPACAL)
5	Hadronic LAr calorimeter	13	PLUG calorimeter
6	Superconducting coil (1.15 T)	14	Concrete shielding
7	Compensating magnet	15	Liquid argon cryostat
8	Helium supply for 7		

Figure 2.1: 3D view of the H1 detector.

2.2.2 Luminosity

The luminosity system is essential for accurate cross section measurements. It is situated in the backwards direction in the accelerator tunnel and is composed of two crystal calorimeters [25]: the Electron Tagger (ET) at $z = -33.4$m adjacent to the electron beam pipe, and the Photon Detector (PD) at $z = -102.9$m adjacent to the proton beam pipe. The luminosity is calculated using the Bethe-Heitler process ($ep \rightarrow ep\gamma$) for which the cross section is known precisely from QED. Initially (online), only a measurement in the PD is taken, but H1 is fortunate in that the two independent detectors, the PD and ET, enable the initial value to be cross checked. The luminosity is corrected to give an accurate measurement by accounting for any additional background processes, detector acceptance and the proportion of luminosity contained in the satellite bunches.

2.2.3 Calorimetry

The H1 detector contains four separate calorimetric units with different angular acceptances. They are the Liquid Argon Calorimeter (LAr), the Spaghetti Calorimeter (SPACAL), the Plug Calorimeter (PLUG) and the Tail Catcher (TC). These are shown in fig.2.1, labelled 4 and 5, 12, 13 and 10 respectively. The most important of these for the following analyses is the LAr which is the primary source of both energy measurement and event triggering. The SPACAL has also been useful for related studies. All calorimeters at H1 work on the same principle: they consist of layers of passive material which induce the particles moving through them to lose energy by showering. These layers are inter-spaced with sensitive, or active, regions which measure the development of the shower by sampling the energy loss. The materials used differ depending on the type of particle that the calorimeter is designed to detect: hadronic particles are known to penetrate further into material than electromagnetic particles, and hence, the detector is designed accordingly with the hadronic part of a calorimeter further from the interaction point than the electromagnetic part to account for the longer hadronic shower profile. The resolution of each calorimeter is also of importance and will be described in the following.

The Liquid Argon Calorimeter

The LAr has a particle detection acceptance over the range $4° < \theta < 154°$ and consists of two sections, both contained in a single liquid argon cryostat: the inner layer which detects electromagnetic (EM) showering and the outer which detects hadronic (HAD) showering. The materials which induce showering are lead plates of 2.4 mm thickness in the EM case, and stainless steel of 19mm thickness in the HAD case. The depth of the EM calorimeter is equivalent to 20 to 30 radiation lengths, X_0. The HAD calorimeter depth is 5 to 7 interaction lengths, λ_I. The liquid argon acts as the sensitive region between each of the metal plates to sample the number of electrons produced in the shower as the traversing particle induces ionisation. The liquid argon 'cells', of which there are 44,000 of varying sizes, have a high voltage applied across them. The induced signal is read-out and known to be proportional to the energy of the particle incident on the cell. The signals from a group of cells (called a 'Big Tower') are combined to give more comprehensive information about the energy deposits throughout the detector, which can then be used for fast decisions on whether to accept or reject events (see section 4.1).

For convenience, the LAr calorimeter is split into 8 different 'wheels': (from front to back) the Inner and Outer Forward (IF, OF) of which the OF has only a hadronic part, the Forward Barrel (FB2, FB1), the Central Barrel (CB3, CB2, CB1) and the Backward Barrel Electromagnetic (BBE) which has only an electromagnetic component (see fig. 2.2). The shape, number and orientation of liquid argon cells varies from wheel to wheel, but each wheel is optimised to allow the best possible measurement of the particle shower assuming a certain shower shape with respect to the interaction point. There are, however, regions between the wheels (z-cracks), and between the 8 'phi octants' (ϕ-cracks) into which the wheels themselves are split, that are insensitive (see fig. 2.3).

The LAr calorimeter is an example of a non-compensating calorimeter. Non-compensating means that the response for electrons and hadrons is not equal: hadrons on average deposit $\sim 30\%$ less energy than electromagnetic particles of the same original energy. This reflects the energy lost by hadrons to nuclear excitations or breakup in the absorber material. Compensation in the LAr calorimeter is achieved through software weighting techniques.

After calibration, carried out using a test beam and cross checked *in-situ*, the calorimeter has been found to have an energy resolution of $\frac{\sigma_{EM}(E)}{E} \approx \frac{0.15}{\sqrt{E}} \oplus 0.01$ for electrons, and $\frac{\sigma_{HAD}(E)}{E} \approx \frac{0.5}{\sqrt{E}} \oplus 0.02$ for charged pions. The absolute energy scale is known to between 0.7% and 3% (depending on the wheel) for the EM and 2% for the HAD.

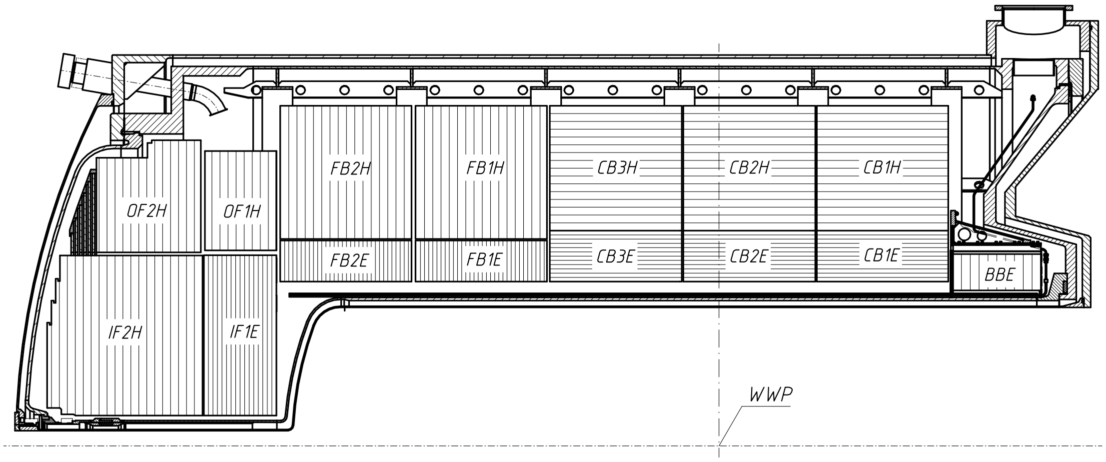

Figure 2.2: The layout of the 8 wheels of the LAr calorimeter.

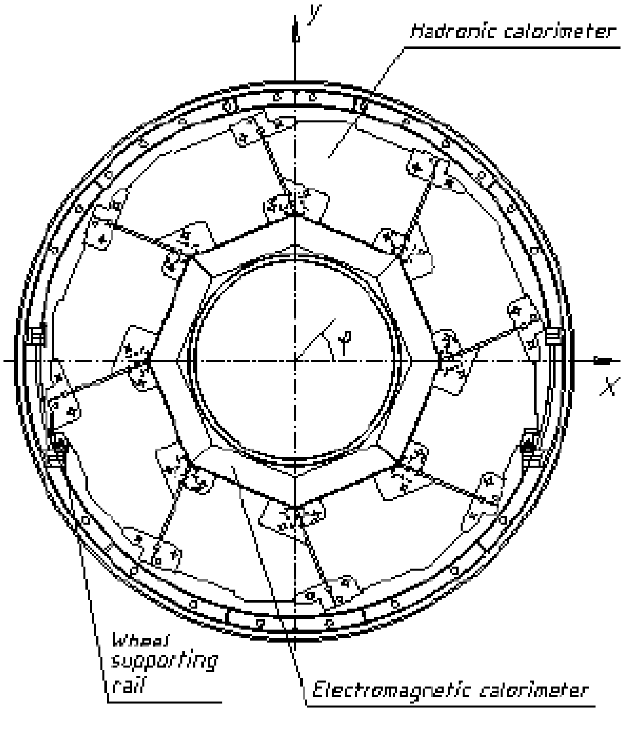

Figure 2.3: The layout of the 8 ϕ octants of the LAr calorimeter.

The SPACAL

The SPACAL is a cylindrical detector which sits in the x - y plane in the backward region of the detector, approximately 1.5 m behind the interaction point. It has both EM and HAD components and covers the range $153^\circ < \theta < 178^\circ$. It consists of 0.5mm diameter scintillating fibres embedded in lead plates. Showering particles induce a signal in the fibres which is collected in photomultiplier tubes behind the detector. The energy resolution of the detector is $\frac{\sigma(E)}{E} \approx \frac{0.07}{\sqrt{E}} \oplus 0.01$ for electromagnetic interactions and it has a depth of approximately 2 interaction lengths. The overall resolution is known to within 7%. The SPACAL is essential for the measurement of electrons in the backward region, which corresponds to low Q^2 DIS NC events. This feature proves useful to this thesis in the low p_t CC triggering study of section 4.4. It addition, it provides a measurement of hadronic energy and time-of-flight information, useful for the rejection of background such as beam-gas and beam-wall, and is also useful for the rejection of non-CC ep interactions.

The Tail Catcher

The TC is the iron return yoke of the magnet, instrumented with limited streamer tubes. It surrounds the outside of the LAr calorimeter and has two main functions: muon detection and measurement of hadronic energy not contained in the LAr. The energy resolution is $\frac{\sigma(E)}{E} \approx \frac{1}{\sqrt{E}}$. It plays an important part in identifying background events in a CC analysis.

The PLUG

The PLUG Calorimeter closes the gap in particle acceptance between the LAr and the beam pipe, from 0.5° to 3.5°. It consists of silicon wafers interspersed with copper absorbers. In the analyses presented here, it is useful for differentiation between genuine DIS events and photoproduction background at low transverse momenta.

2.2.4 Tracking

The tracking detectors in H1 are a combination of drift chambers and multi-wire proportional chambers (MWPCs). These are embedded in a 1.15T magnetic field, provided by a superconducting solenoid which encases the calorimeters. There are two major parts to the tracking system which are themselves made up of smaller detectors: the Central Track Detector (CTD) (no. 2 in fig. 2.1) which has an angular acceptance of $25° < \theta < 155°$, and the Forward Track Detector (FTD) (no. 3 in fig. 2.1), which increases the acceptance in the forward region down to 5° (see fig. 2.4). In all cases the chambers work on the principle of using a charged particle to induce ionisation in a volume of gas. The electrons from the ionisation provide an electrical signal which can be used to reconstruct particle tracks and hence determine the charge and momentum of the particle.

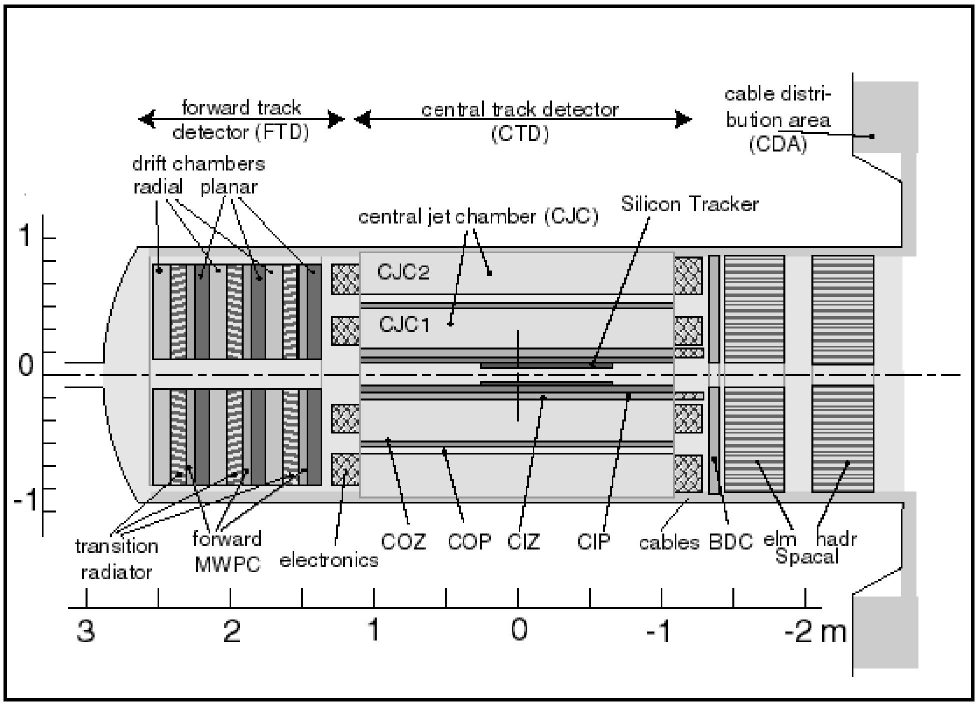

Figure 2.4: Cross section through the H1 tracking detectors.

The Central Track Detector

The CTD consists of 4 drift chambers (the central jet chambers CJC1 and CJC2, and the inner and outer z chambers CIZ and COZ) and 2 MWPCs (the inner and outer central proportional chambers CIP and COP). By building up layers of drift chambers it is possible to reconstruct the trajectory of a charged particle. This is the primary purpose of CJC1 and CJC2. The sense wires of the CJCs run parallel to the z axis and are inclined 30° with respect to the radial direction to provide good resolution in the $r-\phi$ plane. The CIZ and COZ have wires which are strung azimuthally which compensates for the bad z resolution of the CJCs. The CIP and COP chambers have a good response time and are used for triggering purposes: they provide a fast timing signal with a resolution of 21ns which is good enough to determine in which bunch crossing an interaction occured. The information from the CIP and COP is also combined with information from MWPCs in the FTD to determine the z-vertex position of the interaction, hence giving a useful handle for fast background rejection.

The Forward Tracker

The FTD is made up of three 'super-modules', each containing a planar wire drift chamber (PWDC), a forward MWPC (FMWPC), a transition radiator and a radial wire drift chamber (RWDC). The super-modules are positioned around the z axis with the wires strung perpendicular (radially) to the z axis in the PWDC (RWDC). The PWDCs are rotated by 60° with respect to each other to enable resolution of hodoscope ambiguities. The FMWPCs are used with the CIP and COP, as described above.

2.2.5 Time of Flight Counters

The Time of Flight (ToF) systems are a simple but very effective means of rejecting events which arrive 'out-of-time', generally from beam induced processes. The ToF systems are plastic scintillators which are located within the detector near the beam pipe in three places. There is also a double layer of scintillators, called the 'Veto Wall', positioned in the backwards direction behind the Iron return yoke, which rejects events caused by the proton beam-halo. Their timing measurement is accurate to 1 ns.

2.2.6 Triggering

It is essential to H1 that as much useful physics data from ep interactions as possible is recorded. This is a non-trivial problem since bunch crossings at HERA occur once every 96 ns. To record an event in full, with all sub-detector information included, requires $\sim$100 ms. In order to tackle this problem, H1 employs filters to limit, as far as possible, the non-physics events which are recorded. These filters are the 'triggers' and most sub-detectors produce a signal which can be used for this purpose. A decision to keep or reject an event is made on the basis of the trigger element response from each sub-detector. The levels at which an event may be rejected are as follows [26]:

- **Level 1** (up to 2 μs). When activity occurs in the detector, each sub-detector returns information, in the form of a trigger element, to the central trigger logic (CTL). The CTL stores these responses in a 'pipe-line'; some trigger elements take longer to arrive at the pipe-line than others and typically the last arrives 2μs after the bunch crossing occured. The CTL then logically combines the information to search for events which satisfy certain combinatorial requirements. These combinations are called 'sub-triggers'. If any one of the 128 sub-triggers are satisfied, the full event information is passed to the next level. Typically one event in ~10,000 satisfies L1.

- **Level 2** (up to 20 μs). When an event reaches L2 there are further requirements made. These include the use of neural networks (L2NN) and topological configurations (L2TT) to reject another fraction of events. (Level 3 has yet to be implemented.)

- **Level 4** (up to 100 ms). At L4 the events are fed through to 'the farm' - a bank of PCs capable of processing many events simultaneously. Some on-line reconstruction is done at this stage, and some software cuts may be applied. L4 rejects the majority of the remaining beam-gas interactions, and those events originating from trigger noise. After passing L4, data is written out to tape at a rate of 10-20 Hz. For very commonly occuring events the trigger may be 'pre-scaled', so that only every 1 in 10 events, for example, is written to the data storage tapes (DSTs)[1]. Once all the event information is stored on DSTs it can then be handled off-line (called Level 5) and it will undergo a full reconstruction and classification. The data are then ready to be analysed.

The trigger elements used in this work are a combination of LAr signals, track based triggers and vetos to reject background interactions. They are described in more detail in section 4.1.

---

[1] None of the triggers used in this work are subjected to a pre-scale.

Chapter 3

Kinematic Reconstruction and Data Modelling

The accurate reconstruction of kinematic variables and the ability to correctly model the data are two essential aspects of physics analysis. This chapter discusses both of these points with respect to the analyses presented in this thesis.

The methods used to reconstruct the kinematic variables of the observed processes are described and compared. The limitations on the reconstruction methods available are discussed.

The programs used to model the data, Monte Carlos (MCs), are also described. These programs are used to simulate genuine DIS processes and 'background' processes - unwanted events produced by other processes which may form a significant contribution to a data sample. MCs are essential for the correct determination of the resolution, acceptance and efficiency effects which may occur due to the limitations of the detector. Corrections to the data can be made on the basis of understanding the detector response proven by MC studies. The application of these corrections will be discussed in later chapters.

3.1 Reconstruction of Kinematic Variables

To reconstruct the kinematic variables of a CC event there is only one possible method of combining the available information. This is due to the impossibility of detecting the scattered neutrino. For the reconstruction of NC events, which are used for cross checks and calibration studies for example, there are several methods available as there is redundant information from the hadronic final state and the scattered electron.

The Hadron Method

The hadron method (also called the Jaquet-Blondel [35] method) uses the summation over all particles in the hadronic final state i. The variables y, Q^2 and Bjorkën-x are determined using:

$$y_h = \frac{\Sigma}{2E_e} \qquad Q_h^2 = \frac{p_{t,h}^2}{1-y_h} \qquad x_h = \frac{Q_h^2}{sy_h}. \tag{3.1}$$

The quantities Σ, transverse momentum $p_{t,h}$ and the inclusive hadronic angle γ_h are defined as follows:

$$\Sigma = \sum_i (E_i - p_{z,i}) \qquad p_{t,h} = \sqrt{(\sum_i p_{x,i})^2 + (\sum_i p_{y,i})^2} \qquad \tan\frac{\gamma_h}{2} = \frac{\Sigma}{p_{t,h}}. \tag{3.2}$$

The variables E_i and $p_{z,i}$ are the energy and longitudinal momentum of particle i, respectively; $p_{x,i}$ and $p_{y,i}$ are the momentum components of the particle in the x and y directions. The effect on y due to losses in the forward direction are minimal but $p_{t,h}^2$ may suffer a slight degradation of resolution, as will Q^2 due to it's dependence on $p_{t,h}^2$. Losses due to particles escaping down the backwards beam pipe also cause a degradation of y resolution.

The Electron Method

The e method uses the information available from the energy E_e' and polar angle θ_e of the scattered electron in NC events:

$$Q_e^2 = 4E_eE_e'\cos^2\frac{\theta_e}{2} \qquad y_e = 1 - \frac{E_e'}{E_e}(1-\cos\theta_e) \qquad x_e = \frac{Q_e^2}{sy_e}. \tag{3.3}$$

The Sigma Method

The Σ method uses information from both the electron and hadronic final states:

$$y_\Sigma = \frac{\Sigma}{E-p_z} \qquad Q_\Sigma^2 = \frac{(E_e'\sin\theta_e)^2}{1-y_\Sigma} \qquad x_\Sigma = \frac{Q_\Sigma^2}{sy_\Sigma} \tag{3.4}$$

where $E - p_z = \Sigma + E_e'(1-\cos\theta_e)$.

The $e\Sigma$ Method

The relative merits of using the e and Σ reconstruction methods are again dependent on the region of phase space under examination. In the analysis of NC events, best results are obtained by using a combination of the e and Σ methods [27]:

$$Q^2_{e\Sigma} = Q^2_e \qquad x_{e\Sigma} = x_\Sigma \qquad y_{e\Sigma} = \frac{Q^2_e}{x_{e\Sigma}s}. \tag{3.5}$$

3.2 Data Modelling

In order to extract physical quantities from measurements made at HERA, or any particle collider, it is essential to understand and be able to model the processes which it is believed under-lie the observed events. It is also essential to understand the behaviour of the detector in order to correct for any inefficiencies due to acceptance, for example, which may distort the measurements. It is for these reasons that MC simulations are employed. MCs are written for different physics processes. The parton level 'generated' events are passed through a simulation of the hadronisation process and then a reconstruction of the detector and, to a very high degree, mimic the data. This section details the Standard Model MCs used in the presented analyses.

DJANGO

`DJANGOH 1.2` [36] is a DIS MC. It is based on the `HERACLES` [37] event generator and is extended to include QCD effects. `HERACLES` simulates NC and CC ep interactions at the parton level and calculates, within certain kinematic regions, differential cross sections for the aforementioned processes. `DJANGO` also incorporates elements of the `LEPTO` [38] and `JETSET` [39] programs which deal with the hadronisation of the scattered quark and proton remnant. QED radiation effects are also incorporated; electroweak radiative corrections are made to the $O(\alpha)$ cross sections.

PYTHIA

`PYTHIA 5.7` [40] is a photoproduction MC. Photoproduction is the most significant background contribution to the DIS sample. These events can arise from almost real ($Q^2 \sim 0$ GeV^2) ep interactions. The electron is scattered through a very small angle and may be undetected, the final state faking a CC event. `PYTHIA` incorporates direct, resolved and prompt photon processes.

WWGAMMA

`WWGAMMA` [41] is written as an addition to the standard `DJANGO`. `DJANGO` does not treat all possible elements of radiation from DIS processes fully, so `WWGAMMA` fills the gap left with respect to the $WW\gamma$ vertex. It also treats QED radiation from CC events more thoroughly. `WWGAMMA` is purely a generator level MC, so detector acceptance corrections to the calculated cross sections must be done by hand.

Chapter 4

Systematic Studies

This chapter contains the descriptions and studies of some essential components of the presented measurements. Firstly the method of triggering, or initially identifying, Charged Current or radiative CC events is described, followed by a discussion of energy measurement in the H1 detector. The application of the results of these studies will be discussed in later chapters.

4.1 Triggering

The accurate determination of the CC cross section and other related measurements is entirely dependent on the assumption that it is possible to select and identify the events correctly at H1. In order to verify this assumption it is essential to calculate the efficiency with which events are found. In this section, the triggers are described in full, methods of efficiency calculation are shown, and studies of possible means of enhancing the triggers are discussed.

The triggers used to identify events are composed of 'trigger elements' which are combined into 'subtriggers'. Those triggers specific to the CC analysis are now described.

4.1.1 The Trigger Elements

The trigger elements (TE) use individual aspects of calorimetry, tracking and veto conditions [26]. The TEs used are the following:

LAr elements

LAr_Etmiss	Missing transverse energy indicated by an imbalance of the distribution of energy in the LAr 'Big Towers' (BTs) - see fig. 4.1. The trigger thresholds vary according to detector region.
LAr_T0	A timing signal from the LAr BTs.
LAr_BR	A 'Big Ray' is a combination of a measured energy exceeding a threshold set in a LAr BT and a spacially associated a track in an MWPC (see *zVtx_T0* and *FwdRay_T0* below).
LAr_IF	A threshold is set for the summation over all the energy deposited in the Inner Forward region BTs.
LAr_BigT_miss	A topological TE. It identifies an imbalance in ϕ of the energy in all the BTs.
LAr_electron	An electron in the LAr, identified by the energy in one EM trigger tower exceeding one threshold and the energy in the HAD tower not reaching a second threshold. The thresholds are set with respect to polar regions of the detector.

Tracking elements

zVtx_T0 / sig1	This is an indication of the event vertex position along the z axis. Track information from the CIP, COP and FMWPC is combined to form lines, or particle 'rays'. *T0* is a minimum ray signal and *sig1* is a ray signal of a higher significance.
FwdRay_T0	A forward region ray finder, using the FPC and CIP to detect rays which are compatible with the interaction region.
DCrϕ_T0 / Tc	This trigger looks for tracks in the CTD by overlaying masks in the shape of possible track trajectories and checking for hits within the masks. *T0* is the detection of a track with a minimum transverse momentum, *Tc* is a high momentum track.

Veto conditions

ToFs, Veto Wall	These TEs use a 'timing window' to determine if incident hits originate from an interaction or from proton beam background. The hit timing depends on the path length of the particle: background signals will arrive earlier than those from interactions as the path length is shorter.
RZ_veto	A veto of tracks in the z chambers with polar angle in the range $20^o < \theta < 90^o$ which have a vertex outside the interaction region.
CIPB_noSPCL	This veto is set if a large number of tracks are found in the rear section of the CIP but no energy is found in the SPACAL.

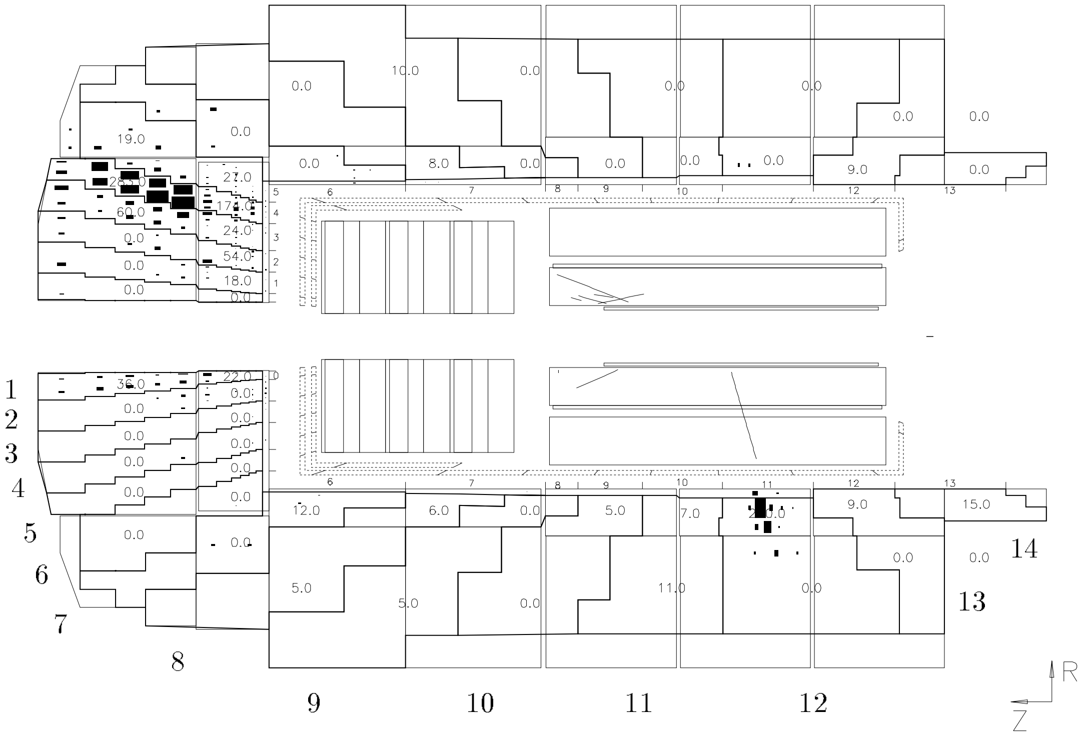

Figure 4.1: An NC event display picture showing the layout of the LAr BTs with respect to the polar cross section of the detector. They are numbered 1 to 14. BTs are groups of cells pointing towards the interaction point.

4.1.2 The Sub-Triggers

The TEs are combined to form sub-triggers (ST) which capitalise on certain characteristics of the CC events:

- **ST66**: *LAr_Etmiss* & *LAr_IF* & *(Ray_T0 or LAr_T0)*
- **ST71**: *zVtx_sig1* & *DCRΦ_T0* & *DCRΦ_Tc* & *LAr_BR* & *LAr_BigT_miss*
- **ST77**: *LAr_Etmiss* & *Ray_T0*

All these sub-triggers are essentially a requirement of imbalanced energy in the LAr with a good timing signal. In addition, they all have the requirement that one or more of the vetos are *not* set. The use of some STs originally designed to trigger NC events is proven to enhance the CC trigger efficiency without introducing significant background [27], hence the following STs are also included:

- **ST67**: *LAr_electron* & *Ray_T0*
- **ST75**: *LAr_electron* & *DCRϕ_THig*

In this case, the use of the 'electron' triggers is useful purely as an indication of an energy cluster in the LAr, regardless of its source.

The STs are used within the following analyses to select the initial event sample. Further selection criteria are then specified.

4.2 Trigger Efficiency Determination

The efficiency of the CC triggers is difficult to determine using only the information provided by the CC sample itself due to the very limited statistical sample. Another method has been developed to overcome this difficulty, called the 'pseudo CC' method [28]. A pseudo CC event is a NC event from which all the electron information has been removed. With all electron information discarded, a NC event has identical characteristics to that of a CC event. The number of events in the high Q^2 NC sample is a factor of 100 larger than the CC sample, so the statistics available are much more suitable for an accurate efficiency determination.

The efficiency ε is calculated using the following formula:

$$\varepsilon = \frac{\text{No. events triggered by ST}(66||67||71||75||77)}{\text{No. of events in whole pseudo CC sample}} \tag{4.1}$$

where || is a logical *or* of the STs.

4.3 Trigger Efficiency Results

Plots of global efficiencies with respect to certain kinematic variables are shown in fig. 4.2. As a function of p_t^{miss} (where $p_t^{miss} \equiv p_{t,h}$ in eqn. 3.2), the global efficiency shown in fig. 4.2(a) rises from approximately 50% at a $p_t^{miss} \sim 12$ GeV, to 100% at $p_t^{miss} \sim 70$ GeV. The inefficiency at lower values of p_t^{miss} becomes more obvious in fig. 4.3 where it is shown in terms of p_t^{miss} for different ranges of hadronic angles in the detector. In the lowest range of inclusive hadronic angle where $\gamma_{had} \sim 5^\circ$ (see eqn.3.2), i.e. in the very forward region, the efficiency is below 50% until the highest values of p_t^{miss}. This is due to two factors: losses down the beam pipe since the LAr calorimeter only starts at 4°, and the setting of the trigger thresholds in the forward region (see section 4.4.2).

The low efficiency behaviour is also shown in fig. 4.2(b), the global efficiency in terms of γ_{had}, and fig. 4.4, plots of efficiency as a function of γ_{had} in bins of p_t^{miss}. At the lowest γ_{had} values in every plot the efficiency is always lower than in any other region. These plots also indicate that the most efficient region of the detector is the forward barrel region where, for all values of p_t^{miss}, the efficiency never falls below 50%.

The global efficiency as a function of the azimuthal angle, ϕ, fig. 4.2(c), shows a reasonably uniform behaviour: the values fluctuate between 70% and 90%. As a function of Q^2, fig 4.2(d), the efficiency is similar to that shown as a function of p_t^{miss}: this is expected as the two quantities are related by the equation

$$Q^2 = \frac{p_t^{miss}}{1-y} \tag{4.2}$$

so, for events at low y which go in the forward direction, the p_t^{miss} and Q^2 efficiencies should indeed be similar.

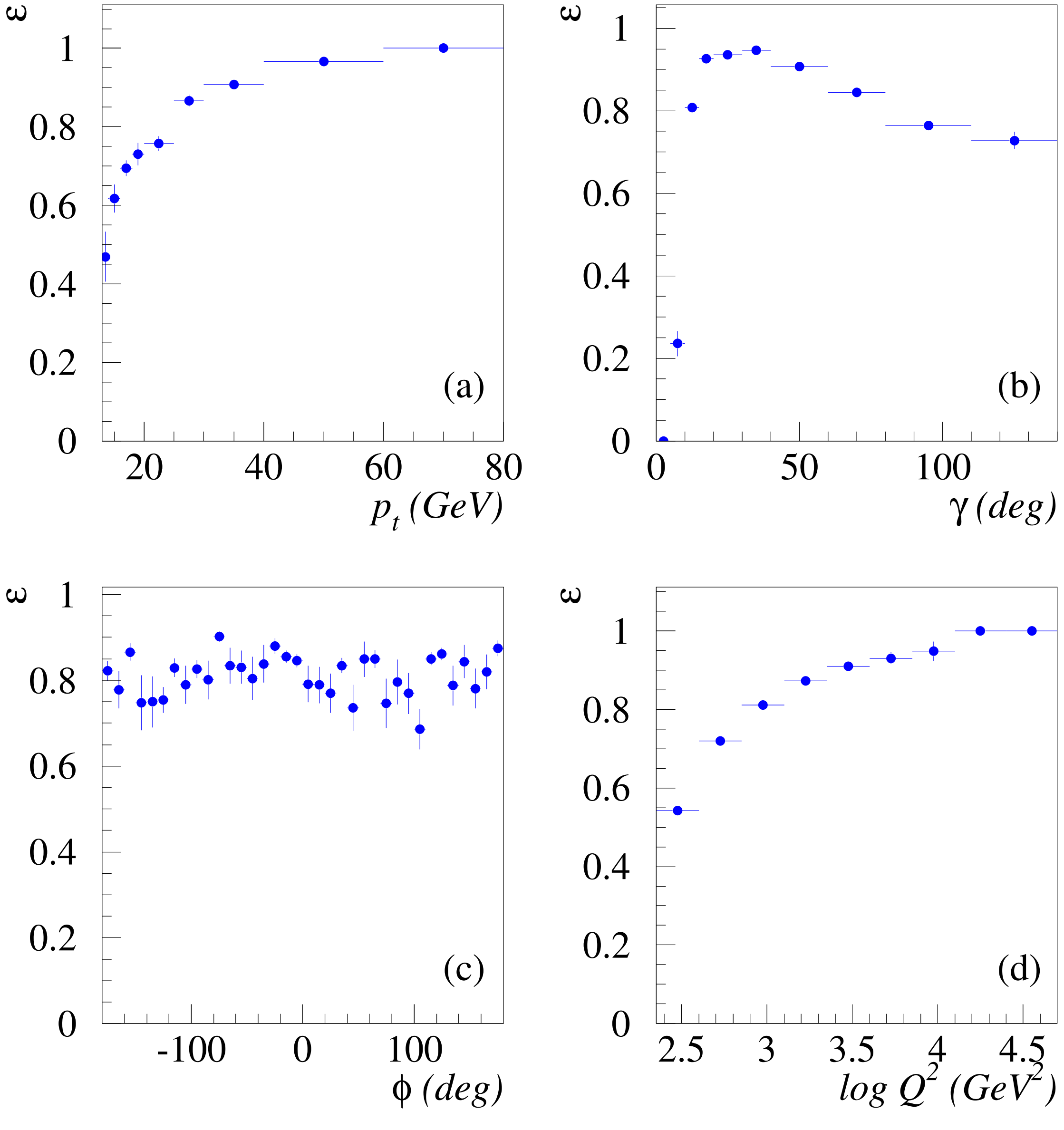

Figure 4.2: Global trigger efficiencies of combined sub-triggers 66, 67, 71, 75 and 77 as a function of (a) $p_t^{miss} (= p_t)$, (b) the inclusive hadronic angle γ_{had}, (c) the azimuthal angle ϕ and (d) Q^2, calculated using pseudo CC data from 1998 - 1999.

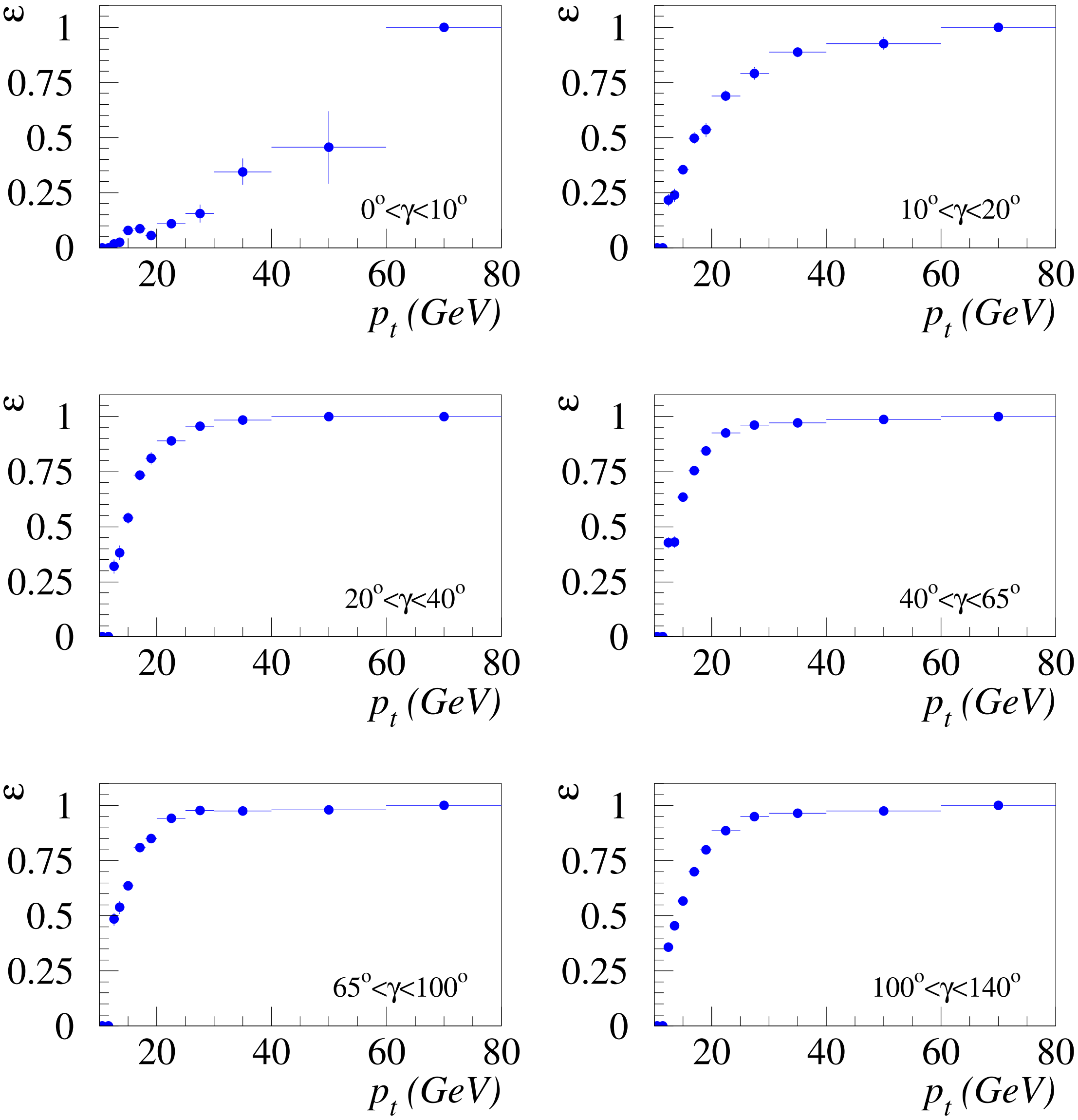

Figure 4.3: Trigger efficiencies as a function of $p_t^{miss}(= p_t)$ in bins of increasing γ_{had}, calculated using pseudo CC data from 1998 - 1999.

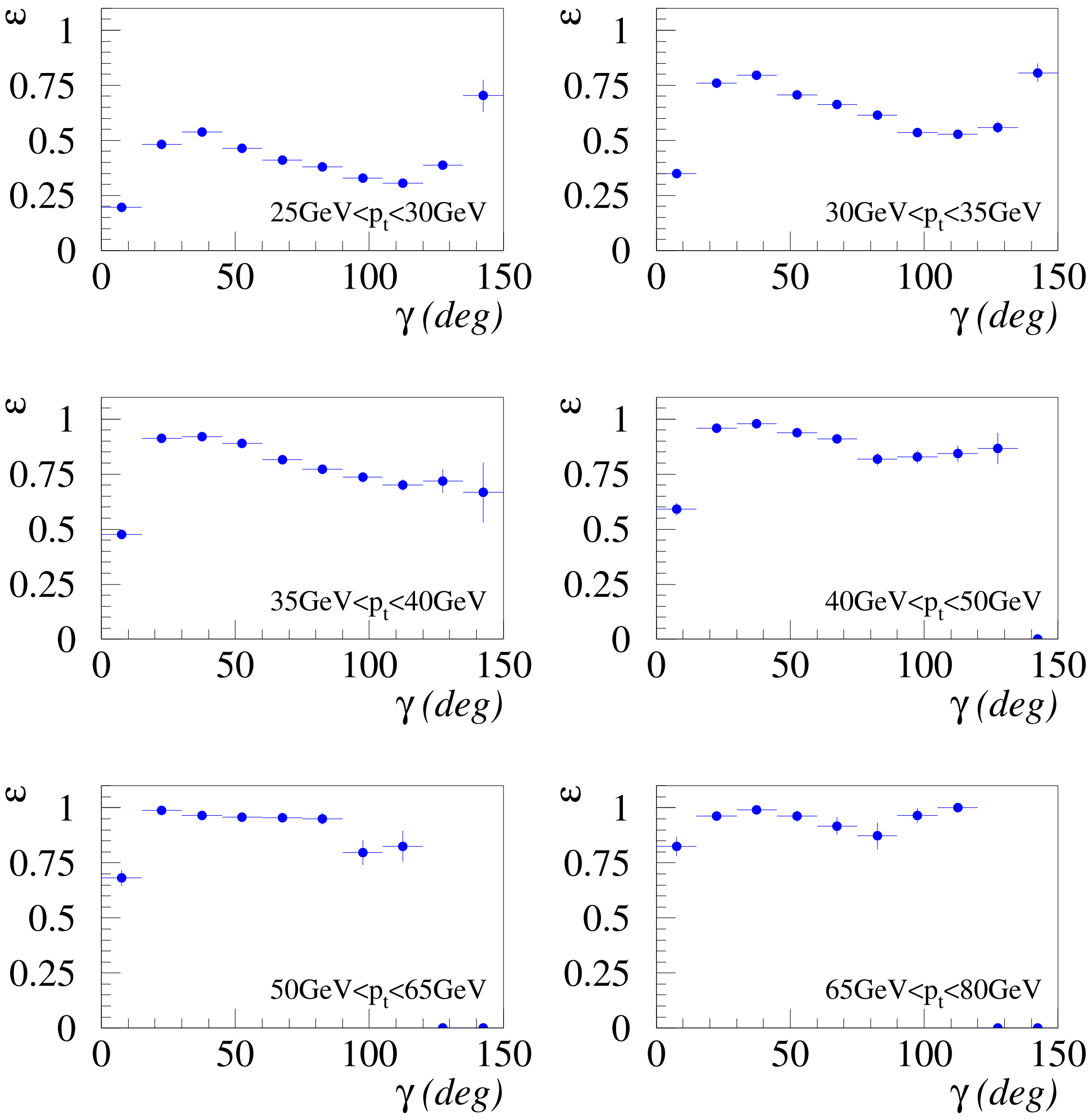

Figure 4.4: Trigger efficiencies as a function of γ_{had} in bins of increasing $p_t^{miss} (= p_t)$, calculated using pseudo CC data from 1998 - 1999. Efficiency values of 0 are due to the total absence of pseudo CC data within this particular kinematic range.

4.4 Studies on Increasing Efficiency

As the previous figures have shown, the triggers used for the identification of CC events have regions of considerable inefficiency. This section describes studies designed to develop methods of improving these regions of inefficiency and extending the phase space available for the measurement of the CC cross section. Two different techniques are used: a data analysis method using pre-selected low Q^2 NC events and a simulation of the effects of altering hardware trigger thresholds.

4.4.1 Low $\mathbf{Q}^2$ Neutral Current method

This study focusses on the trigger efficiencies at low values of p_t^{miss} and attempts to optimise and extend this region. The method involves the use of a selection of NC events in which the electron is found in the SPACAL - typically low Q^2 NC events. It is possible to entirely neglect the electron in these events to simulate CC events; the information about the electron is contained entirely within the SPACAL and is therefore independent of the hadronic final state which will mimic the final state of a CC event at low p_t. These events are analogous to those in the pseudo CC sample except that they cover a lower range in p_t.

These events are passed through the CC trigger selection and, using the entire sample of low Q^2 NC events as the denominator, the trigger efficiency is made in an identical way to that described in eqn. 4.1. The efficiencies of the low Q^2 NC sample and the pseudo CC sample are compared in the region of p_t available to both ($p_t \sim 15$ GeV) and found to be consistent. The efficiency measurement is then made at lower values of p_t using the low Q^2 NC sample.

Fig. 4.5 shows the trigger efficiency measured using both the pseudo CC sample for 12 GeV $< p_t <$ 80 GeV, and the low Q^2 NC sample for 7 GeV $< p_t <$ 20 GeV. The study indicates that it would indeed be possible to use this method of trigger efficiency calculation to measure the CC cross section over a range in p_t as low as 8 GeV. The efficiency falls to approximately 30% at the lowest measured values of p_t but these results are well understood and convincing since the statistical sample of low Q^2 NC events is relatively large.

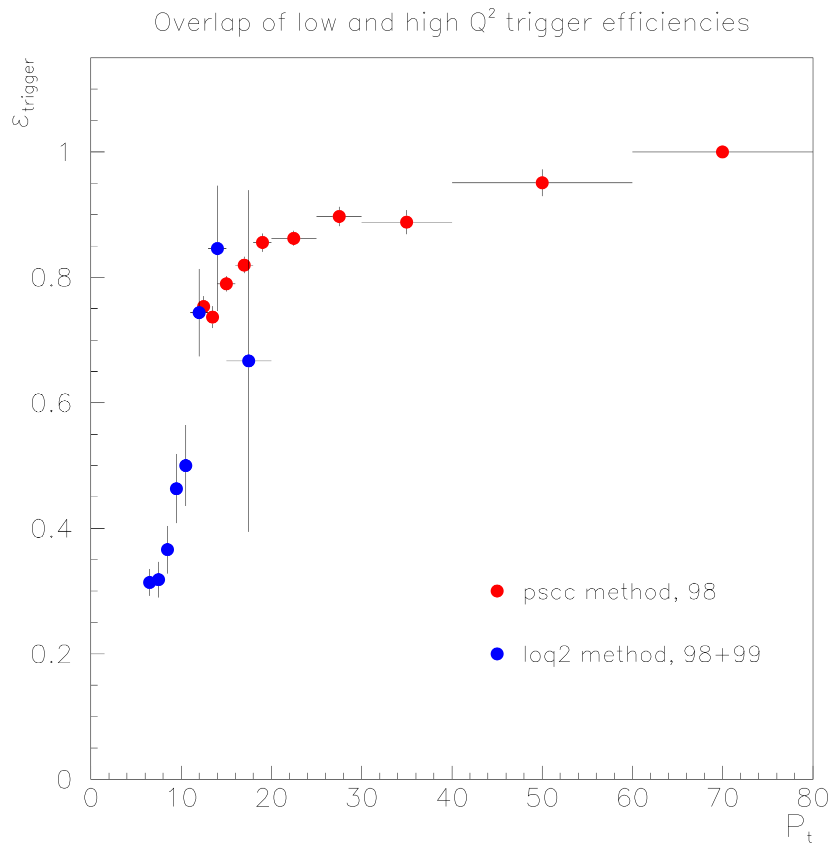

Figure 4.5: Trigger efficiencies as a function of p_t^{miss} (in GeV) demonstrating the possibility of using low Q^2 NC data (blue points, below p_t^{miss} = 20 GeV) to extend the range in p_t^{miss} currently available for the CC cross section measurement using pseudo CC data (red points, above p_t^{miss} = 12 GeV).

4.4.2 The *LAr_Etmiss* Trigger Element Optimisation method

To improve the performance of the triggers it is necessary to make modifications to the software set up of the triggers themselves and to optimise the information available from the detector. In two of the three CC specific STs, **ST 66** and **ST 77**, the *Etmiss* TE is the main component. Hence, the conclusion can be drawn that the most effective TE to optimise for an increase of efficiency in the low p_t region is this *Etmiss* TE.

The challenge is to increase the efficiency of the triggers and simultaneously to ensure that there is no increase increase in background acceptance which would lead to unacceptably high trigger rates. The rate of any trigger should be ∼ 1 Hz with or without a pre-scale.

This optimisation can be done using a tool called 'TTNT' [29] - an interface of the LAr trigger software package into the standard data analysis framework. TTNT simulates access to and manipulation of the thresholds set for each part of the LAr trigger, using an existing pseudo CC sample. This tool gives access to the e.m. ADC (Analogue to Digital Converter) counts and hadronic ADC counts assigned to each cell, the sums of counts per big tower and the global sums of all counts. One count corresponds to an energy of 0.125 GeV.

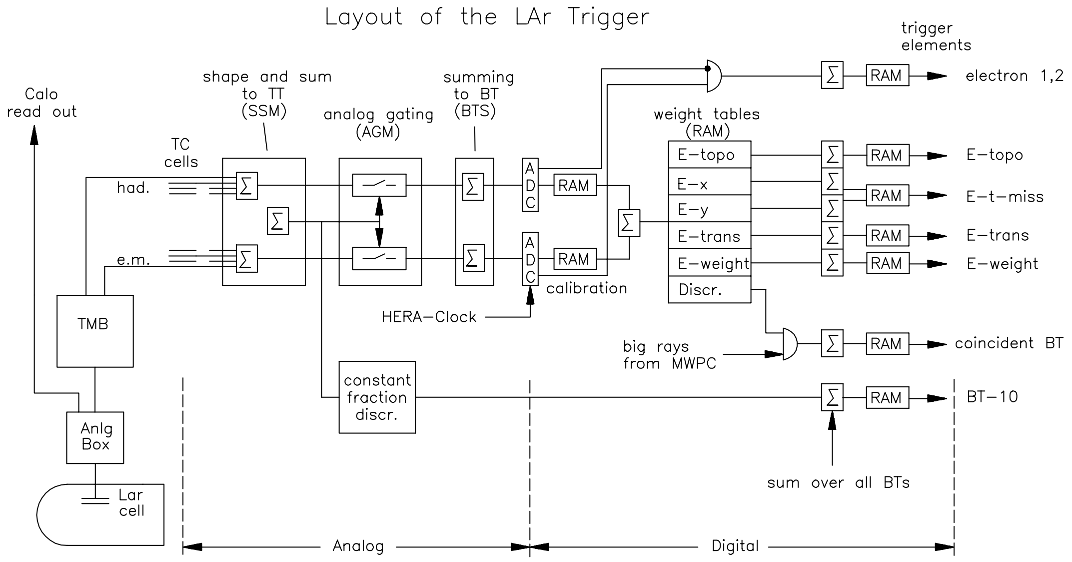

Figure 4.6: Schematic of the layout of the LAr trigger electronics. The trigger elements are output on the right hand side of the diagram.

A schematic diagram in fig.4.6 shows the layout of the electronics of the LAr trigger. The information gathered from each LAr cell is, in effect, used twice. Information is sent both to the trigger system and the calorimeter read out (top left of fig.4.6) where the energy measurement is made, independent of the trigger. For the trigger part, the LAr cell signals follow the path shown from left to right in the diagram. The analogue signals from the EM and HAD parts are required to exceed individual and summed analogue gating module (AGM) thresholds. They are then summed into BTs and the resulting signal is passed through an analogue to digital converter. The digital output is calibrated and this calibrated BT signal is compared to reference tables for typical energy signatures and weighted according to particular distributions. Finally, the weighted signals from all the BTs are combined and if this signal exceeds a global threshold for any TE, the TE is set.

Threshold	**em**	**had**	**BT1**	**BT2**	**BT3-14**	**G(l,m,h)**	**Rate inc.**	ϵ
Old	6	5	256	256	0	38,44,52	1	50%
New	6	5	256	8	8	38,44,52	1.08	57%

Table 4.1: List of original and revised thresholds, the relative rate increase and the efficiency of each scenario. **em**(**had**) is the threshold number of e.m. (had) counts, **BT** are the Big Tower threshold counts, **G** is the global threshold for low, medium and high settings and ϵ is the trigger efficiency for the Q^2 = 300 GeV^2 bin.

To establish optimised threshold values, systematic variations were applied to each component, shown in table 4.1, and comparisons made to the original until the optimal combination of low rate increase and high efficiency increase was found. Information given in the table details the new old and new threshold settings for the *Etmiss* TE: **em** and **had** are the AGM threshold values, **BT1 - 14** are the BT thresholds (see fig. 4.1 for reference to positions of 1 to 14) and **G** are the global thresholds. Finally, the relative rates and inefficiencies are given. The efficiency is quoted for a particular Q^2 bin which corresponds to events at low p_t^{miss}.

The results of the optimisation study show a rate increase of approximately 8% for an increase in efficiency of 7%. This equates to an increase in the number of accepted pseudo CC events from 1121 to 1270 from the total sample used. Fig. 4.7 shows the overall effects of these changes in terms of p_t^{miss} and γ_{had}; a considerable improvement is observed in both distributions at low p_t^{miss} and γ_{had}.

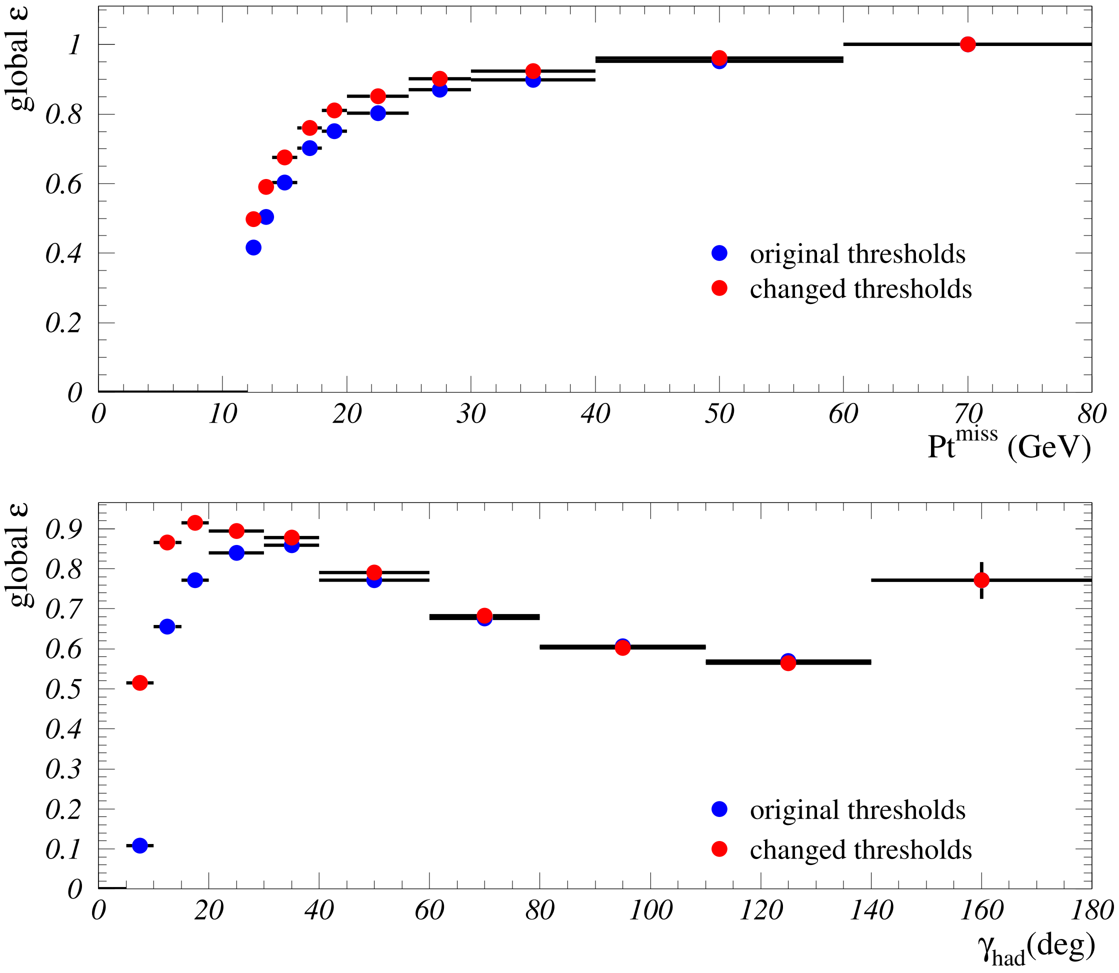

Figure 4.7: Plots showing trigger efficiencies calculated using the original threshold settings (blue/dark points) and with the new threshold settings (red/light points) as a function of p_t^{miss} (top plot) and γ_{had} (bottom plot).

4.5 Energy measurement

The energy measurement itself is the most important aspect of the analyses to follow, which depend almost entirely on the accurate determination of the kinematic variables of the final state. The quantities $E - p_z$ and p_t are reconstructed from energy and momentum measurements from the LAr calorimeter, the tracker (CJC) and the backward SPACAL calorimeter. For example, Σ_{tot} is constructed from 4 components:

$$\Sigma_{tot} = (\Sigma_{LAr} - \Sigma_{noise}) + \Sigma_{tracker} + \Sigma_{SPACAL} \tag{4.3}$$

In the CC and radiative CC analyses the contribution to this sum from the SPACAL is negligible because the selection of $p_t > 12$ GeV (see chapter 6) excludes the low-x region, in which the hadronic final state may enter the backward apparatus.

Information from more than one detector component is used to optimise the resolution and angular coverage of the energy measurement. Information from either the LAr calorimeter or the trackers alone is insufficient: tracking information is useful for charged particles with quite low energy but neutral particles are not detected and high energy particles leave a very straight track making curvature measurements very difficult; calorimeter information is excellent for high energy particles but low energy particles may curve around considerably in the trackers allowing much more accurate measurement to be made with the trackers than by using the low energy calorimeter deposition. However, by using more than one detector component, the possibility of double counting of energy is admitted. An algorithm to combine the information from calorimetery and tracking information whilst minimising double counting has been developed [30].

Σ_{noise} is a correction applied to energies in the LAr calorimeter to correct for two main sources of spurious energy deposition. Firstly, some small quantity of electronic noise may survive the online noise suppression algorithm. Although any such remaining energy will be small, it may still introduce a significant bias into the measurement of $E - p_z$ in very low y events if the noise is in the backward region. Secondly, particles may interact in material before reaching the calorimeter and be deflected from their original direction, resulting in low energy isolated energy deposits. Both sources of noise are suppressed by a topological algorithm [31].

In order to ensure the energy measurement is as accurate as possible, studies have been done to verify how well various aspect of the measurements using the trackers and

LAr are understood. These studies relate to the alignment between the trackers and the LAr calorimeter, and to the calibration of both the electromagnetic (EM) and hadronic (HAD) part of the calorimeter. Full descriptions of all these studies are available in reference [43].

Alignment

The procedure for connecting tracks and energy clusters relies on the the correct assumption of the position of the Central Trackers with relation to the LAr calorimeter. Using the scattered electron from NC events, a study to determine the alignment constants has been done [27] comparing the polar and azimuthal angles of the LAr energy cluster with track angles measured in the CTD. The alignment of the trackers and the LAr calorimeter has been established to within 1mm in the x, y and z directions.

Calibration

The LAr calorimeter, as mentioned in section 2.2.3, is a non-compensating calorimeter and, as such, requires separate calibration of the energy scales of electrons and hadrons to improve the energy resolution.

- **Electron energy measurement**
  The energy of any electron is corrected for losses in the material in front of the calorimeter. In addition to this correction, a further correction is made to allow for possible energy loss in ‘crack’ regions of the detector (see section 2.2.3). NC DIS events and QED-Compton events[1] are used to determine the calibration constants for the LAr. The calibration constants are determined for finely segmented z and ϕ regions by comparing the energy of the electron measured in the LAr to the energy calculated with two other independent reconstruction methods (the double angle (DA) method and the Omega (ω) method [34]) and comparing the results for data and MC. An energy scale uncertainty can then be assigned for each wheel. This varies between ± 0.7% in the backward region and ± 3% in the forward region.

---

[1] QED-Compton events have an electron and photon in the final state.

- **Hadronic energy measurement**

  Weighting algorithms are applied to the hadronic energy clusters as standard within H1 [32] [33]. Additional studies based on the use of NC events have been done to establish an improved calibration over the weighting algorithms alone. The method used compares the transverse momentum $p_{t,e}$ of the scattered electron (after the above calibration) to the $p_{t,h}$ of the hadronic final state, which will generally be spread over more than one wheel and octant of the detector.

  The event 'pull' - a ratio of the projection of the $p_{t,h}$ in the direction of the electron, to $p_{t,e}$ - is calculated, as is the fractional contribution of $p_{t,h}$ from each wheel. The wheel-weighted pull average is determined for each wheel, for data and MC, and after several iterations the ratio of the two is taken to be the calibration factor. Investigation of the dependence of this ratio on various kinematic factors allows a systematic uncertainty on the relative hadronic energy scale of 2% to be quoted.

Chapter 5

Photon Identification

This chapter presents the procedure used to identify photons within CC events. The preselection process is described for photons in general and for photons within a basic CC event sample. The optimisation of the photon finder is described and the efficiencies of the photon finder are evaluated for the relevant region of CC phase space. The photon selection cuts applied to the final analysis are described in chapter 8.

5.1 Photon characteristics

The essential properties of photons which allow them to be distinguished from other particles are the following:

① they are electrically neutral and will either pass through the tracking chambers undetected, or convert to an electron-positron pair in the material prior to or within a tracking chamber and leave a signal;

② the energy of photons or electron-positron pairs is deposited primarily in the electromagnetic calorimeter.

These properties must be exploited in order to separate photons from other particles such as pions, kaons and electrons. There is an additional indicator available which gives an increased understanding of the type of energy cluster which may be a photon. Within the framework of this analysis, the following is crucial:

③ according to theoretical predictions for the production of radiative CC events [16], the photon radiated from the W will be separated from both the hadronic jet and the proton remnant.

5.2 Photon candidate preselection

Several requirements are made in order to select candidate photons from the generally large number of energy clusters in the detector for each event. For the purpose of this Monte Carlo study, it is necessary to define a 'well reconstructed' energy cluster: any cluster which satisfies $|\theta gen - \theta rec| < 2\sigma$ of a Gaussian fit is 'well reconstructed' (see fig. 5.1(a)), where θgen and θrec are the polar angle of a generated photon and a reconstructed cluster respectively. The peak in the middle of the distribution is due to clusters which occur at low values of θ which, as shown in fig. 5.1(c), are better reconstructed.

Cluster energy properties

Clusters are chosen with a minimum generated and reconstructed transverse momentum

$$p_t > 1 \text{ GeV} \tag{5.1}$$

reducing the contribution from badly reconstructed, low p_t clusters, shown in fig. 5.1(b). A minimum requirement is made on the percentage of the cluster energy deposited in the EM LAr calorimeter:

$$e.m.frac > 95\%. \tag{5.2}$$

An average of 6% of well reconstructed events with $p_t > 1$ GeV fail the e.m. fraction cut. For $p_t gen > 45$ GeV, this failure rate is 25%. However, an overall average of 43% of badly reconstructed events fail this cut. The distribution of the θrec versus θgen of the well and badly reconstructed events is shown in fig 5.1(c).

Cluster isolation criteria

Three different isolation requirements are made with respect to the candidate cluster and activity surrounding it, in the form of (i) other clusters, (ii) jets and (iii) tracks. In terms of the isolation requirements for acceptance of photons and electron-positron

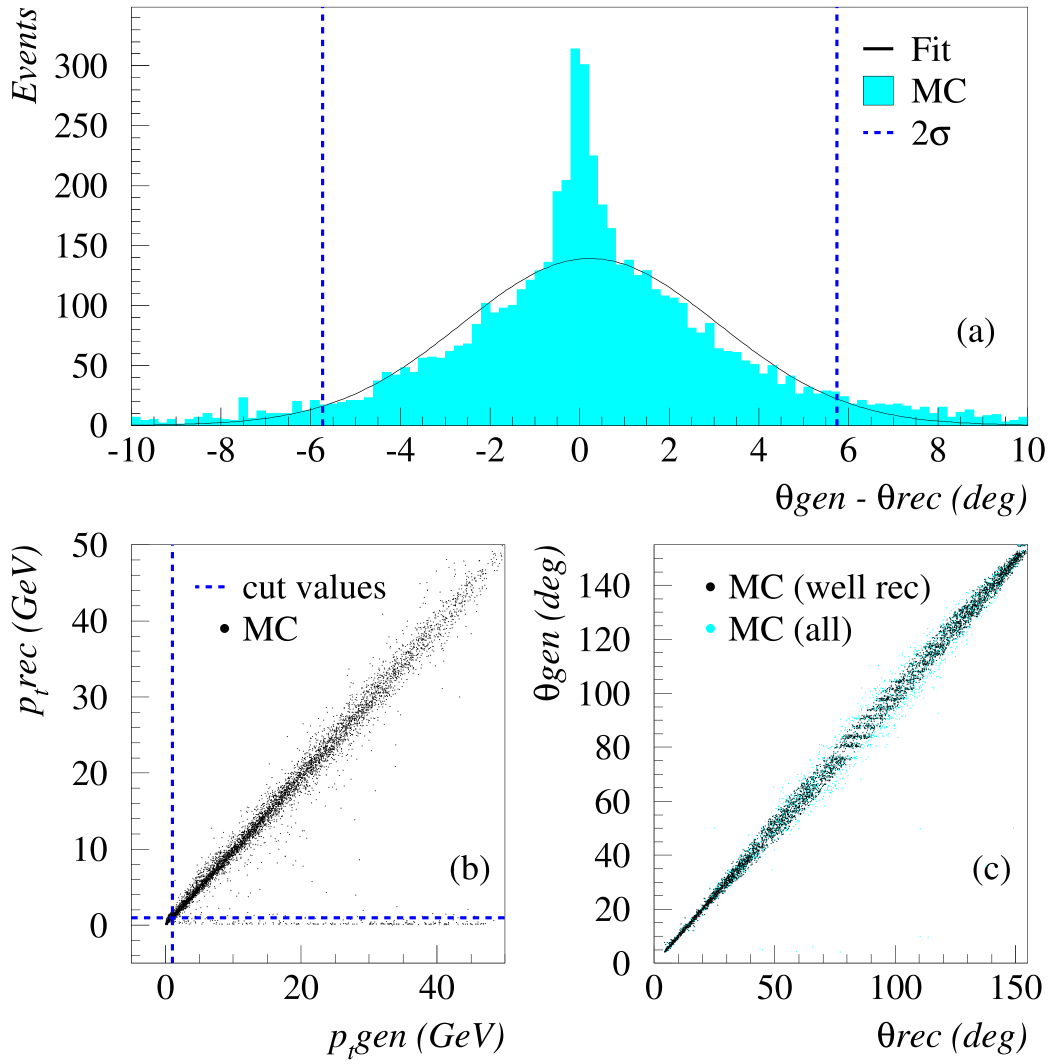

Figure 5.1: Plots showing (a) the distribution of $\theta gen - \theta rec$ of all candidates with $p_t > 1$ GeV, fitted with a Gaussian and with dashed lines at 2σ, indicating the boundary between well reconstructed and badly reconstructed clusters, (b) reconstructed versus generated p_t of photon candidates in a MC file of individual photons, with dashed lines indicating cuts made at $p_t = 1$ GeV and (c) the distribution of generated θ versus reconstructed θ of clusters: black dots are well reconstructed photons, light dots outside the black band are 'badly' reconstructed.

conversions, cluster and jet requirements are standard but the selection criteria are different for tracks.

(i) **Other clusters**

A cone R is defined in $\eta - \phi$ space around the candidate γ cluster, where

$$R = \sqrt{(\eta_\gamma - \eta_{clus2})^2 + (\phi_\gamma - \phi_{clus2})^2} \quad \text{and} \quad \eta = -1 \times \log(\tan \frac{\theta^\gamma}{2}).$$

'$clus2$' is the nearest cluster and a minimum separation between the candidate cluster and $clus2$, with a certain minimum energy, is made:

$$R > 0.25 \qquad \text{for} \qquad E_{clus2} > 0.5 \text{ GeV} \tag{5.3}$$

Any clusters with $E_{clus2} < 0.5$ GeV are neglected.

(ii) **Jets**

A similar isolation definition is made for the candidate γ clusters and jets in the event:

$$R = \sqrt{(\eta_\gamma - \eta_{jet})^2 + (\phi_\gamma - \phi_{jet})^2}$$

The jets are found using the kt algorithm [42] and have a minimum transverse momentum of 5 GeV. No minimum R separation requirement is made at this stage, but this definition is useful in section 8.2.

(iii) **Tracks**

Attempts are made to ensure that photon conversions are accepted as good photon candidates, but that scattered electrons are rejected.

(a) Photons Simple photon identification is made if no track with a transverse momentum above a threshold is found within a cone of isolation:

$$R = \sqrt{(\eta_{cluster} - \eta_{track})^2 + (\phi_{cluster} - \phi_{track})^2}$$

$$R > 0.25 \qquad \text{for} \qquad E_{track} > 0.8 \text{ GeV} \tag{5.4}$$

Any tracks with $E_{track} < 0.8$ GeV are neglected.

(b) Photon conversions These are accepted if the track has transverse momentum above the threshold set for simple photons ($E_{track} > 0.8$ GeV), but starts only in CJC2 (equivalent to a start radius of > 0.44m in the CJC). It is possible for these conversions to take place in the inside wall of CJC1 or 2, but by rejecting candidates with a track starting in CJC1, less than 5% of true[1] photons are lost. If a photon conversion is identified, no specific second track isolation requirement is made but the isolation can then be determined using the jet isolation criteria described above.

Of all well reconstructed photons, 5.3% convert at some point in CJC2, shown in fig. 5.2(a) as a function of the p_t of the photon candidate. Overall, 81% of events with a well reconstructed photon contain some track with $p_t > 0.8$ GeV. The distribution of events with and without conversions as a function of the polar angle of the photon candidate is shown in fig. 5.2(b) and the conversions are seen to be heavily peaked in the forward direction, as expected given the distribution of material within the detector.

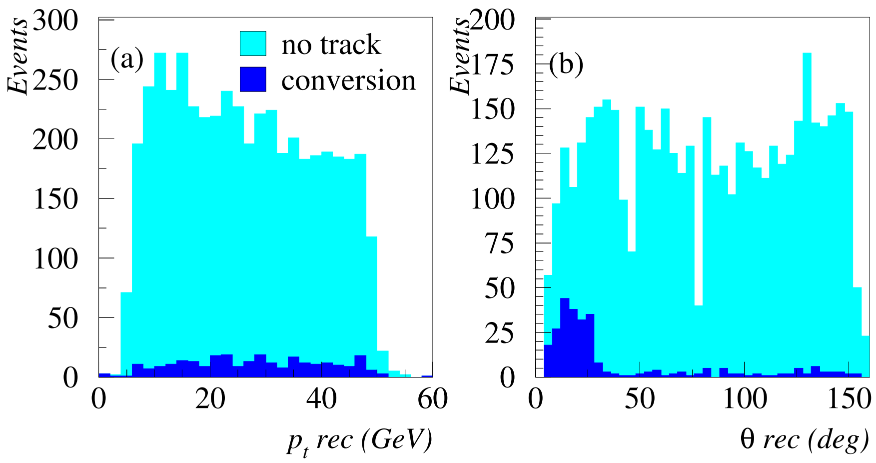

Figure 5.2: Plot showing number of events which have no associated track (light blue histogram), and those which do have a track (dark blue histogram) and are photon conversions, calculated from the `DJANGO` CC MC. These events are (a) uniformly distributed in p_t, but (b) heavily peaked at low θ (the forward direction) where photons pass through the end wall of the CJC.

---

[1] 'True' is synonymous with generated.

Detector acceptance

The angular acceptance of the photon finder is limited (eqn. 5.5) to

$$25^\circ < \theta^\gamma < 145^\circ \tag{5.5}$$

to ensure the photon:

(a) travels through the CJC tracking detector so conversions can be identified, reducing the risk of mis-identifying an electron as a photon;

(b) will be caught in the main barrel of the LAr calorimeter, within the region in which the calorimeter has both an electromagnetic and a hadronic part.

Summary

Table 5.1 summarises the properties which an energy cluster must possess in order to become a photon candidate.

Property	**Cut**
p_t of cluster	> 1 GeV
e.m. fraction of total energy	$> 95\%$
Isolation criteria:	
Nearest cluster energy	> 0.5 GeV
Cluster - γ candidate separation R	> 0.25
Anti-electron track selection:	
p_t track	> 0.8 GeV
Track start radius	< 44 cm
Track - γ candidate separation R	> 0.25
Detector acceptance:	
Polar angle θ^γ	$> 25^\circ$
Polar angle θ^γ	$< 145^\circ$

Table 5.1: Selection criteria for photon candidates.

The photon finder will select all candidates which pass the preselection criteria. They are ordered and labelled with respect to decreasing energy. The 10 candidate photons with the highest energies are kept for each event. The properties of all these photons, and the number of candidates per event, are shown to agree well in all respects between the data and Monte Carlo (fig. 5.3) when normalised to the luminosity of the data sample.

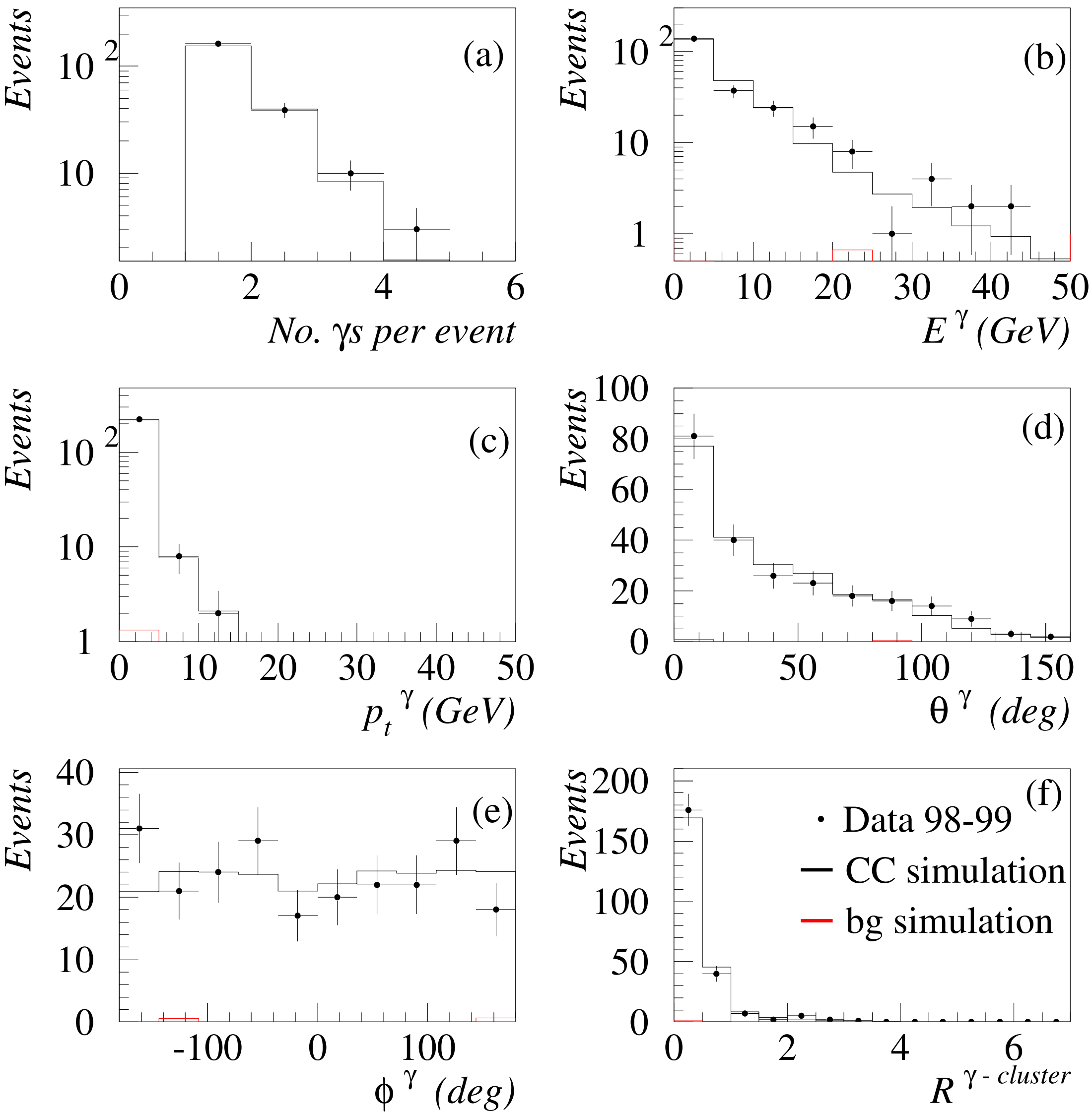

Figure 5.3: Monitor plots showing data - Monte Carlo agreement. Black points are 98-99 e$^-$ data. The black (solid) line is the `DJANGO` CC MC and the red (light) line is the contribution from `DJANGO` NC and `PYTHIA` photoproduction MC. Plot (a) shows number of candidate photons per event, (b) shows the energy E$^\gamma$ for all candidates, (c) is the transverse momentum p_t^γ, (d) is the polar angle distribution θ^γ, (e) is the azimuthal angle distribution ϕ^γ and (f) is the cone R separation in $\eta - \phi$ between the candidate clusters and the nearest cluster with energy > 0.5 GeV.

5.3 Photon finder efficiency evaluation

The efficiency of this photon finder is evaluated using `DJANGO` CC MC with $p_t^{miss} > 25$ GeV for the conditions summarised previously in table 5.1. The results of this efficiency evaluation are shown in fig. 5.4 for all photon candidates as a function of (a) polar angle θ^γ and (b) transverse momentum p_t^γ. The efficiency as a function of θ^γ is shown to vary between 65% and 80% and shows no strong systematic variation. In terms of p_t^γ, the efficiency is 94% in the lowest p_t^γ range but decreases rapidly to ~60% as p_t^γ increases. This is due primarily to the inefficiency of the $e.m.frac$ cut at high p_t^γ.

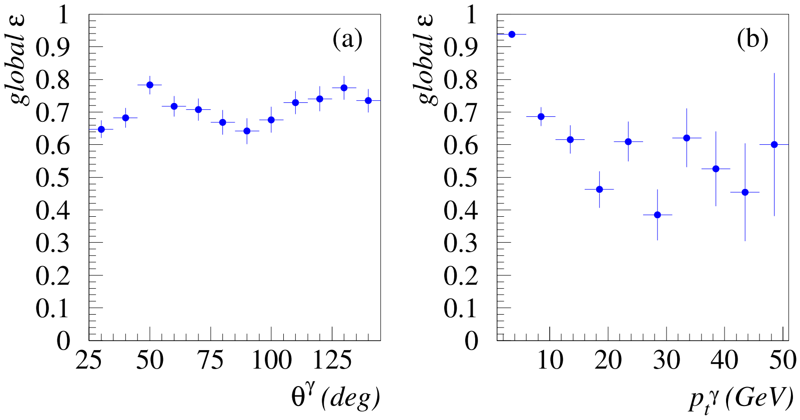

Figure 5.4: The efficiency of the photon finder as a function of (a) polar angle θ^γ and (b) transverse momentum p_t^γ, evaluated using the `DJANGO` CC MC with $p_t^{miss} > 25$ GeV.

The efficiency of this photon finder is verified within the framework of the radiative CC analysis in section 9.1.2.

Chapter 6

Charged Current Event Selection

Events at HERA resulting from the process $ep \to \nu X$, where a W boson is exchanged, have a characteristic topology. The topology is that of a hadronic jet and an imbalance of (also referred to as 'missing') transverse momentum due to the neutrino escaping undetected. A search is performed for events of this topology and it is shown that by far the largest contribution to the resulting event sample is indeed charged current events. However, this does not preclude the contribution to the event sample of other types of event, photoproduction interactions for example, or even something more unusual, but for the sake of simplicity this analysis is called the 'inclusive charged current' (CC) analysis.

This chapter describes the process by which events are selected for the CC analysis. The phase space cuts, the general selection for all CC type events, the rejection of background from this sample and the efficiencies and calibration are described in detail. This analysis uses all the data taken by H1 from 1994 onwards. The data are split into three different samples, relating to the different beam particles and beam energies with which HERA has run (table 6.1).

Sample	**Years**	**COM (GeV)**	**Lepton beam**	**$\mathcal{L}$ (pb^{-1})**
A	1994 - 1997	820	positron	35.7
B	1998 - 1999	920	electron	16.4
C	1999 - 2000	920	positron	62.9

Table 6.1: Data samples: the years, centre of mass (C.O.M.) energy, lepton beam type and integrated luminosity relating to each sample.

Unless otherwise stated, all distributions and other plots in this chapter use data sample **B**. Differences between data samples, where they arise, will be shown.

6.1 Phase space

The phase space selected for this analysis is designed to be appropriate for both the standard CC analysis and the radiative CC analysis, described in chapter 8. Inelasticity cuts (eqn. 6.1) ensure the resolution of the event kinematics is good and a Q^2 cut (eqn. 6.2) that the analysis takes place over the 'high Q^2' domain (fig 6.1). Finally, a cut is applied to the transverse momentum (eqn. 6.3).

$$0.03 < y < 0.85 \tag{6.1}$$

$$Q^2 > 100 \ \mathrm{GeV}^2 \tag{6.2}$$

$$p_t^{miss} > 12 \ \mathrm{GeV} \tag{6.3}$$

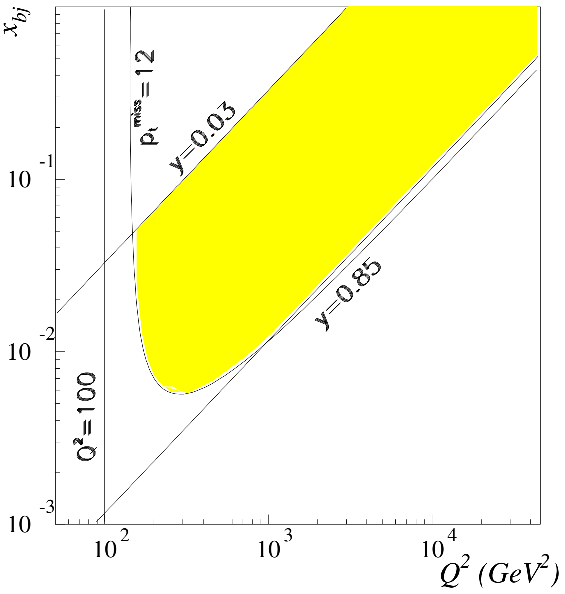

Figure 6.1: Kinematic plane available for CC analysis, marked by yellow (shaded) band.

6.2 Run selection and HV requirements

The status of both the HERA accelerator and the H1 detector are important for the quality of the data included in this analysis. Each 'run' of ep collisions is categorised corresponding to the quality of the data, defined by the status of critical detector components at the time. This analysis requires that the detector components which are essential for the safe identification of CC events have their high voltage (HV) on, i.e. the main calorimeters, the central tracking chambers, the luminosity and time-of-flight systems. Fig. 6.2 shows the number of events per nb^{-1} for sample B (top plot) and C (bottom plot) which satisfy these quality criteria. Also shown is the average for each data set, which highlights the obvious difference in event yield for the different beam types. An average of 0.039 events per nb^{-1} for running with electron and proton beams, and 0.018 events per nb^{-1} for running with positron and proton beam: a factor of ~ 2, as expected (see section 1.1.1).

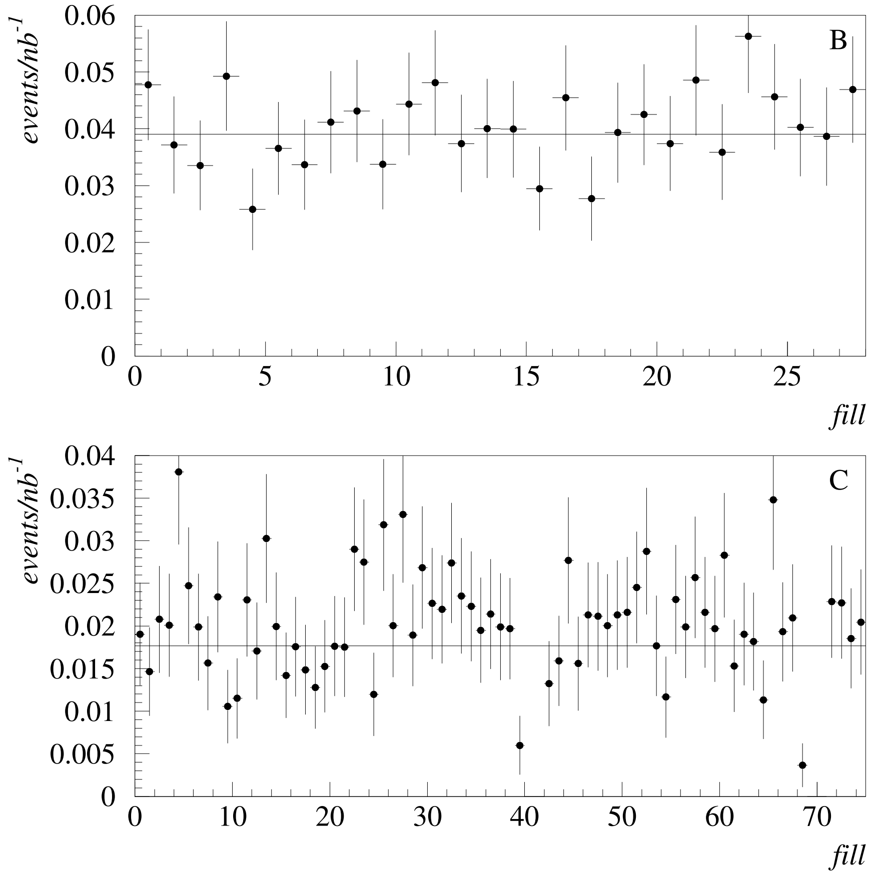

Figure 6.2: Number of CC events found per nb^{-1}, by fill, for samples B (1998-9) and C (1999-2000). Solid line is a fit to the data.

Individual runs or fills may be rejected from the sample if there is a problem which may complicate the analysis. For example, runs tagged as containing coherent noise - electronic noise occuring in the same place repeatedly - throughout a significant proportion of the run will be rejected (see section 6.4).

6.3 Trigger

It is required that the events are triggered as described in section 4.1. The efficiencies of these triggers are described in section 4.2 and shown in fig. 4.2.

6.4 Non-*ep* background rejection

There are many different types of background events which may contribute to the CC event sample. These may be either *ep* physics events or non-*ep* background. These events are rejected using various methods which are optimised to identify events with the characteristic topology of each background type. The non-*ep* contribution and rejection methods are described below.

Vertex requirement

A cut on the event vertex position along the z-axis is applied around the nominal interaction point (eqn. 6.4). This cut allows for the interaction point to move slightly, whilst still reducing background caused by beam gas interactions.

$$-35cm < z_{vertex} < 35cm \tag{6.4}$$

Cosmic Ray and Halo Muon rejection

A substantial proportion of the background interactions are due to cosmic rays, and 'halo muons' from the proton beam. Cosmic rays are identified by energy deposits left in the instrumented iron, LAr calorimeter and the central tracking detectors. These deposits are usually made in straight lines, approximately perpendicular to the beam axis and will normally make up a large proportion of energy in the detector even if they overlay a genuine physics event. Halo muons are detected in the LAr calorimeter, instrumented iron and the SPACAL. They leave traces of energy parallel to the beam axis and, again, will make up a large proportion of the energy detected in an event.

It is important to assess the proportion of genuine CC events which are selected for rejection by the cosmic or halo muon background finders [44] in order to be able to correct for this. Therefore, the efficiency of the topological background finders at *not* wrongly identifying true CC events as background is determined (fig.6.3) using both `DJANGO` CC MC and pseudo CC data. Both methods of calculation give efficiencies of 93% or above in every bin, with the exception of the lowest, and together give an average efficiency of 96% overall. Due to small differences in the efficiencies calculated with the two methods, caused primarily by the pseudo CC sample having a factor $\sim$ 10 fewer events than the MC sample, a systematic error of 3% is assigned.

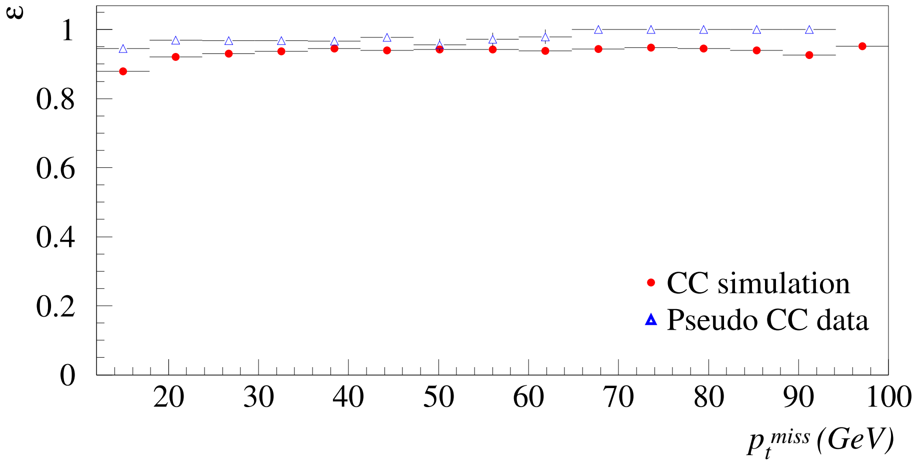

Figure 6.3: Efficiency ε of cosmic ray and halo muon background finders versus p_t^{miss} of the event, calculated with `DJANGO` simulation (red dots) and pseudo CC data (blue triangles).

Noise rejection

Events containing contributions to the p_t^{miss} from coherent noise in the LAr calorimeter are rejected from the sample by algorithms designed to recognise the characteristic patterns of noise in the detector. Events with one 'hot cell', where more than 90% of the p_t^{miss} is measured in one LAr cell, are rejected.

6.5 Physics (ep) background rejection

The main physics contamination of the CC sample comes from photoproduction and NC events. These may be present in the sample if their energy is measured inaccurately due to detector acceptance limitations or unidentified electrons which would allow them to have an imbalance of transverse momentum, i.e. p_t^{miss}. These background contributions are much more significant at low values of transverse momentum.

The energy flow isotropy cut

In order to reject these processes a method has been devised [43] which measures the sum of the transverse momentum flow parallel to the transverse momentum component of the hadronic final state (V_p) and the sum of that opposite, or anti-parallel (V_{ap}),

$$V_p = \sum_i \frac{\overrightarrow{p}_{t,h} \cdot \overrightarrow{p}_{t,i}}{\overrightarrow{p}_{t,h}} \qquad \text{for} \qquad \overrightarrow{p}_{t,h} \cdot \overrightarrow{p}_{t,i} > 0 \tag{6.5}$$

$$V_{ap} = -\sum_i \frac{\overrightarrow{p}_{t,h} \cdot \overrightarrow{p}_{t,i}}{\overrightarrow{p}_{t,h}} \qquad \text{for} \qquad \overrightarrow{p}_{t,h} \cdot \overrightarrow{p}_{t,i} < 0 \tag{6.6}$$

where i represents the individual particles belonging to the hadronic final state and h is the total hadronic final state. V_{ap}/V_p is then a measure of the fraction of the total transverse momentum of the event which is in the opposite hemisphere of the detector to the hadronic final state. For CC events V_{ap}/V_p is small, 0.3 or less, but for NC or photoproduction events this number will be greater than 0.1 as their energy is distributed more isotropically in the detector, as fig. 6.4 illustrates. Therefore, a cut is made which is designed to suppress background and optimise the signal contribution:

$$V_{ap}/V_p < 0.15 \tag{6.7}$$

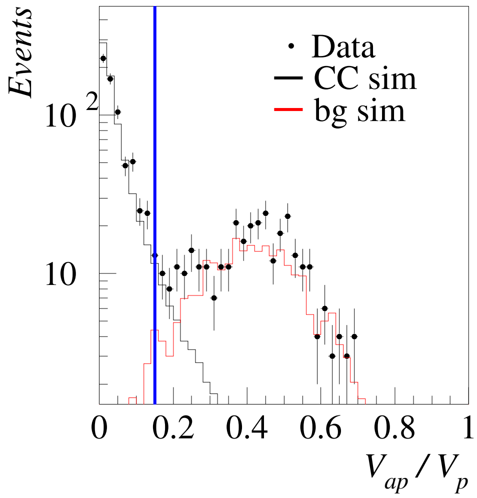

Figure 6.4: Plot of V_{ap}/V_p for $p_t^{miss} > 12$ GeV. The black dots are data, the black line is `DJANGO` CC simulation and the red (light) line is combined NC `DJANGO` and γp Pythia simulation. The blue vertical line represents the cut placed on V_{ap}/V_p for CC analysis.

The plug cut

The plug is a useful detector component for the rejection of photoproduction events. The azimuthal angle of the hadronic final state are calculated from the jet properties, and the azimuthal angle of any activity in the plug is determined. The difference in these angles is calculated, and a cut is made in the following way:

$$\Delta(\phi)_{jet,plug} < 150 + 30\left(\frac{p_t^{miss} - 12}{13}\right) \tag{6.8}$$

The cut has no effect above of $p_t^{miss} = 25$ GeV, which is appropriate since the contribution from photoproduction is very small above that threshold. CC events are usually contained in one region of ϕ in the detector. If plug activity is detected, it will normally be in the same half of the detector and, hence, have a small value of $\Delta\phi$. Photoproduction events, however, may have hadronic activity in one region of ϕ found in the LAr - implying p_t^{miss} - but the proton remnant caught in the plug must balance this and will, with increasing p_t, have increasing values of $\Delta\phi$ [45].

Cuts against W production and NC

So called 'W production' events, shown in fig. 6.5, may cause very small amounts of contamination in the CC sample as they have a very similar topology to that of a CC event. However, W production events contain a hadronic jet accompanied by a neutrino (which leaves the detector, indicated by missing p_t) but also contain an electron which is not co-planar to the jet. These events are rejected by identifying an electron candidate with an associated track [46]. This track must have a transverse momentum > 10 GeV and must be isolated[1] from the highest momentum jet by $R_{j-t} > 1.5$. None of the events which are found in the dedicated 'W production' analysis [21] are accepted by this analysis.

There is also possible contamination of the sample by NC events. These may have an electron which goes into a region of the calorimeter which is unable to accurately measure energy. These events are identified by a track with isolation[2] $R_{t1-t2} > 0.5$ from any other track. If this event then has $E - p_z > 45$ GeV, which is the difference of the energy of the electron candidate and its four-momentum along the beam axis, then the event is rejected. None of the events which pass the selection for the NC analysis [48] are accepted by this analysis.

---

[1] $R_{j-t} = \sqrt{(\eta_{jet} - \eta_{track})^2 + (\phi_{jet} - \phi_{track})^2}$, ϕ is the azimuthal angle and η is the pseudorapidity.

[2] $R_{t1-t2} = \sqrt{(\eta_{track1} - \eta_{track2})^2 + (\phi_{track1} - \phi_{track2})^2}$

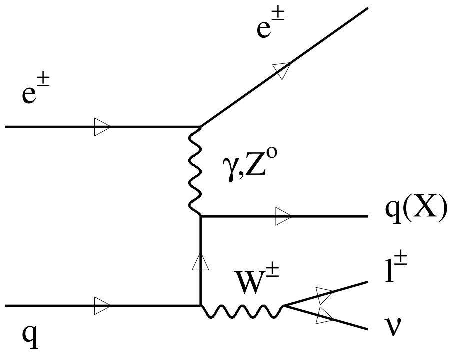

Figure 6.5: Feynman diagram of real W production.

Visual scan

The final stage of the background rejection process is to make a visual scan of all the events remaining in the sample. This ensures that no obvious background candidates (i.e. NCs, cosmics or halo-muons) satisfy the final selection. Of each data sample, approximately 5% of the sample remaining after all the above cuts are excluded 'by hand'.

6.6 Final sample

The final sample shows excellent agreement between data and simulation (figure 6.6). The contribution of *ep* physics background is shown to be small in all regions of phase space.

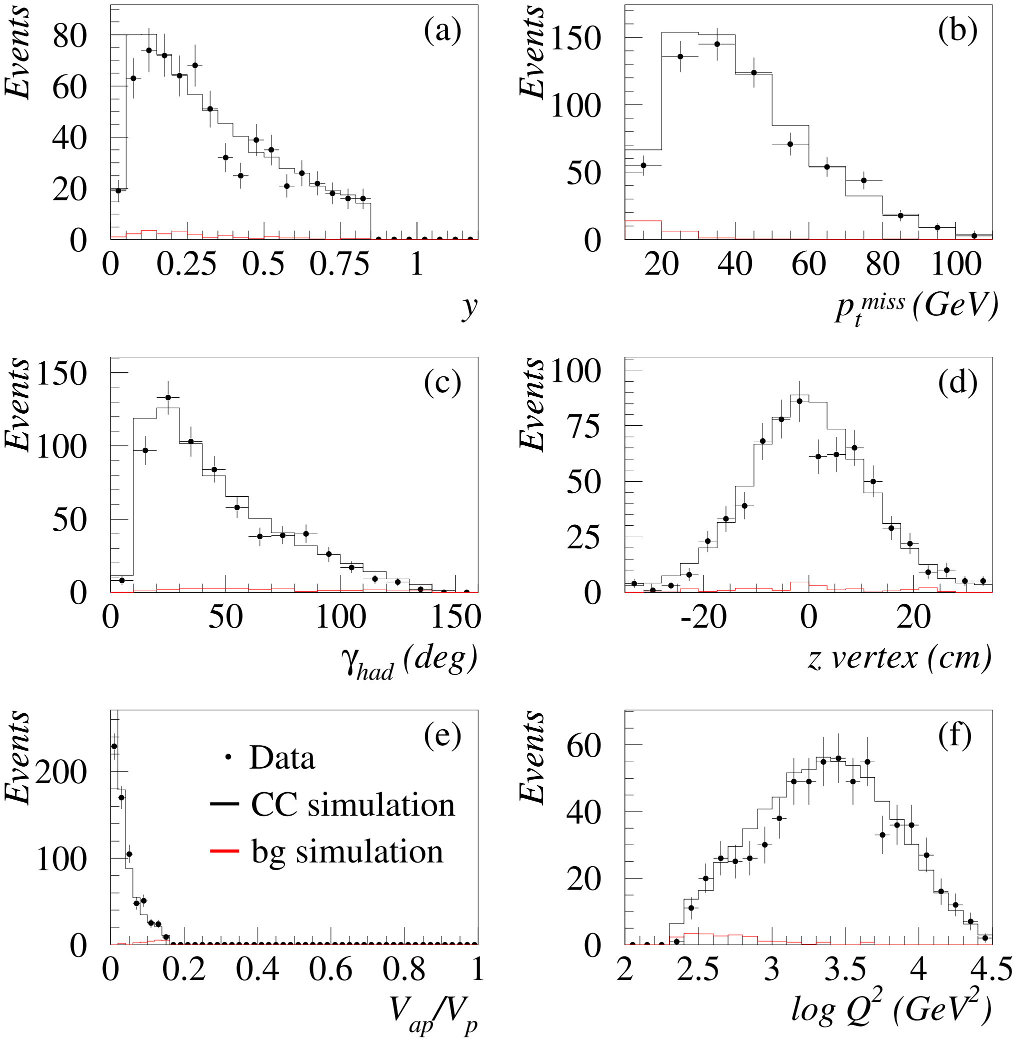

Figure 6.6: Monitor distibutions for the CC analysis. Black points represent the data, black line is `DJANGO` CC MC simulation and red (pale) line is combined background contribution of `DJANGO` NC MC and `PYTHIA` γp MC.Plot (a) shows the y distribution with cuts at 0.03 and 0.85. Plot (b) is the p_t^{miss} distribution above 12 GeV. Plot (c) is the mean angle of the hadronic final state γ. Plot (d) is the position of the z vertex in cm from the nominal interaction point. Plot (e) is the energy isotropy distribtion V_{ap}/V_p cut at < 0.15 and (f) is the log Q^2 distribution.

Chapter 7

Results of Charged Current Analysis

This chapter describes the method used to extract a physics measurement from the CC selection described in Chapter 6. Correction factors which are applied to the data in the final measurement are explained and the results of the analysis are presented.

7.1 Inclusive cross section measurement procedure

In order to make a measurement from the selected data sample it is necessary to convert the number of events found in certain regions of phase space into a measurement of the cross section with respect to one or more relevant parameters. These regions of selected phase space are 'bins' in the x, Q^2 plane and to each bin corrections must be made to compensate for several factors:

① for the emission or exchange of additional bosons, 'radiative corrections', and

② for smearing and acceptance effects due to detector inefficiencies or reconstruction methods.

This section describes these corrections and their application to the cross section measurements.

7.1.1 Binning

Due to the relatively low statistical precision available for the CC analysis in comparison to, for example, the NC analysis, it is possible to split the event sample into only 8 bins in Q^2 and 7 bins in x. The bin boundaries are:

$\log Q^2$	2.35 2.6 2.85 3.1 3.35 3.6 3.85 4.1 4.4
$\log x$	-2.0 -1.67 -1.33 -1.0 -0.75 -0.5 -0.25 0.0

The binning is chosen according to criteria which quantify how well events are found and reconstructed in each region of x, Q^2 space. These criteria are the purity $\mathcal{P}$, stability $\mathcal{S}$ and acceptance $\mathcal{A}$. They are measured as efficiencies and the `DJANGO` CC MC (see section 3.2) is used to calculate them.

The criteria are defined as:

$$\mathcal{P} = \frac{N_{rec+gen}(i)}{N_{rec}(i)} \qquad \mathcal{S} = \frac{N_{rec+gen}(i)}{N_{gen+sel}(i)} \qquad \mathcal{A} = \frac{N_{rec}(i)}{N_{gen}(i)} \tag{7.1}$$

where

$N_{rec}(i)$	is the number of events reconstructed in bin i
$N_{gen}(i)$	is the number of events generated in bin i
$N_{rec+gen}(i)$	is the number of events reconstructed and generated in bin i
$N_{gen+sel}(i)$	is the number of events generated in bin i and reconstructed in any bin

Fig. 7.1 shows the criteria plotted as a function of x in the Q^2 bins shown above. The requirements imposed are that, for each bin, the purity and stability must be greater than 30% and the acceptance greater than 20%. Any bin not passing these stated requirements is removed. The x and Q^2 measurement is made using the hadron method.

The purity and stability show very similar behaviour in all Q^2 bins: they start low at low x, increase and then decrease again at high x (with the exception of the two highest Q^2 bins which do not see this decrease at high x). The acceptance shows a similar shape profile but there is a general increase of the mean value from low x to high x. These particular shape profiles are due to the reconstruction method used - the only method available for CC analysis. The resolution at low x is poor, causing a decrease in purity as events tend to be assigned to the wrong bins, and at high x much of the hadronic final state will escape down the forward beam pipe, causing the measured p_t^{miss} values to be too low and inducing the observed decrease in stability.

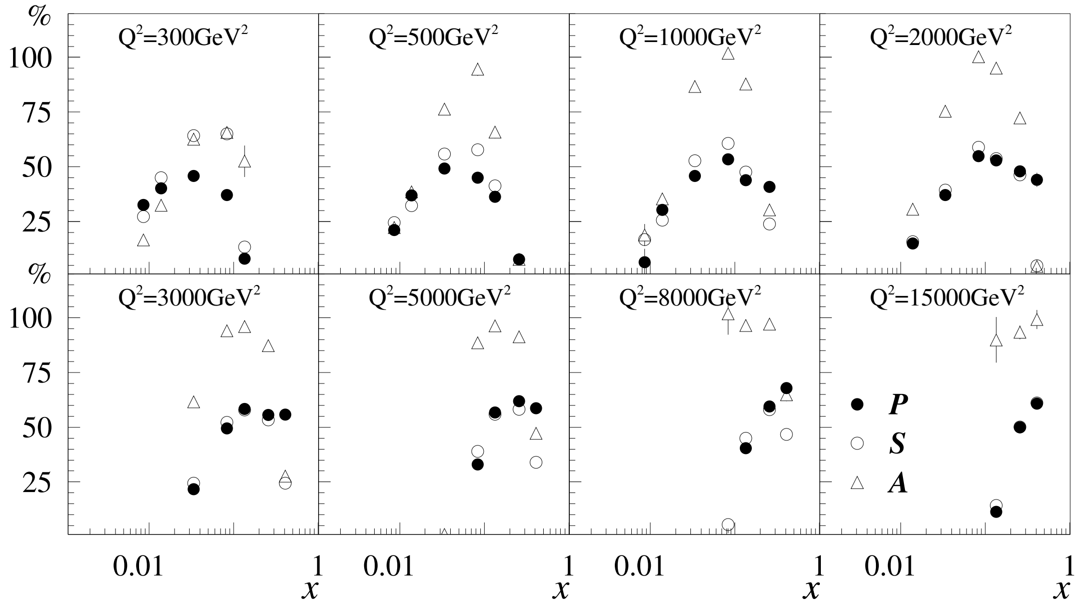

Figure 7.1: Bin selection criteria. Purity are the solid points, open points are the stability and open triangles are the acceptance. Evaluated using `DJANGO` CC MC generated events.

7.1.2 Radiative corrections

During a CC DIS process it possible that the incoming quark or lepton or outgoing quark will radiate one or more photons, called 'initial state' (ISR) or 'final state' (FSR) radiation, as described in section 1.2. In the case of ISR, this will result in the incident energy of the lepton being reduced from that which is assumed for the first order, or Born-level, calculation of the cross section. Any incorrect assumptions about the centre of mass energy will affect the reconstruction of the kinematic variables of an event.

The effects of radiation and their significance for the measurement can be separated into two parts: (i) The case of ISR and FSR: these are electromagnetic QED effects and their significance is dependent on the acceptance of the detector. The *bremsstrahlung* radiation is likely to be emitted collinearly to the beam with little angular separation. This radiation may not be detected if the photon follows the beam down the beam pipe. Hence the detector acceptance limitations are crucial in defining the necessary corrections to the measurement. There is a quark-lepton interference term which deals with interference from both lines. (ii) There is also a scenario whereby a purely weak process occurs.

A description of the differences between detector dependent and independent effects can be found in [49]; a full analysis of the radiative corrections to the CC analysis is found in [50]. In this analysis, only corrections to detector acceptance dependent effects are made to the cross section [27]. An uncertainty of 3% is assigned, as prescribed in [51].

7.1.3 Systematic uncertainties

Uncertainties which are introduced into the measurement by various aspects of detector dependence or selection inefficiency lead to systematic errors. Studies which relate to aspects of this analysis are discussed in earlier chapters (4.1, 4.5, 6). Other errors which are unrelated to the procedure used in this analysis but must be accounted for in the overall calculation are given in the following. All errors are added in quadrature and the number in square brackets refers to the section introducing the source.

Uncertainty	**Source**
	100% Correlated
1.5%	from luminosity measurement (not included in plots) [2.2.2]
25%	on energy identified as noise in the LAr calorimeter [6.4]
4 to 6%	on energy flow isotropy cut [6.5]
30%	on subtracted γp background contribution [6.5]
	Partially correlated
2%	on hadronic energy in LAr calorimeter [4.5] (quadratic sum of 1% correlated from reference scale and 1.7% uncorrelated from calibration method)
	Uncorrelated
3 to 8%	on trigger efficiency [4.2]
3%	on QED radiative corrections [7.1.2]
3%	on efficiency of non-ep background finders [6.4]
2 to 5%	on vertex finding efficiency [6.4]

Table 7.1: Table showing systematic uncertainties of the CC measurement.

The determination of these errors is also discussed in previous publications [43] [27]. The total systematic errors for the CC double differential cross section amount to $\sim$ 12%. For the single differential, $\mathrm{d}\sigma_{CC}/\mathrm{d}Q^2$, the errors amount to $\sim$ 8%.

7.1.4 Calculation of the cross section

The cross section is calculated for each individual x, Q^2 bin. The factors described in sections 7.1.1 to 7.1.3 above are applied to the data in the following way:

$$\frac{\mathrm{d}^2\sigma}{\mathrm{d}x\mathrm{d}Q^2} = \frac{N^{data} - N^{bg}}{\mathcal{L}.\mathcal{A}}.\delta^{bc}.\frac{1}{1+\delta^{RC}} \tag{7.2}$$

where

N^{data}	is the number of events in individual bin
N^{bg}	is the number of background events contributing to bin
$\mathcal{L}$	is the total integrated luminosity of sample
$\mathcal{A}$	is the detector acceptance for bin
δ^{RC}	is the radiative correction factor where $\delta^{RC} = \frac{\sigma_{rad}}{\sigma-1}$
δ^{bc}	is a bin centre correction to put the cross section in a bin i, of size $\Delta x_i = x_{i,max} - x_{i,min}$, $\Delta Q^2_i = Q^2_{i,max} - Q^2_{i,min}$, at the bin centre x_c, Q^2_c

$$\Rightarrow \delta^{bc} = \frac{\mathrm{d}^2\sigma^{MC}}{\mathrm{d}x\mathrm{d}Q^2}.\frac{\mathcal{L}^{MC}.\mathcal{A}}{N^{MC}_{rec}}. \tag{7.3}$$

All factors, with the exception of N^{bg}, have been determined using the `DJANGO` MC which contains radiative corrections. Therefore, eqn.7.2 can be simplified to the following:

$$\frac{\mathrm{d}^2\sigma}{\mathrm{d}x\mathrm{d}Q^2} = \frac{N^{data} - N^{bg}}{N^{MC}_{rec}}.\frac{\mathcal{L}_{MC}}{\mathcal{L}}.\frac{\mathrm{d}^2\sigma^{MC}}{\mathrm{d}x\mathrm{d}Q^2} \tag{7.4}$$

Equation 7.4 is the formula used to construct the double differential results seen in figure 7.4. The equations for the single differentials are defined as:

$$\frac{\mathrm{d}\sigma}{\mathrm{d}x} = \int_{Q^2_{min}}^{Q^2_{max}} \frac{\mathrm{d}^2\sigma}{\mathrm{d}x\mathrm{d}Q^2}\mathrm{d}Q^2 \qquad \frac{\mathrm{d}\sigma}{\mathrm{d}Q^2} = \int_{x_{min}}^{x_{max}} \frac{\mathrm{d}^2\sigma}{\mathrm{d}Q^2\mathrm{d}x}\mathrm{d}x \tag{7.5}$$

In order to construct fig. 7.6, the 'reduced cross section', all the kinematic factors are multiplied out of the double differential cross section as shown in equation 7.6.

$$\tilde{\sigma}_{CC} = \frac{2\pi x}{G_F}\left[\frac{Q^2 + M_W^2}{M_W^2}\right]^2 \frac{\mathrm{d}^2\sigma_{CC}}{\mathrm{d}x\mathrm{d}Q^2} = \phi^{+}_{CC}(1+\delta^{weak}_{CC}) \tag{7.6}$$

where

δ^{weak}	is the contribution from weak processes to the radiative corrections
M_W^2	is assigned the measured value of 80.4 GeV.

7.2 Results

The differential CC cross section is shown as a function of x in fig. 7.3 for $Q^2 > 1000$ GeV^2 and as a function of Q^2 in fig. 7.4 for $Q^2 > 100$ GeV^2. Data from both samples A (open squares) and B (solid squares) are plotted[1], as are the predictions of the Standard Model for e^-p scattering (upper solid line) and e^+p scattering (lower solid line $\sqrt{s} = 300$ GeV, dashed line $\sqrt{s} = 320$ GeV). Data and SM expectations show excellent agreement in all regions of x and Q^2. The cross section calculated using data from sample B is found to be larger everywhere than the cross section calculated with sample A.

The difference in magnitude of the differential cross sections as a function of x, shown in fig. 7.3, calculated using e^+p and e^-p is evident. The cross sections differ in magnitude by almost 200% at low x (≈ 0.03) and 400% at high x (≈ 0.4). As a function of Q^2, shown in fig. 7.4, they differ by approximately 20% at low Q^2 (≈ 100 GeV^2), increasing to approximately 500% at high Q^2 ($\approx 25{,}000$ GeV^2). The difference in the size of the cross sections is due primarily to the nature of the quark content of the proton: the sensitivity of the exchanged $W^\pm$ bosons to the different quark flavours which are probed, as discussed in section 1.1.1. The effect of the increase in centre of mass energy accounts for very little of the change in magnitude, as is indicated by the difference between the solid dark line and the dashed line in fig. 7.4.

Fig. 7.5 shows the ratio of the data to the SM expectation. The data are not systematically above or below the expectation. The measurement is well described over several orders of magnitude and the SM is shown to withstand this precision test.

The double differential CC reduced cross section is shown in fig. 7.6 in bins of Q^2 as a function of x. There is insufficient e^-p data to make a measurement in the lowest Q^2 bin. The data agree well with the SM expectation, shown as solid lines for the H1QCD fit [43] [48] for both e^+p and e^-p. The reduced cross section for sample B is consistently larger than that for sample A. Again, this is primarily due to the difference in the quark flavours probed by the exchanged boson, specifically the presence of 2 u valence quarks for every d in the proton.

The cross section values and their associated statistical and systematic errors for

---

[1] Reminder:

Sample **A**	1994 - 1997, e^+p and $\sqrt{s} = 300$ GeV
Sample **B**	1998 - 1999, e^-p and $\sqrt{s} = 320$ GeV
Sample **C**	1999 - 2000, e^+p and $\sqrt{s} = 320$ GeV

each running period are given in table 7.2. The cross section for e^-p data is larger than for either of the e^+p data sets, as is also shown in figs 7.3, 7.4 and 7.6. The differences in the cross sections for the two e^+p data samples are due to the difference in the COM energies.

Data Set	σ (pb)	$\delta\sigma$**(stat.)**	$\delta\sigma$**(sys.)**
A	21.5	± 0.9	± 1.4
B	43.1	± 1.8	± 1.6
C	34.3	± 0.9	± 1.6

Figure 7.2: CC cross sections for each data set with statistical and systematic errors.

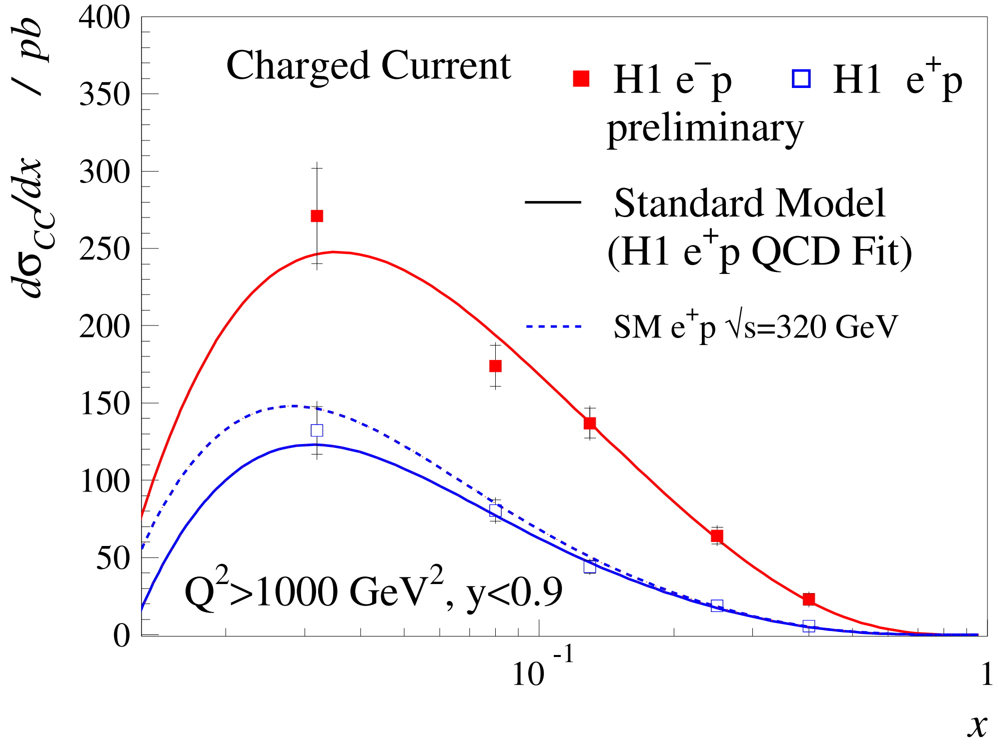

Figure 7.3: Single differential ($d\sigma/dx$) CC cross section for $Q^2 > 1000$ GeV^2. Red (solid) squares are 1998-9 e^-p data at $\sqrt{s} = 320$ GeV. Blue (open) squares are 1994-7 e^+p data at $\sqrt{s} = 300$ GeV. Red (upper) solid line is the SM expectation for e^-p at $\sqrt{s} = 320$ GeV. Blue (lower) solid line is the SM expectation for e^+p at $\sqrt{s} = 300$ GeV, and blue (dashed) line is the expectation for e^+p at $\sqrt{s} = 320$ GeV. The luminosity uncertainty of 1.5% is not included in the errors shown.

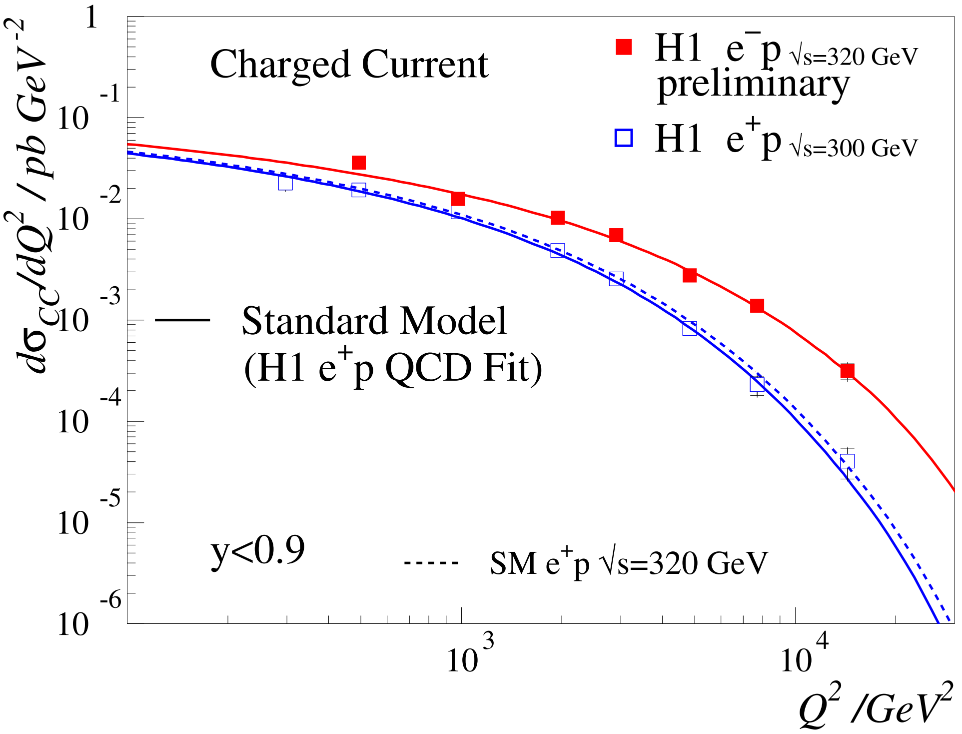

Figure 7.4: Single differential ($\mathrm{d}\sigma/\mathrm{d}Q^2$) CC cross section. Red (solid) squares are 1998-9 e^-p data at $\sqrt{s} = 320$ GeV. Blue (open) squares are 1994-7 e^+p data at $\sqrt{s} = 300$ GeV. Red (upper) solid line is the SM expectation for e^-p at $\sqrt{s} = 320$ GeV. Blue (lower) solid line is the SM expectation for e^+p at $\sqrt{s} = 300$ GeV, and blue (dashed) line is the expectation for e^+p at $\sqrt{s} = 320$ GeV. The luminosity uncertainty of 1.5% is not included in the errors shown.

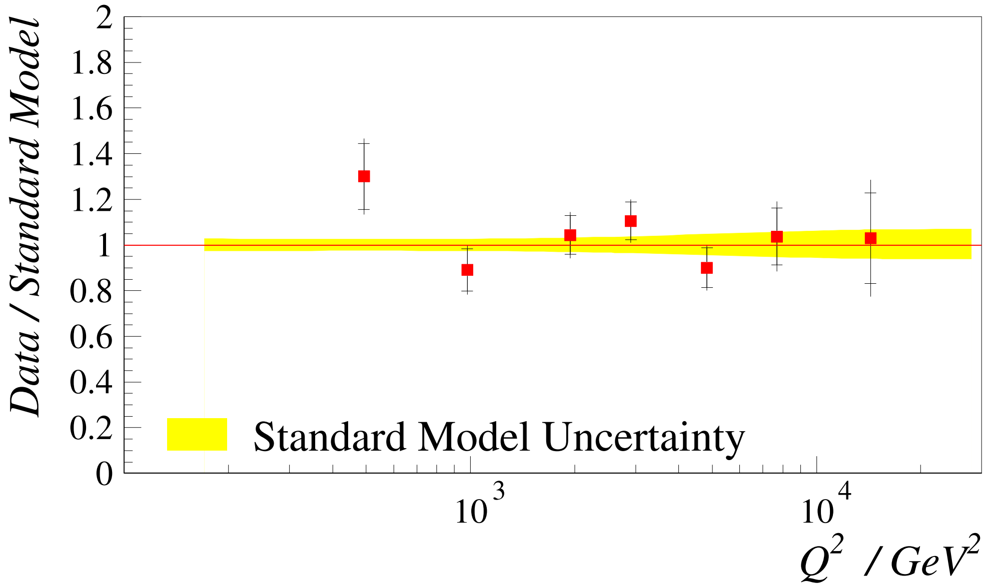

Figure 7.5: Data / Standard Model expectation as a function of Q^2 for 1998-9 e^-p at $\sqrt{s} = 320$ GeV. Yellow (shaded) band is the SM uncertainty. The luminosity uncertainty of 1.5% is not included in the errors shown.

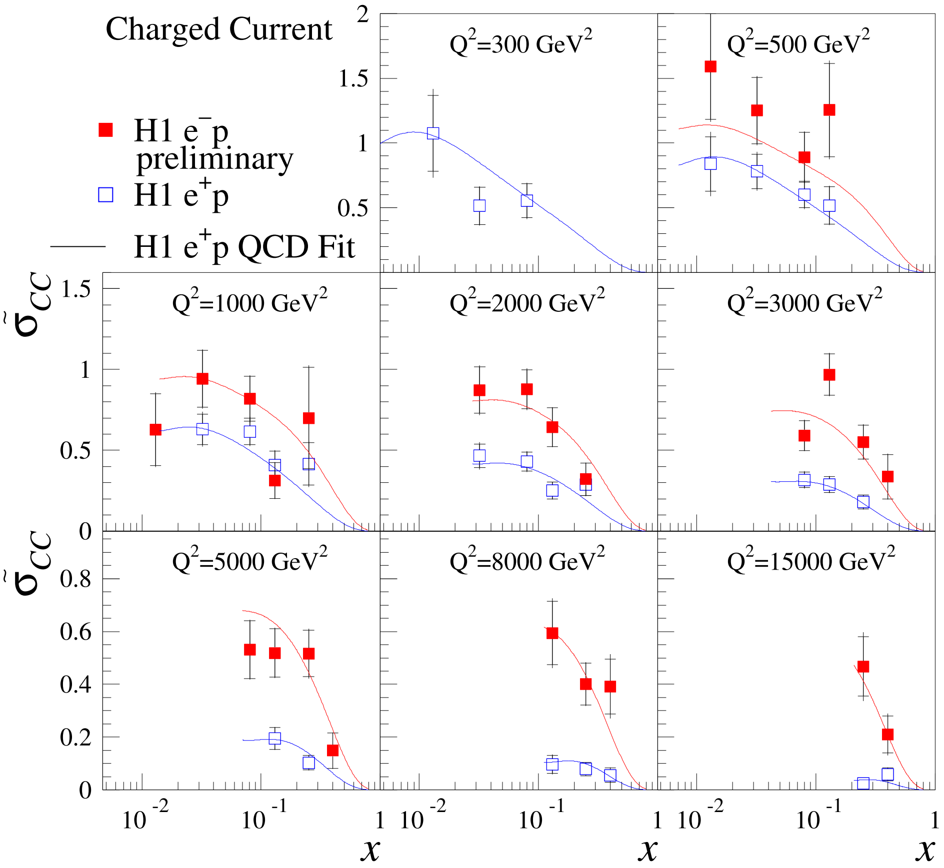

Figure 7.6: Double differential CC reduced cross section. Red (solid) squares are 1998-9 e^-p data at $\sqrt{s} = 320$ GeV. Blue (open) squares are 1994-7 e^+p data at $\sqrt{s} = 300$ GeV. Red (upper) solid line is the SM expectation for e^-p at $\sqrt{s} = 320$ GeV. Blue (lower) solid line is the SM expectation for e^+p at $\sqrt{s} = 300$ GeV. The luminosity uncertainty of 1.5% is not included in the errors shown.

Chapter 8

Radiative Charged Current Event Selection

The selection for the radiative CC analysis is very similar to the selection for the CC analysis. The same data samples and naming conventions are used as in the CC analysis, shown in table 6.1. It is necessary, however, to make some minor modifications to certain aspects of the analysis: the background finders, for example. In addition, a photon finder is included to identify isolated, high momentum photons. Aspects of this analysis which differ from the CC analysis are described below. All distributions shown contain data from sample B unless otherwise stated.

8.1 Phase Space

The phase space in which the radiative CC analysis is preformed is reduced slightly with respect to that of the CC analysis (fig 8.1). The cut on the missing transverse momentum is increased to:

$$p_t^{miss} \geq 25 \text{ GeV} \tag{8.1}$$

There is also a difference in the measurement of missing transverse momentum and transverse momentum of the hadronic final state

$$p_t^{miss} = |\overrightarrow{p_t^{had}} + \overrightarrow{p_t^{\gamma}}| \tag{8.2}$$

where p_t^{had} is the transverse momentum of the hadronic final state[1] and p_t^{γ} is the transverse momentum of the isolated photon.

---

[1] In a non-radiative CC event $p_t^{had} = p_t^{miss}$ and $p_t^{had} \equiv p_{t,h}$ in section 3.1.

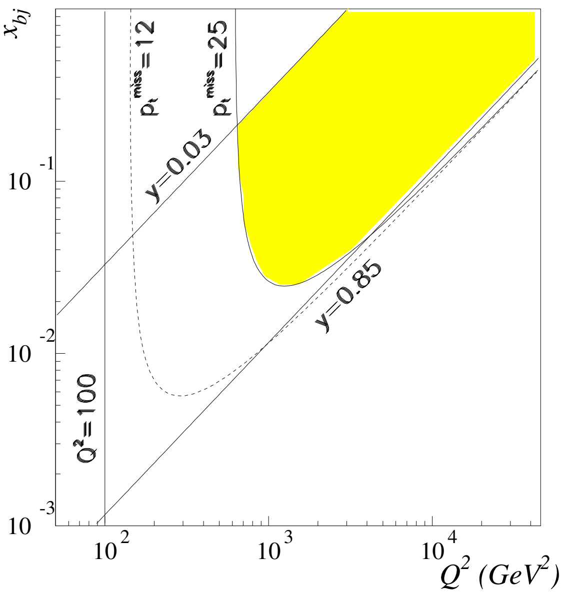

Figure 8.1: Kinematic plane available for CC analysis, marked by yellow (shaded) area. The p_t^{miss} cut for CC (dashed line) and radiative CC analysis are both shown.

8.2 Photon selection

The photon finder used to select photons within CC events is described in detail in chapter 5. The specific cuts applied to photons selected by the finder are as follows:

- transverse momentum of the photon $p_t^{\gamma} > 3$ GeV
- polar angle acceptance in the LAr calorimeter $25^o < \theta^{\gamma} < 145^o$
- isolation R between the photon (γ) and the nearest cluster (c) of $R_{\gamma-c} > 0.5$
- isolation R between the photon (γ) and the nearest track (t) of $R_{\gamma-t} > 0.5$
- isolation R between the photon (γ) and the nearest jet of $R_{\gamma-jet} > 0.5$

where isolation R is a cone in η,ϕ space:

$$R_{\gamma-c,t,jet} = \sqrt{(\eta_{\gamma} - \eta_{c,t,jet})^2 + (\phi_{\gamma} - \phi_{c,t,jet})^2}$$

and ϕ is the azimuthal angle and η is the pseudorapidity.

8.3 Non-ep background rejection

Event track requirement

Within this analysis, it has been found that a cut on the minimum p_t of the vertex fitted tracks in the event acts as a very effective rejection criterion for non-ep type background events. Frequently, these types of events will deposit large amounts of energy in the calorimeter, or pass through the detector and not leave tracks which point to the interaction region. Therefore the following requirement is made:

$$p_t^{tracks} > 0.5 \text{ GeV}. \tag{8.3}$$

Cosmic and halo muon rejection

A study of the cosmic and halo muon background finders has shown that the application of the full complement of finders used in the CC analysis would be inappropriate for the radiative CC analysis. Events from each of the background finders which makes rejections have been visually scanned to select which ones are appropriate for use in this analysis. Consequently, a modified selection of finders is applied, excluding any finder which rejects more 3% of the good radiative CC candidates in a sample. The global efficiency of the remaining finders at not misidentifying true CC events is shown in fig. 8.2. In all bins the efficiency is above 90%, despite the statistically small samples available for this study.

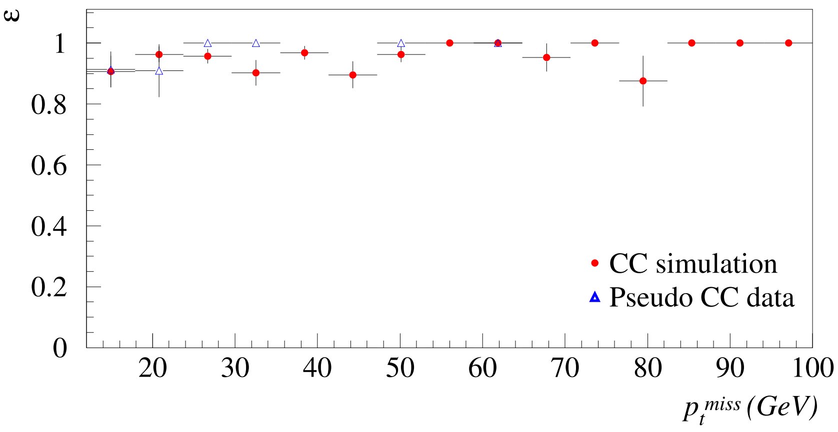

Figure 8.2: Efficiency of cosmic ray and halo muon background finders versus p_t^{miss} of the event, calculated with `DJANGO` simulation (red dots) and pseudo CC data (blue triangles).

8.4 Physics (ep) background rejection

The energy isotropy cut

The V_{ap}/V_p cut, described in section 6.5, is reduced for this selection. It is sensible to reduce the cut against such background contributions for two reasons:

- the contribution to the CC sample from photoproduction and NC has been shown to be very small above $p_t^{miss} = 25$ GeV in figure 6.6(b).
- leaving this cut at the threshold applied for the CC analysis also results in the loss of signal events in the radiative CC analysis.

This second reason is due to the fact that a high momentum photon, separated from the current jet, will alter the energy distribution in the detector from that of an ordinary CC event (see fig. 8.3). The energy of the photon is still likely to be only a fraction of the energy carried by the jet, but if the photon falls in the opposite hemisphere to the jet then the CC V_{ap}/V_p cut may reject the event. Therefore, this cut is reduced to:

$$V_{ap}/V_p < 0.3 \tag{8.4}$$

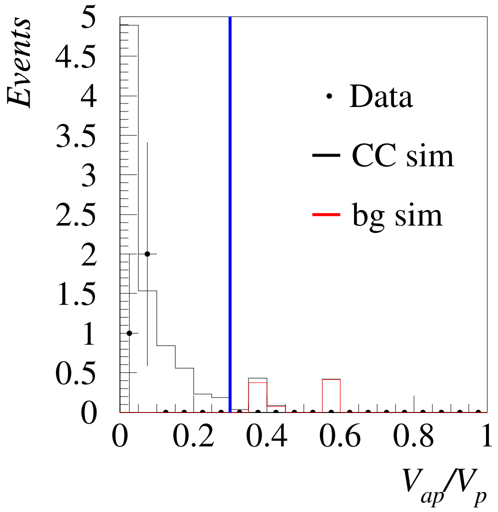

Figure 8.3: Distribution of V_{ap}/V_p for $p_t^{miss} > 25$ GeV. The black dots are data, the black line `DJANGO` CC MC and the red (light) line is the combined `DJANGO` NC and `PYTHIA` γp simulation. The blue vertical line represents the cut placed on V_{ap}/V_p for the radiative CC analysis.

8.5 Trigger

Identical triggers are used for the CC and radiative CC analyses. The efficiency studies are repeated using pseudo CC data with full radiative CC cuts applied, shown in fig. 8.4. The efficiencies are found to be the same within errors as obtained in the CC case.

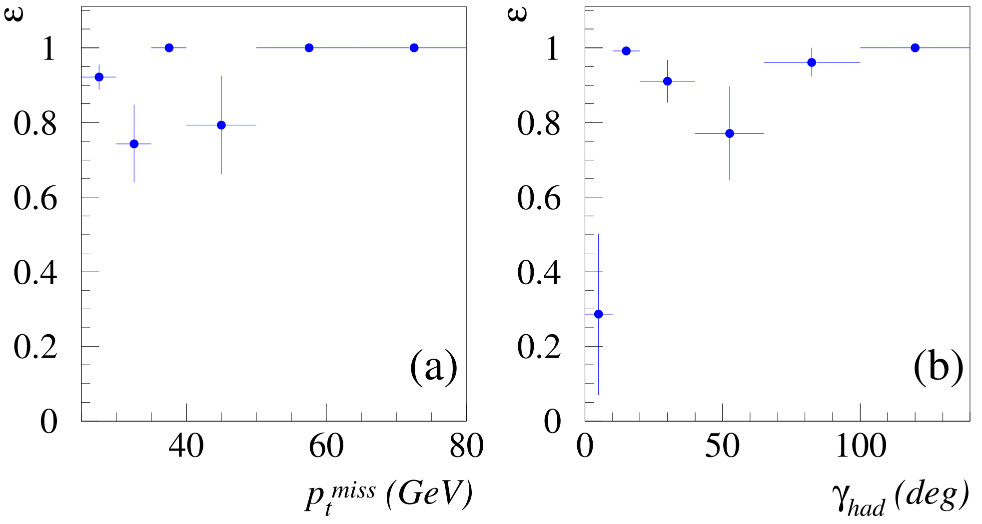

Figure 8.4: Trigger efficiencies for radiative CC, calculated using pseudo CC data, in terms of (a) p_t^{miss} of the event, and (b) angle of the hadronic final state γ_{had}.

8.6 Visual scan

A visual scan of all 24 selected events from all data samples, results in the removal of 2 background events.

8.7 Final sample

The following section contains the monitor distributions for all three data samples, and all events which enter into the final analysis measurements.

Sample A

The control distributions shown in figs 8.5 and 8.6 pertain to the first data sample and correspond to a luminosity of 35.7 pb^{-1} taken between 1994 and 1997 with positron and proton beams at $\sqrt{s} = 300$ GeV. The plots shown in fig. 8.5 relate to overall properties of the events: (a) the missing transverse momentum p_t^{miss}, (b) the transverse momentum of the hadronic final state p_t^{had}, (c) the $\log Q^2$ distribution, (d) the inelasticity y, (e) the angle of the hadronic final state γ^{had} and (f) the azimuthal distribution ϕ. The plots shown in fig. 8.6 relate to properties of the photons within the events: (a) the transverse momenutum of the photon p_t^{γ}, (b) the polar angle distribution θ^{γ}, (c) the azimuthal angle distribution ϕ^{γ}, (d) the photon - nearest cluster separation $R_{\gamma-c}$, (e) the photon - nearest track separation $R_{\gamma-t}$ and (f) the photon - nearest jet separation $R_{\gamma-jet}$.

The figures show that the data lie slightly below the `DJANGO` MC prediction, although the distributions are otherwise well described.

Sample B

The control distributions shown in figs 8.7 and 8.8 pertain to the second data sample and correspond to 16.4 pb^{-1} taken in 1998 and 1999 with electron and proton beams at $\sqrt{s} = 320$ GeV. The distributions (described analogously to distributions of sample **A**) show that the data yield falls below that predicted by the `DJANGO` simulation.

Sample C

The control distributions shown in figs 8.9 and 8.10 pertain to the final data sample and correspond to 62.9 pb^{-1} taken in 1999 and 2000 with positron and proton beams at $\sqrt{s} = 320$ GeV. The distributions (described analogously to distributions of sample **A**) show a trend towards the data yield being greater than the `DJANGO` MC prediction. The overall shape of the distributions, however, is quite accurate.

Combined sample

Figures 8.11 and 8.12 contain the combined data from samples **A**, **B** and **C**. The agreement between data and SM `DJANGO` MC prediction is excellent within the statistical errors shown for all distributions. Two events from the final sample of 22 are shown in figs. 8.13 and 8.14. Details of all events can be found in Appendix A.

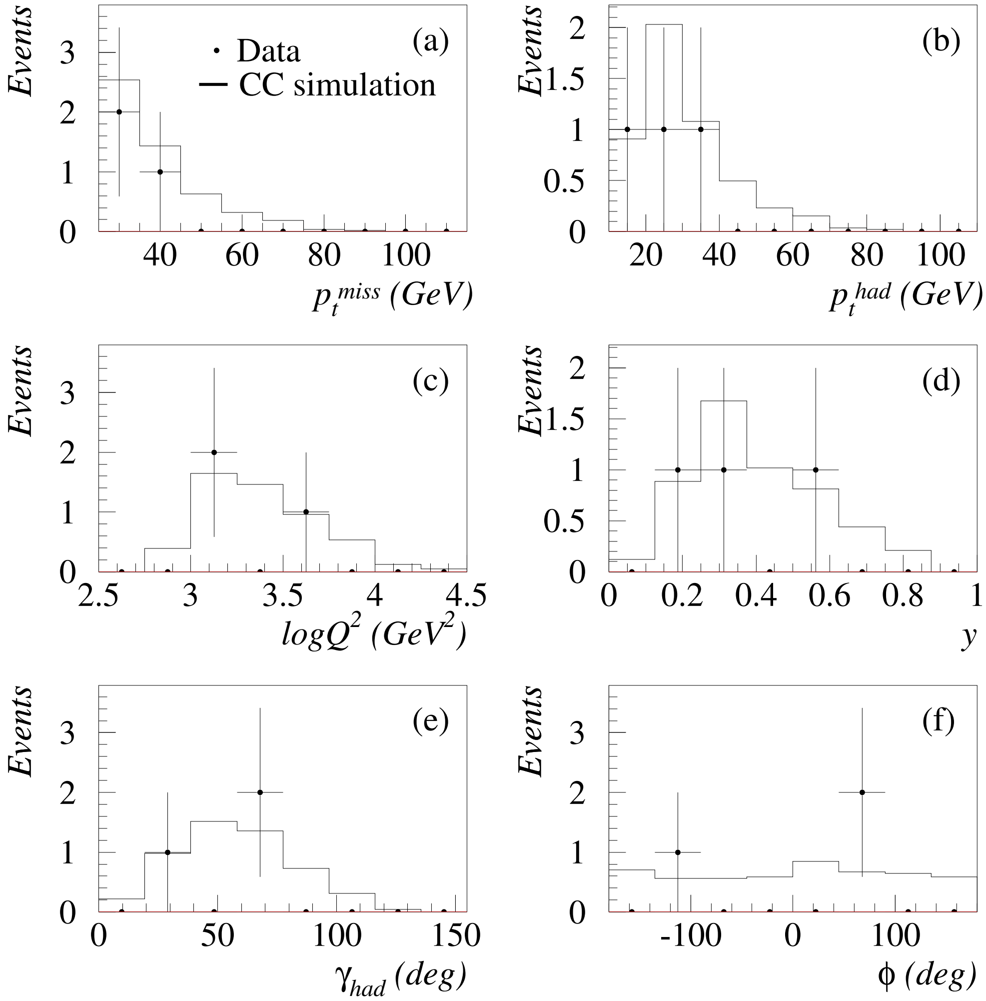

Figure 8.5: Data sample **A**. Black points are data, black line is `DJANGO` CC MC simulation. Plot (a) shows the missing transverse momentum p_t^{miss} distribution, plot (b) the transverse momentum of the hadrons p_t^{had}, plot (c) the four momementum transfer Q^2, plot (d) the inelasticity y, plot (e) the angle of the hadronic final state γ and plot (f) the azimuthal angle ϕ. The red line at the bottom of each plot indicates that within the quoted precision, no background from NC and γp contribute.

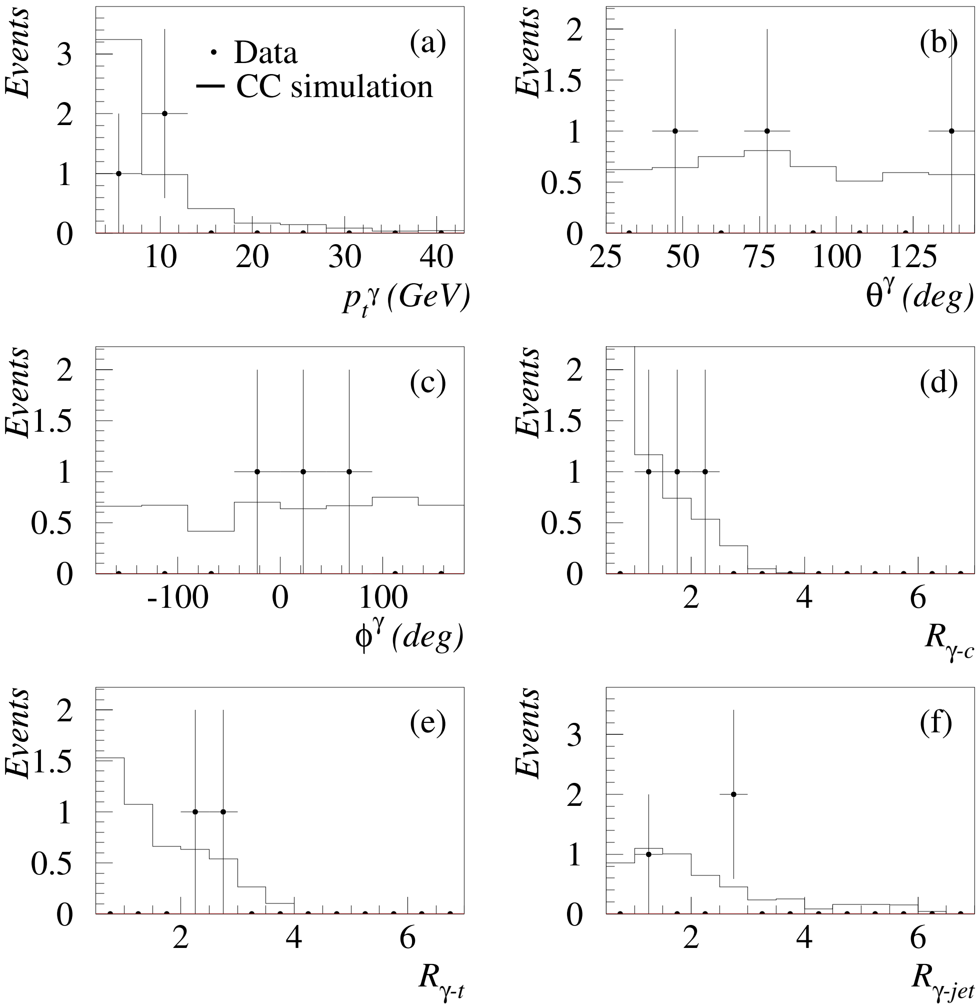

Figure 8.6: Data sample **A**. Black points are data, black line is `DJANGO` CC MC simulation. Plot (a) shows the distribution of the transverse momentum of the photon p_t^γ plot (b) shows the polar angle distribution of the photon θ^γ, plot (c) the azimuthal angle of the photon ϕ^γ, plot (d) the photon - nearest cluster isolation $R_{\gamma-c}$, plot (e) the photon - nearest track isolation $R_{\gamma-t}$ and plot (f) the photon - nearest jet isolation $R_{\gamma-jet}$. The red line at the bottom of each plot indicates that within the quoted precision, no backgound from NC and γp contribute.

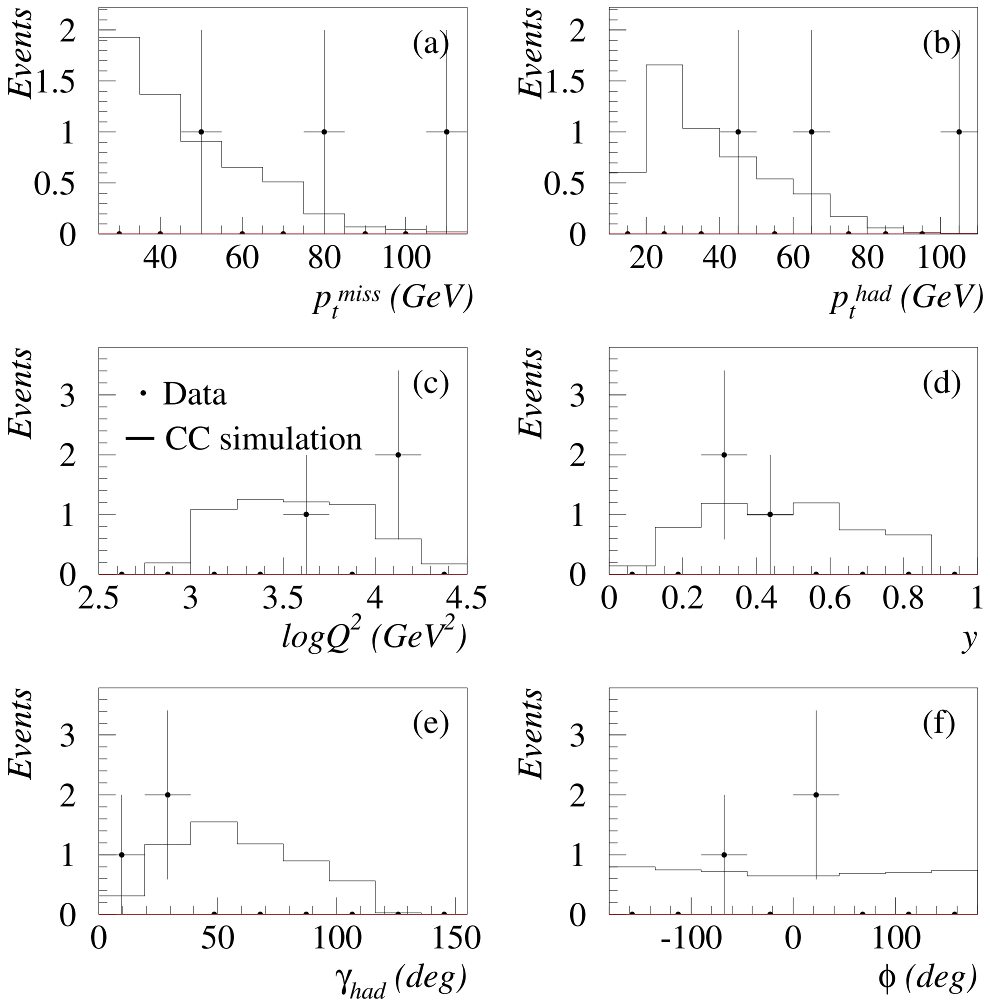

Figure 8.7: Data sample **B**. Black points are data, black line is `DJANGO` CC MC simulation. Plot (a) shows the missing transverse momentum p_t^{miss} distribution, plot (b) the transverse momentum of the hadrons p_t^{had}, plot (c) the four momementum transfer Q^2, plot (d) the inelasticity y, plot (e) the angle of the hadronic final state γ and plot (f) the azimuthal angle ϕ. The red line at the bottom of each plot indicates that within the quoted precision, no background from NC and γp contribute.

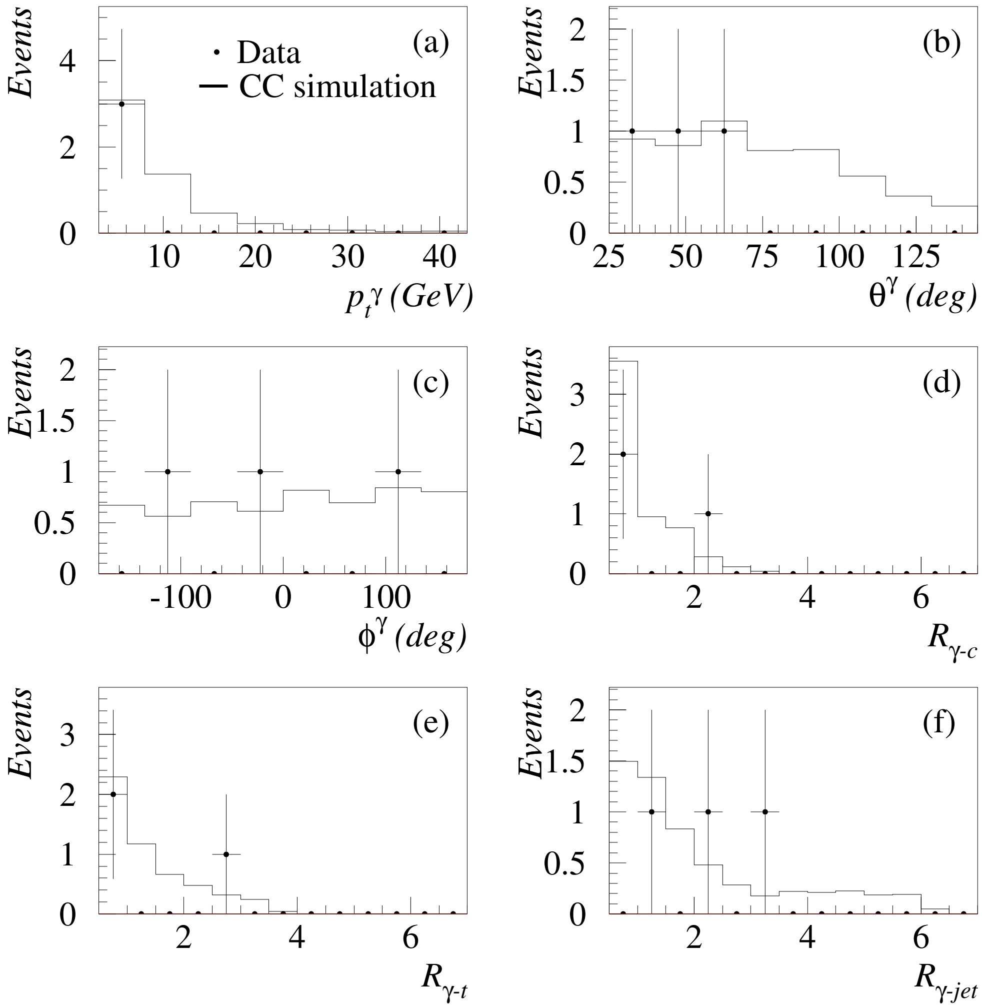

Figure 8.8: Data sample **B**. Black points are data, black line is `DJANGO` CC MC simulation. Plot (a) shows the distribution of the transverse momentum of the photon p_t^γ plot (b) shows the polar angle distribution of the photon θ^γ, plot (c) the azimuthal angle of the photon ϕ^γ, plot (d) the photon - nearest cluster isolation $R_{\gamma-c}$, plot (e) the photon - nearest track isolation $R_{\gamma-t}$ and plot (f) the photon - nearest jet isolation $R_{\gamma-jet}$. The red line at the bottom of each plot indicates that within the quoted precision, no backgound from NC and γp contribute.

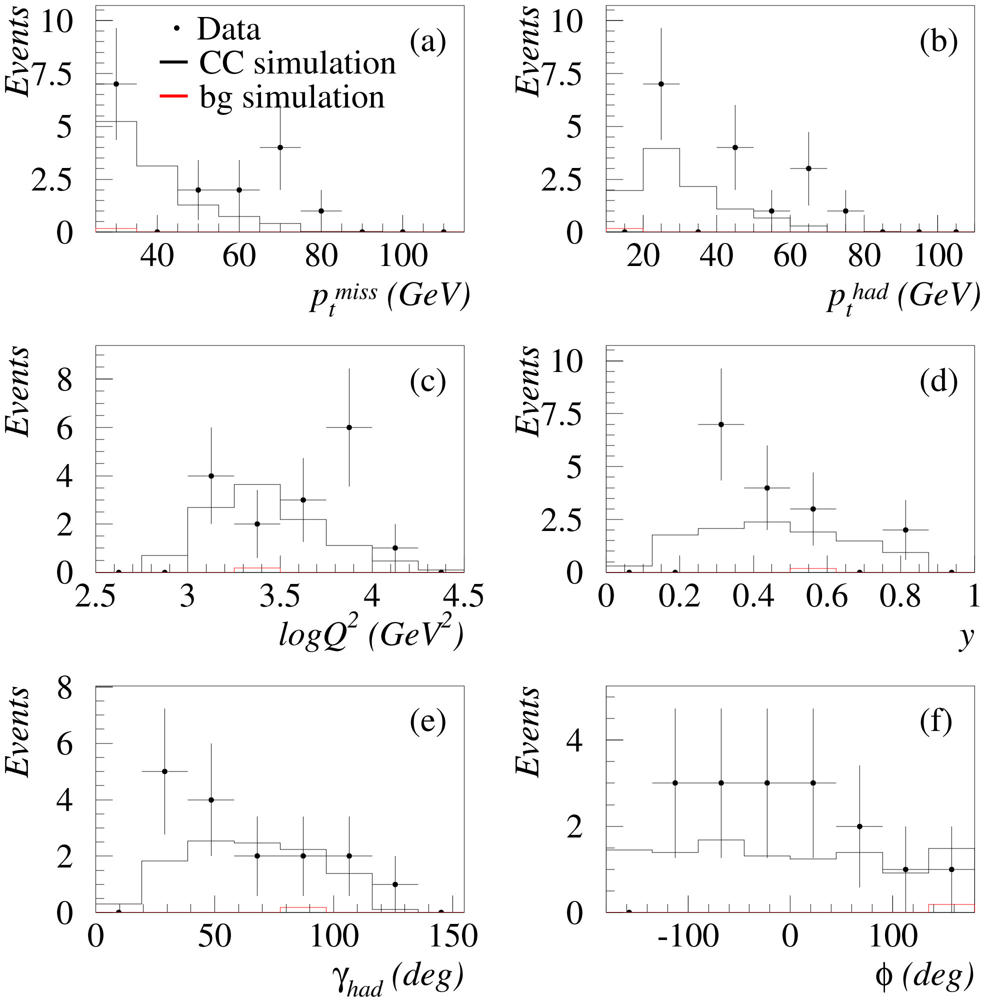

Figure 8.9: Data sample **C**. Black points are data, black line is the `DJANGO` CC MC simulation and red (light) line is the contribution from `PYTHIA` photoproduction and `DJANGO` NC MCs. Plot (a) shows the missing transverse momentum p_t^{miss} distribution, plot (b) the transverse momentum of the hadrons p_t^{had}, plot (c) the four momementum transfer Q^2, plot (d) the inelasticity y, plot (e) the angle of the hadronic final state γ and plot (f) the azimuthal angle ϕ. The red line at the bottom of each plot indicates that a very small contribution from NC and γp is seen.

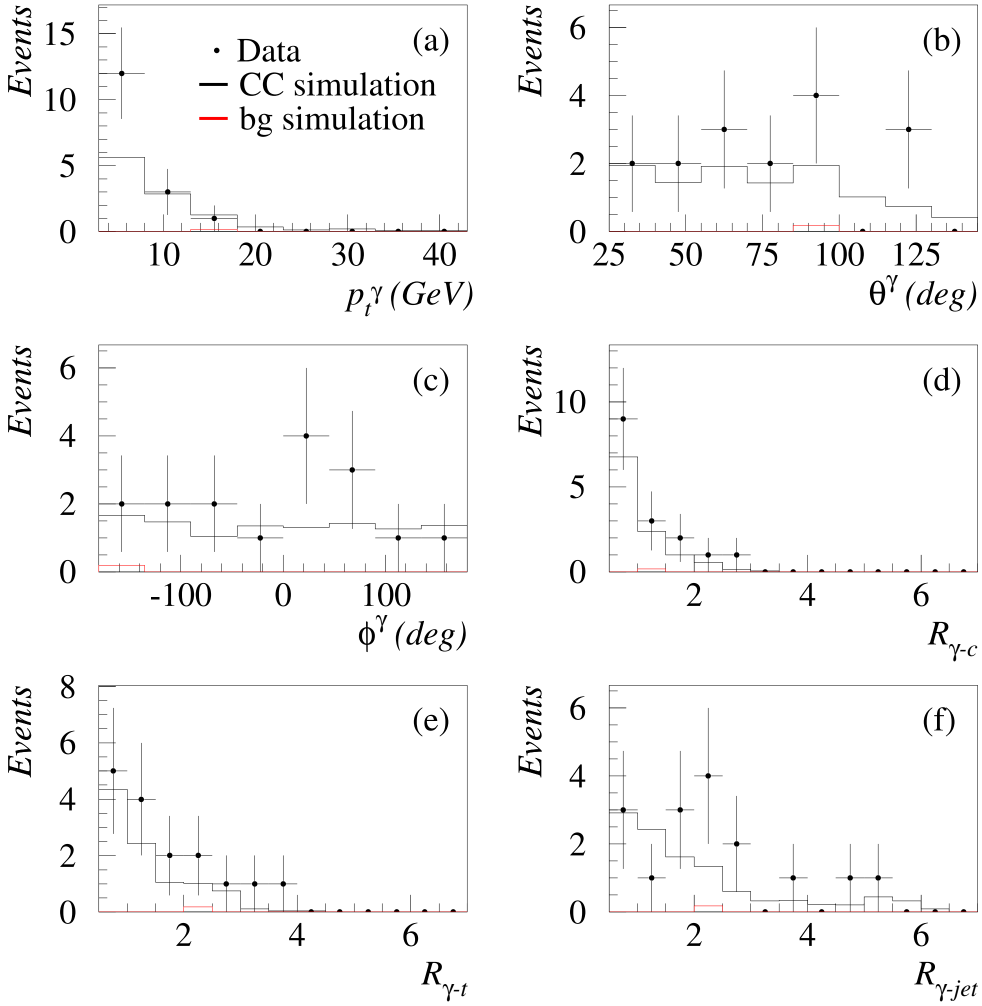

Figure 8.10: Data sample **C**. Black points are data, black line is the `DJANGO` CC MC simulation and red (light) line is the contribution from `PYTHIA` photoproduction and `DJANGO` NC MCs. Plot (a) shows the distribution of the transverse momentum of the photon p_t^γ plot (b) shows the polar angle distribution of the photon θ^γ, plot (c) the azimuthal angle of the photon ϕ^γ, plot (d) the photon - nearest cluster isolation $R_{\gamma-c}$, plot (e) the photon - nearest track isolation $R_{\gamma-t}$ and plot (f) the photon - nearest jet isolation $R_{\gamma-jet}$. The red line at the bottom of each plot indicates that a very small contribution from NC and γp is seen.

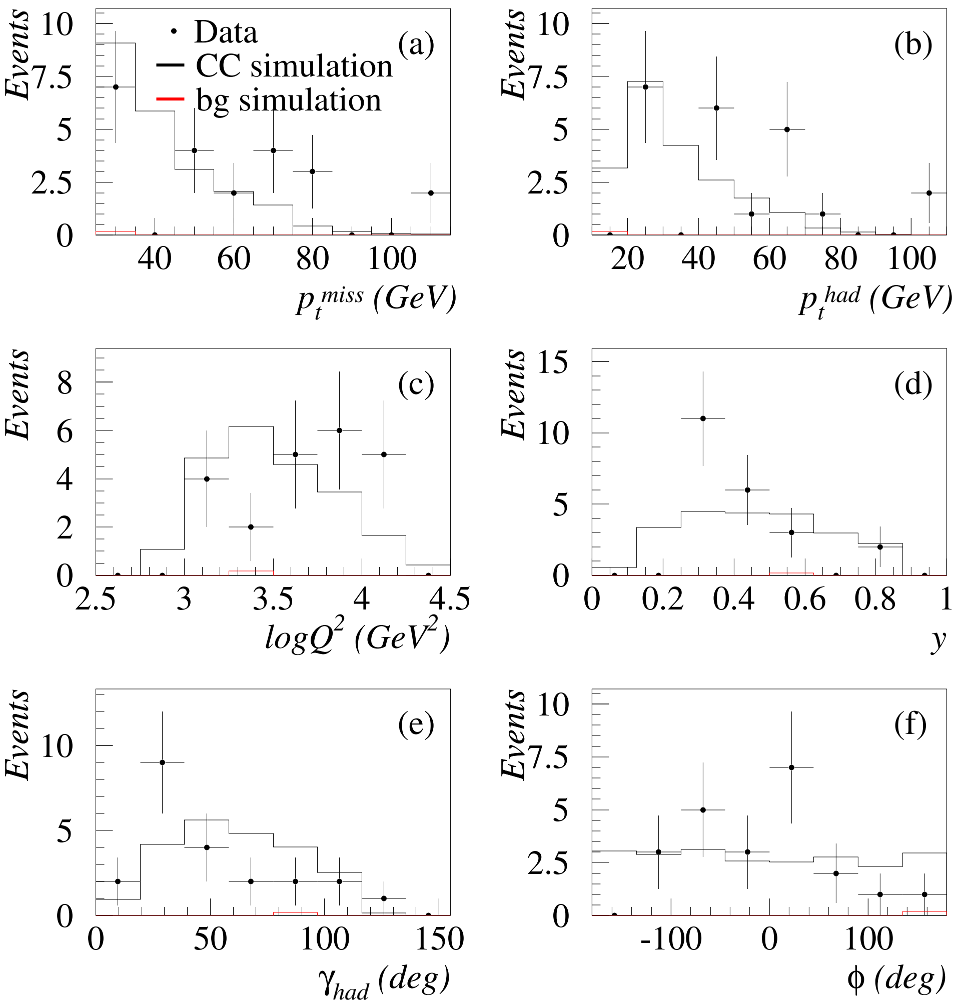

Figure 8.11: Combined data sets. Black points are data, black line is the `DJANGO` CC MC simulation and red (light) line is the contribution from `PYTHIA` photoproduction and `DJANGO` NC MCs. Plot (a) shows the missing transverse momentum p_t^{miss} distribution, plot (b) the transverse momentum of the hadrons p_t^{had}, plot (c) the four momementum transfer Q^2, plot (d) the inelasticity y, plot (e) the angle of the hadronic final state γ and plot (f) the azimuthal angle ϕ. The red line at the bottom of each plot indicates that a very small contribution from NC and γp is seen.

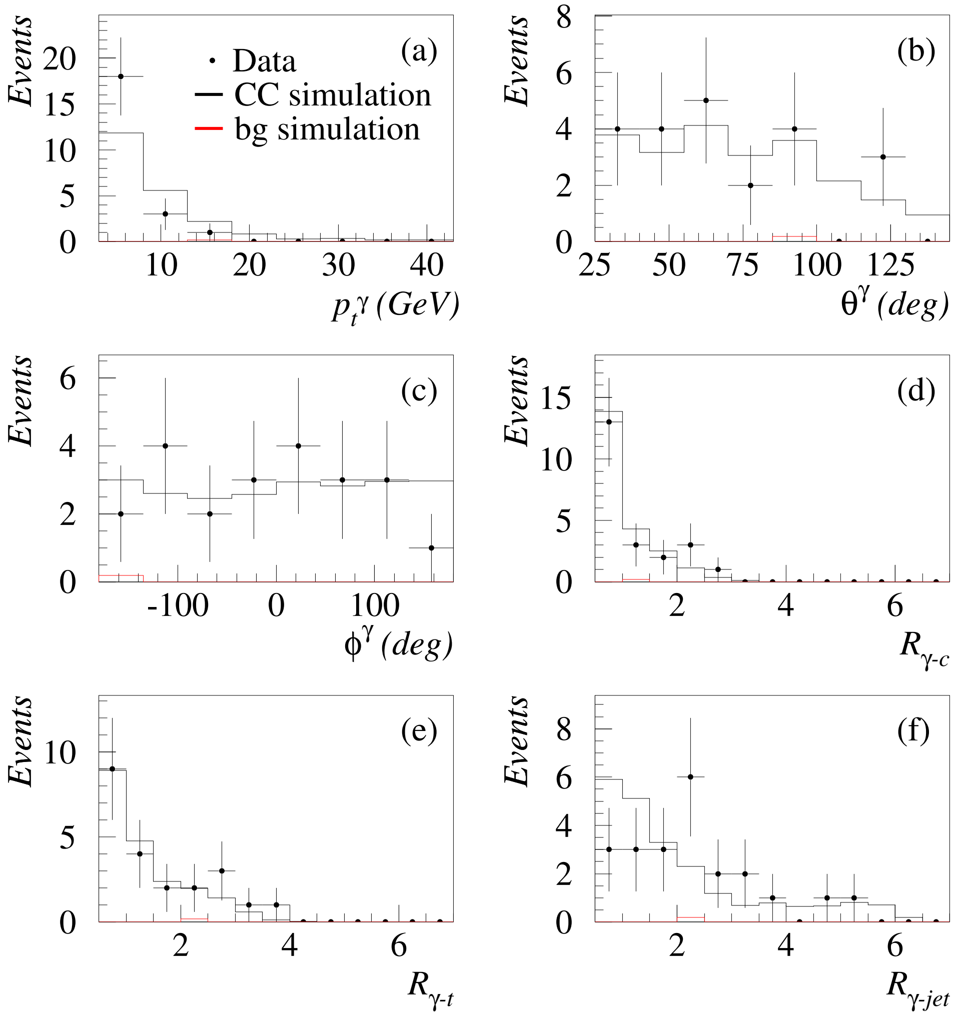

Figure 8.12: Combined data sets. Black points are data, black line is the `DJANGO` CC MC simulation and red (light) line is the contribution from `PYTHIA` photoproduction and `DJANGO` NC MCs. Plot (a) shows the distribution of the transverse momentum of the photon p_t^γ plot (b) shows the polar angle distribution of the photon θ^γ, plot (c) the azimuthal angle of the photon ϕ^γ, plot (d) the photon - nearest cluster isolation $R_{\gamma-c}$, plot (e) the photon - nearest track isolation $R_{\gamma-t}$ and plot (f) the photon - nearest jet isolation $R_{\gamma-jet}$. The red line at the bottom of each plot indicates that a very small contribution from NC and γp is seen.

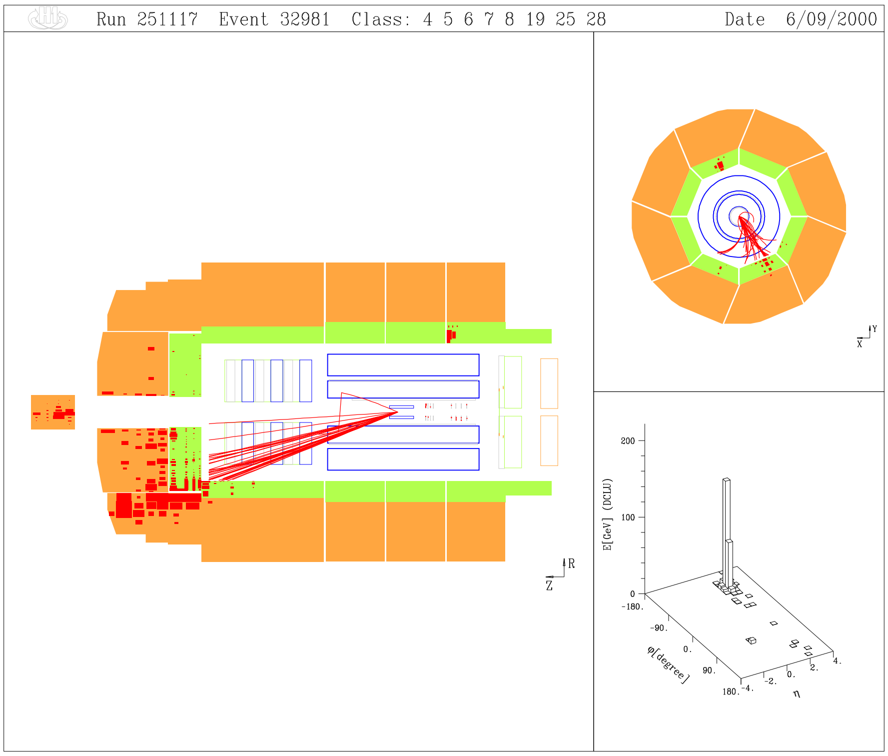

Figure 8.13: An example of a very clean radiative CC event. The large picture is a view of the cross section of the detector, the upper small picture is a cross section in the $x - y$ plane and the lower small picture shows the energy depositions in the $\eta - \phi$ plane.

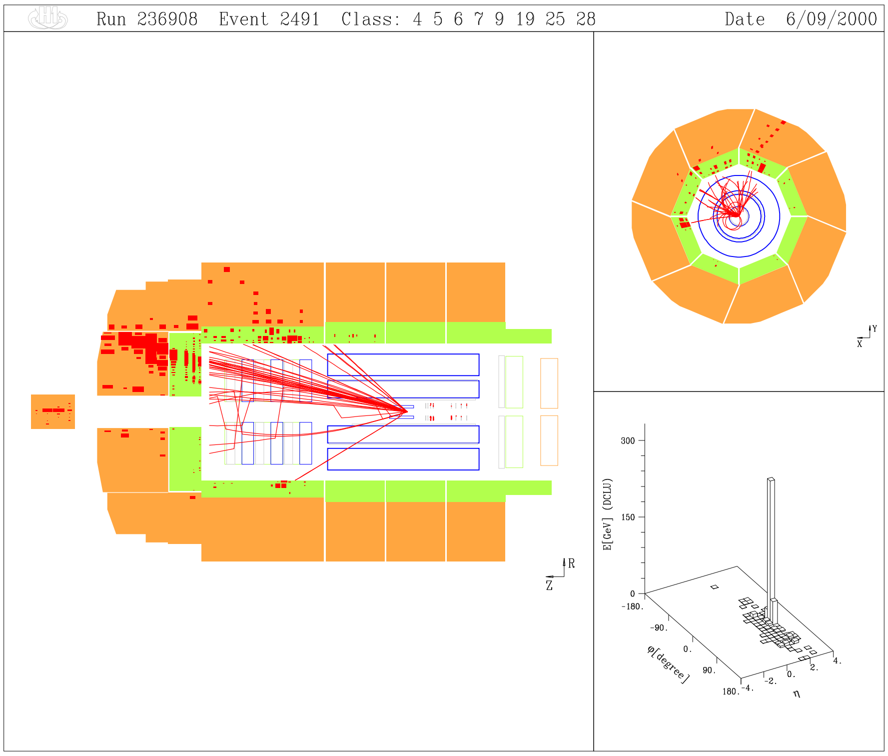

Figure 8.14: An example of a photon conversion event. The photon conversion can be seen as the energy cluster with associated track in the lower half of the large picture.

Chapter 9

Results of Radiative Charged Current Analysis

The measurements presented in this chapter are the results of the inclusive radiative CC analysis - events with missing transverse momentum and a high momentum isolated photon. It is important to emphasize that it is only for convenience that this analysis is referred to as the radiative CC analysis and that potentially there are other, more exotic, processes which could contribute to the event sample.

The inclusive measurement of each data sample is presented in several forms: as a cross section and as a function of different properties of the events. There is then a comparison of the measurements with SM MC prediction and with the generator level `WWGAMMA` MC. This latter allows variation of the tri-linear gauge couplings which govern the WWγ vertex within a radiative CC event, expressed in terms of the anomalous couplings $\Delta\kappa$ and λ. Finally there is a discussion about the compatability of the results with the Standard Model predictions for these anomalous couplings.

9.1 Cross section measurement procedure

9.1.1 Binning

There is no specific binning for the radiative CC analysis due to the limited statistical accuracy of the data samples. All measurements are made globally.

However, in order to show the accuracy of the event selection, plots are shown of the purity, stability and acceptance (as defined in section 7.1.1) in bins. The calculations for each data sample are made as a function of the the transverse momentum of the photon p_t^γ in figs. 9.1(a),(c) and (e), and the polar angle of the photon θ^γ in figs. 9.1(b),(d) and (f). The purity for all samples is between approximately 50% and 80%, the stability also ranges from 50% to 80% and the acceptance between 80% and 130%. The plots for the different data samples show very similar systematic behaviour.

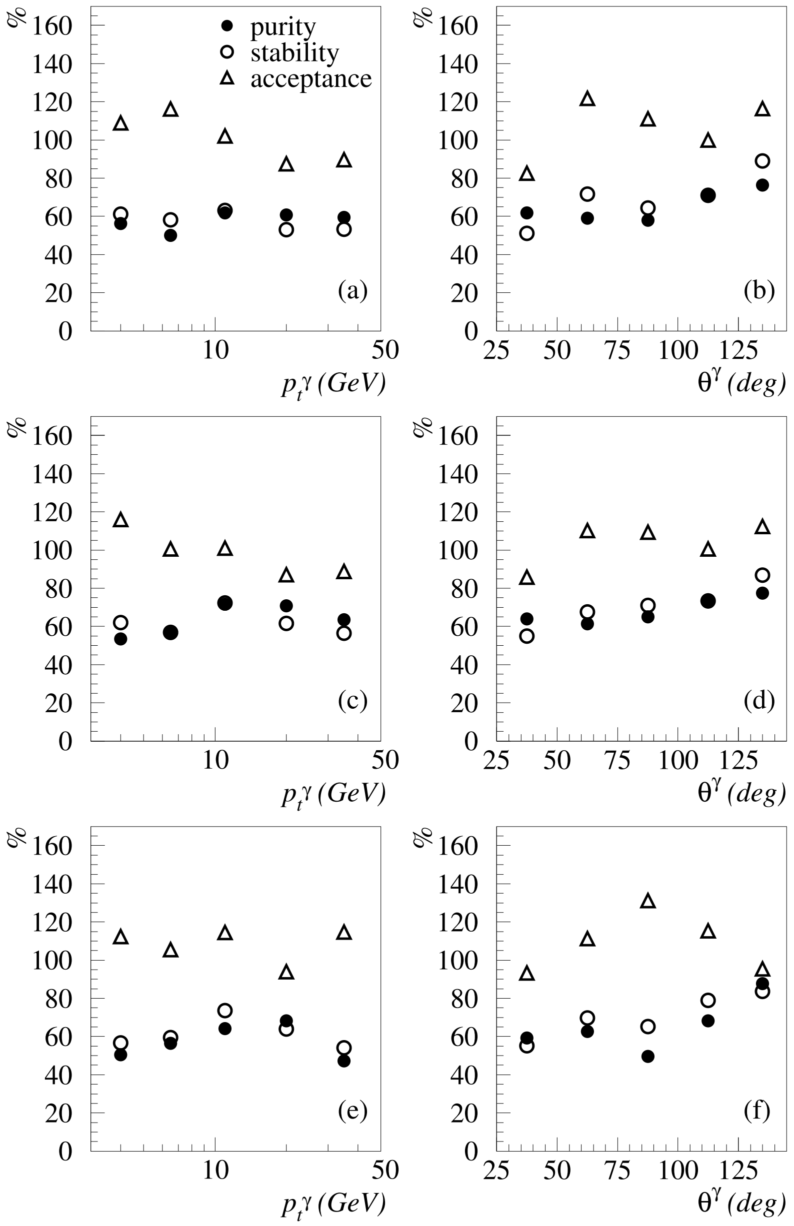

Figure 9.1: Purity, stability and acceptance for the radiative CC candidate sample calculated using `DJANGO` CC MC.

9.1.2 Analysis cross check

The radiative CC cross section results have been verified using an H1 standard electron finder [46] to replace the photon finder. The features of the electron finder with the energy cluster and track information separated are similar to those of the photon finder. This allows a similar photon candidate selection to be made; identical isolation requirements and electromagnetic energy fraction cut are applied. However, the minimum p_t^γ cut on the electron finder is set to 5 GeV, so comparisons cannot be made for the two finders below this threshold. Fig. 9.2 shows plots of the purity, stability and acceptance of the radiative CC sample using the electron finder: fig. 9.2(a) should be compared to fig. 9.1(c) and 9.2(b) to 9.1(d).

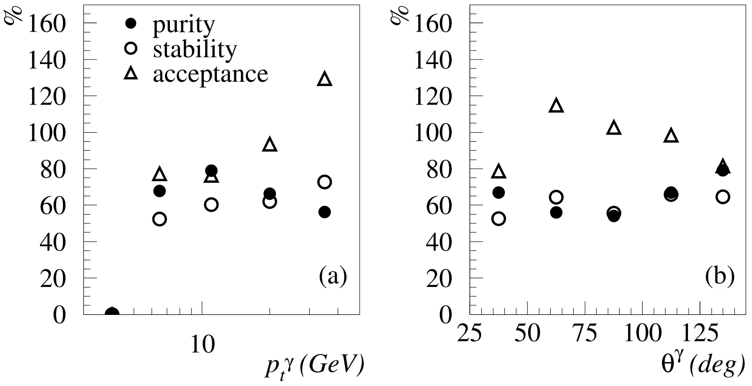

Figure 9.2: Purity, stability and acceptance for the radiative CC candidate sample using the electron finder, calculated with `DJANGO` CC MC.

Comparison of the above plots with those made using the photon finder shows that, although the shapes of the distributions differ slightly, the calculated values of the purity and stability are very similar, to within ~10%. Differences in the shape of these distributions occur due to differences in resolution of the finders and hence, smearing effects with respect to the isolation determination. The final selection of events using the electron finder or the photon finder yields exactly the same events in the data sample used for the cross check.

9.1.3 Systematic uncertainties

Systematic uncertainties, identical to those described in 7.1.3, are assigned to the radiative CC analysis with the addition of an uncertainty of 10% on the photon finder inefficiency, described in sections 5.3 and 9.1.2.

9.1.4 Calculation of the cross section

The calculation of the cross section is similar to that shown in section 7.1.4 although, since the measurements are not made as a function of any particular kinematic variable, there is no need to include the terms for bin centre corrections.

The equation used is as follows:

$$\sigma = \frac{N^{data} - N^{bg}}{N^{MC}_{rec}} . \frac{\mathcal{L}^{MC}}{\mathcal{L}} . \sigma^{MC} \tag{9.1}$$

where

N^{data} is the number of events,
N^{bg} is the number of background events,
N^{MC}_{rec} is the number of reconstructed events,
$\mathcal{L}^{MC}$ is the luminosity of the MC simulation file,
$\mathcal{L}$ is the total integrated luminosity of the data sample and
σ^{MC} is the cross section from the MC alone, using $\sigma^{MC} = \frac{N_{gen}}{\mathcal{L}^{MC}}$.

9.2 Results

A selection procedure has been designed for events with missing transverse momentum and an isolated, high momentum photon. Such events are observed and, in order to draw conclusions about how data yields compare to SM predictions, it is useful to convert the observations into a cross section measurement.

The results of the inclusive analysis of radiative CC type events are presented in table 9.2. The numbers of events found for each data set are shown, compared to those expected from the SM predictions made by `DJANGO` CC MC and expected background contributions from photoproduction and NC. Table 9.1 gives the cross section measurements themselves, accompanied by the associated statistical and systematic errors. All event yields are consistent with the SM within given errors. The background contribution in sample **C** is due entirely to NC events.

The plots shown in fig. 9.3 illustrate the properties of the radiative CC events (a) as a function of the missing transverse momentum p_t^{miss} versus the photon momentum p_t^{γ} and (b) as a function of Q^2 of the events versus p_t^{γ}. The majority of the events have low p_t^{γ} but there is a reasonably even distribution of events over the p_t^{miss} and Q^2 ranges.

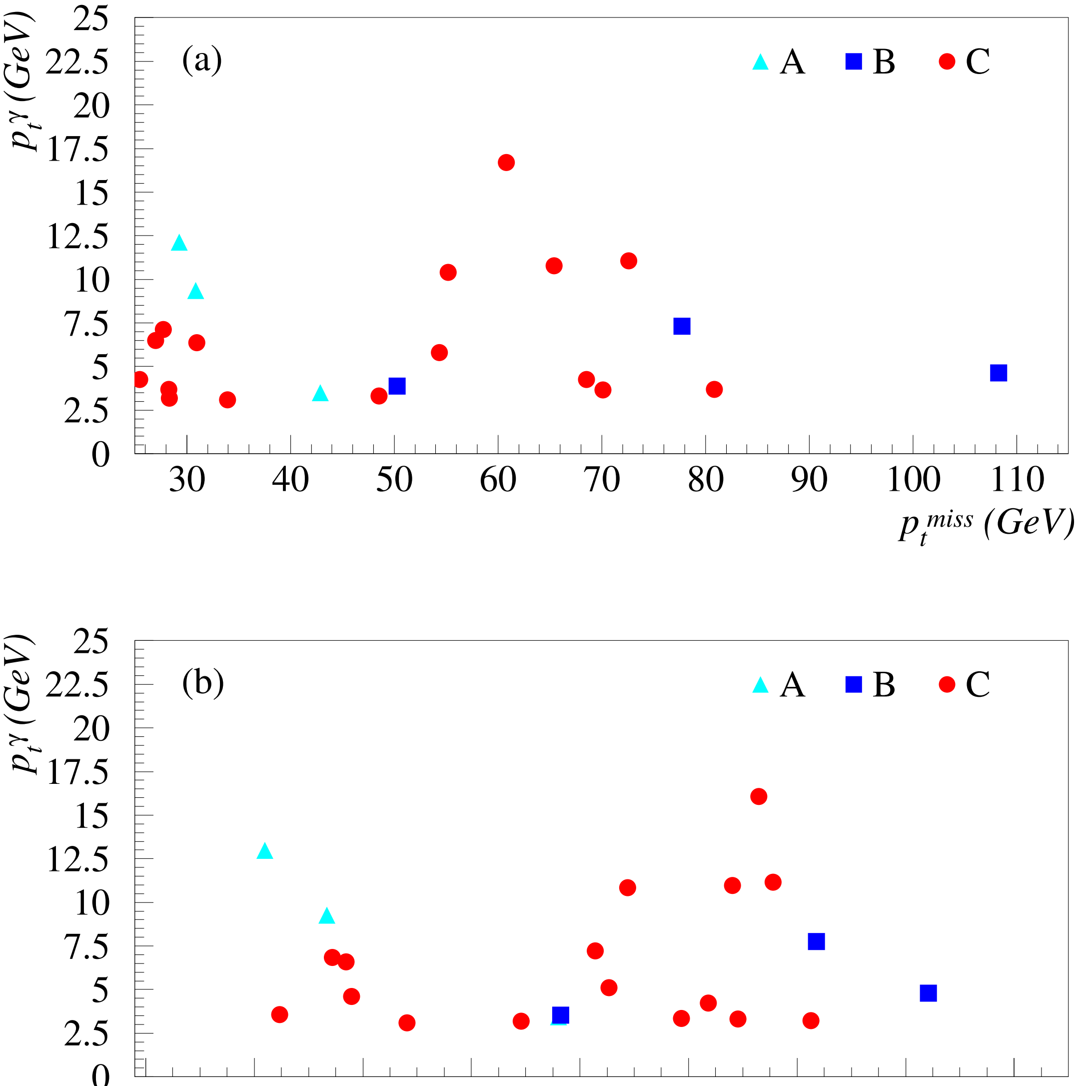

Figure 9.3: Plots showing (a) the transverse momentum p_t^γ of the photon versus the transverse momentum p_t of the event and (b) the transverse momentum p_t^γ of the photon versus the Q^2 for data sample **A** (light blue triangles), **B** (blue squares) and **C** (red circles).

Data Set	N^{data}	N^{MC}	N^{bg}
A	3	5.16 ± 0.07	-
B	3	6.44 ± 0.07	-
C	16	10.48 ± 0.26	0.18 ± 0.03

Table 9.1: Numbers of data events found (N^{data}) and those expected from the SM prediction (N^{MC}) and the contribution from background (N^{bg}) for data sets **A** (1994-7 e^+p at $\sqrt{s} = 300$ GeV), **B** (1998-9 e^-p at $\sqrt{s} = 320$ GeV) and **C** (1999-2000 e^+p at $\sqrt{s} = 320$ GeV).

Data Set	**Cross section** σ	$\delta\sigma$(stat.)	$\delta\sigma$(sys.) (pb)
A	0.130	± 0.077	± 0.040
B	0.321	± 0.185	± 0.097
C	0.378	± 0.091	± 0.115

Table 9.2: The cross section results for each data set and the associated statistical and systematic errors.

9.3 Comparisons with Monte Carlo

Having established the number of data events found and the values of the cross sections for each data set, it is useful to compare the results of the measurements to the expectation from the available SM predictions made by the `DJANGO` and `WWGAMMA` MCs.

`WWGAMMA` is a very basic generator MC: it does not provide sufficient output parameters to allow the simulation of real events. The output is limited to 4 vectors of the final state quark, photon, neutrino and proton remnant. In contrast, at the generator level `DJANGO` provides information about a stable final state which can be simulated with all H1 detector conditions applied. In essence, `WWGAMMA` is a tool which enables a calculation of the radiative CC cross section to be made for a given input (beam energies, incoming lepton type) within certain phase space constraints.

The cross section comparisons for the data, `DJANGO` and `WWGAMMA` are shown in table 9.3. The effective luminosity of the `WWGAMMA` file is two orders of magnitude larger than that of the `DJANGO` file, hence the statistical errors on the `WWGAMMA` results are much smaller. In general, there is good agreement between the predictions of the two MCs and within the quoted errors, all results for the data, `DJANGO` and `WWGAMMA` are consistent with each other.

Data Set	**Cross section** (pb)	`DJANGO` (pb)	`WWGAMMA` (pb)
A	$0.130 \pm 0.077 \pm 0.040$	0.229 ± 0.071	0.160 ± 0.001
B	$0.321 \pm 0.185 \pm 0.097$	0.688 ± 0.187	0.618 ± 0.002
C	$0.378 \pm 0.091 \pm 0.115$	0.250 ± 0.055	0.236 ± 0.001

Table 9.3: Cross section comparisons of the data and the predictions from the `DJANGO` MC and the `WWGAMMA` MC.

The two MCs are compared to each other in fig 9.4. Both are reconstructed using the beam energies and charges from data set **C** and normalised to the luminosity of this data sample. It is shown that there is very good agreement between the two in terms of expected numbers of events, and hence, cross section predictions. In general, with the exception of plots 9.4(a) and (d), their overall shape also agrees. The differences in plots (a) and (d) may be due to constraints on the reconstruction available, as described above. However, it is more likely that the shape incongruities are due to the differences in the treatment of the WWγ vertex itself. `WWGAMMA` contains a more comprehensive description of the matrix elements involved and is expected to be slightly different to `DJANGO`.

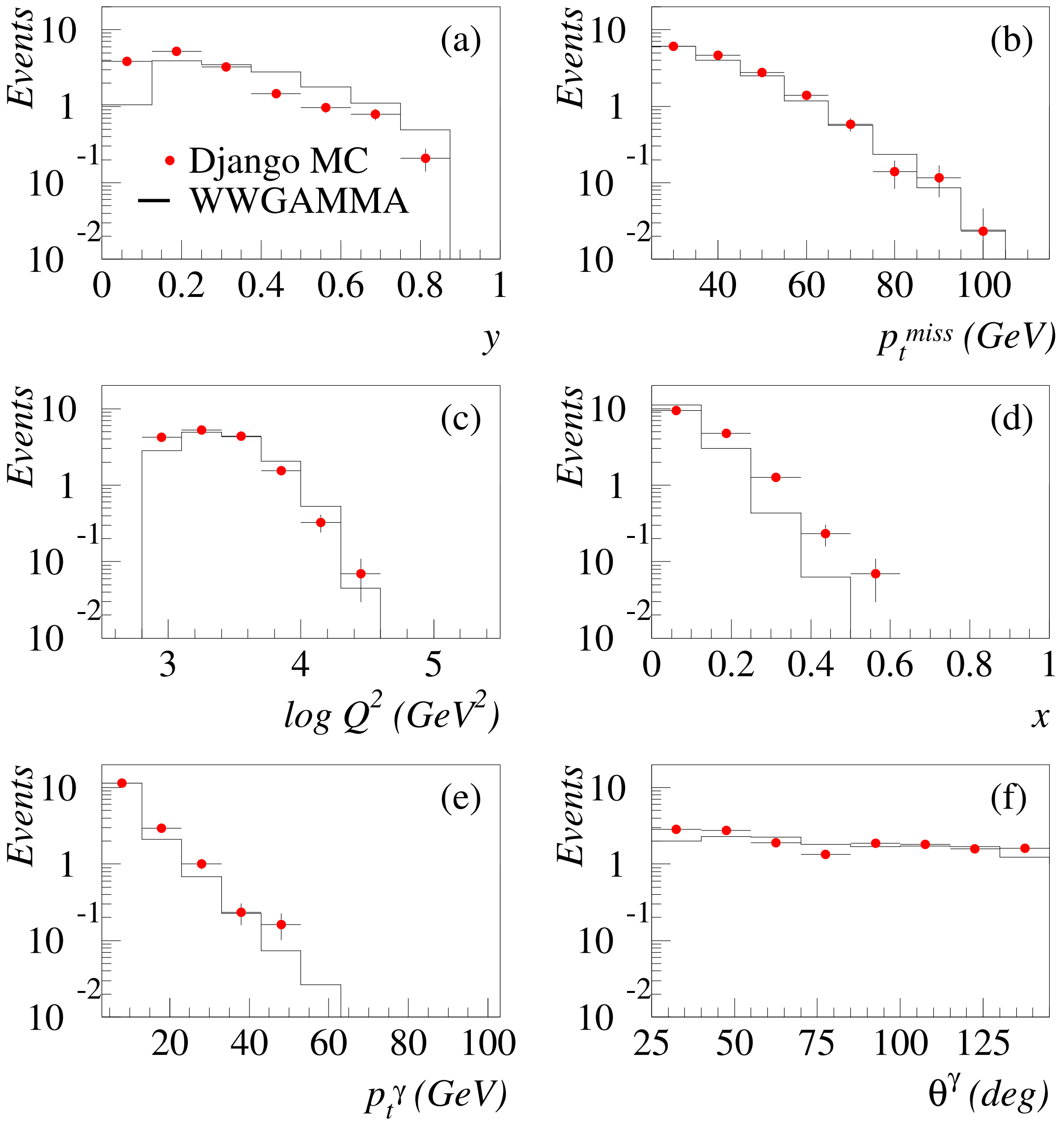

Figure 9.4: Comparison of `WWGAMMA` and `DJANGO` MCs. Both are normalised to the luminosity of data sample **C**. `DJANGO` is represented by the red points and `WWGAMMA` by the solid black line for (a) y, (b) p_t^{miss}, (c) $\log Q^2$, (d) x, (e) p_t^{γ} and (f) θ^{γ}. All distributions agree well with respect to the expected number of events, but the x and y distributions are seen to differ in overall shape.

9.4 Variation of anomalous couplings

In order to assess the agreement of the cross section results with the Standard Model expectation it is possible to vary the effect of the anomalous couplings, $\Delta\kappa$ and λ, on the predicted cross sections given by the `WWGAMMA` MC. The Standard Model values for these parameters are:

$$\kappa = 1 \qquad (\Delta\kappa = \kappa - 1) \qquad\qquad \lambda = 0. \tag{9.2}$$

These values have been measured by other HEP experiments and the current averages from LEP are [52]:

$$\Delta\kappa = 0.04 \pm 0.08 \qquad\qquad \lambda = -0.04 \pm 004. \tag{9.3}$$

In figures 9.5 and 9.6 the predictions for the radiative CC distributions are given, using the luminosity, beam energies and types relating to the conditions of data set **C**. The SM values of κ and λ are represented by the black histogram, and altered values of these couplings are represented by the circles and triangles in each case. The distributions plotted in figures 9.5 and 9.6 are (a) the inelasticity y, (b) the missing transverse momentum p_t^{miss}, (c) log Q^2, (d) the fraction of the momentum carried by struck quark x, (e) the transverse momentum of the photon p_t^γ and (f) the polar angle of the photon θ^γ.

From this study, using the `WWGAMMA` generator MC, it can be seen that differences in these couplings can only be observed in the p_t^γ spectrum at high values of p_t^γ. From the scale of these differential plots it can be deduced that, in order to observe a change in the measurement due to anomalous couplings, an increase of the luminosity by 2 orders of magnitude on this data set is required. Hence, this is an interesting study for future consideration at HERA (see chapter 10), but makes the measurement of any anomalous couplings virtually impossible with the data available.

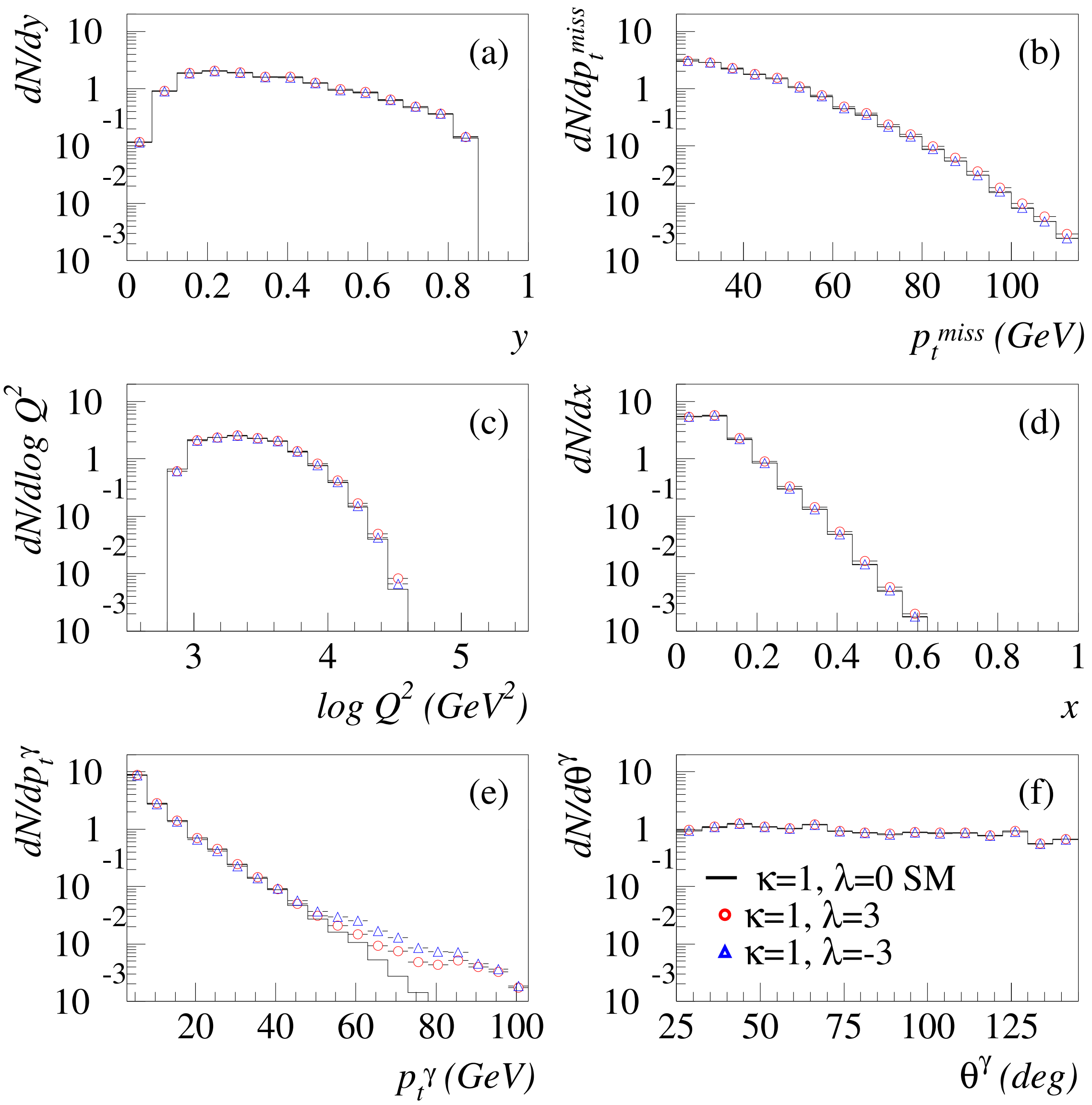

Figure 9.5: Plots showing the predictions for different values of λ. The Standard Model prediction (κ=1, λ=0) is the solid black line, λ=3 the red open points and $\lambda = -3$ the open blue triangles. Plot (a) shows the dN/dy distribution, (b) dN/dp_t^{miss}, (c) dN/d$logQ^2$, (d) dN/dx, (e) dN/dp_t^γ and (f) dN/dθ^γ. No significant variations are seen in the distributions, other than in the dN/dp_t^γ plot where the anomalous couplings do induce an increase in the prediction at high p_t^γ.

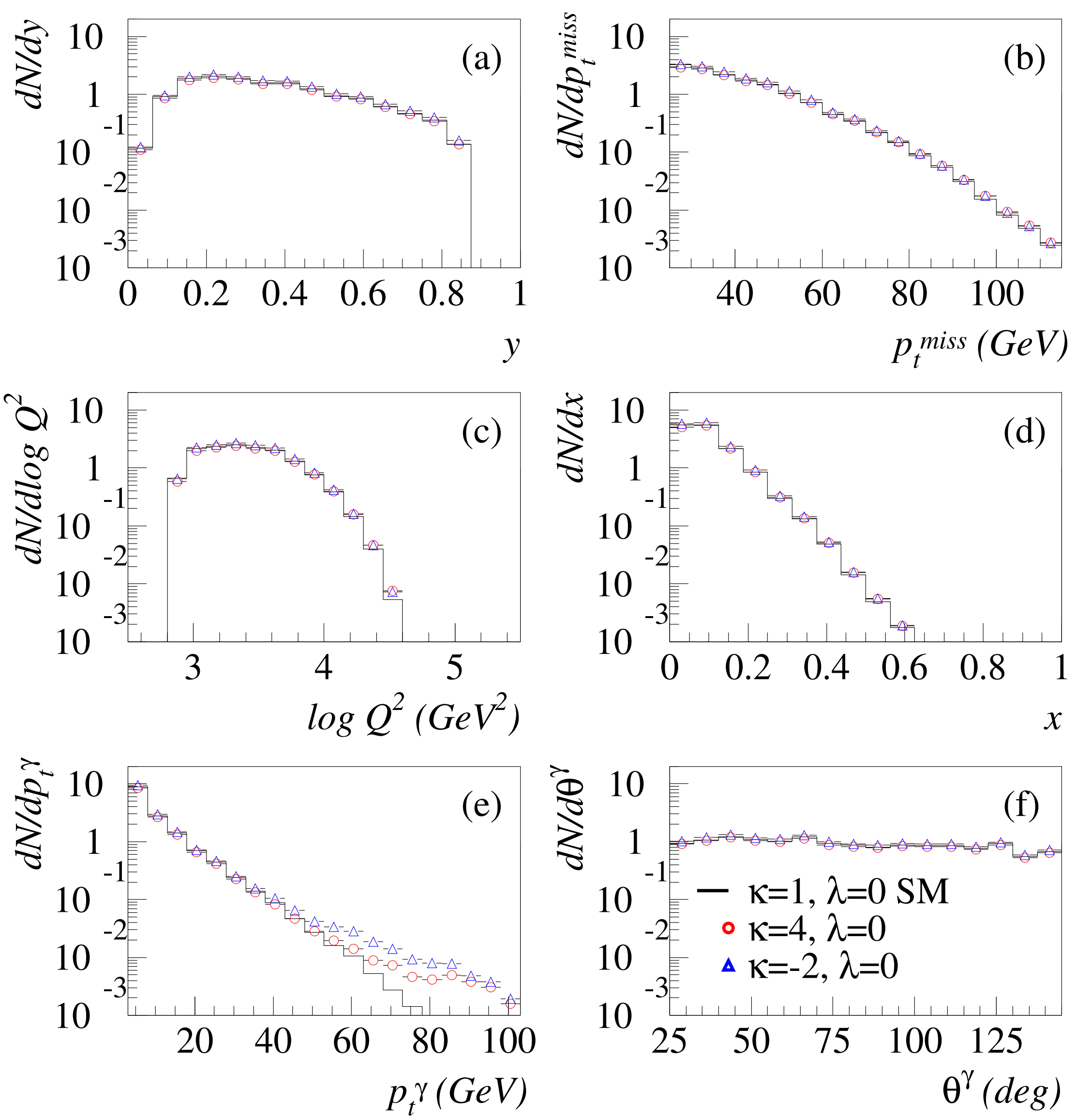

Figure 9.6: Plots showing the predictions for different values of κ. The Standard Model prediction (κ=1, λ=0) is the solid black line, κ=4 the red open points and $\kappa = -2$ the open blue triangles. Plot (a) shows the $\mathrm{d}N/\mathrm{d}y$ distribution, (b) $\mathrm{d}N/\mathrm{d}p_t^{miss}$, (c) $\mathrm{d}N/\mathrm{d}logQ^2$, (d) $\mathrm{d}N/\mathrm{d}x$, (e) $\mathrm{d}N/\mathrm{d}p_t^{\gamma}$ and (f) $\mathrm{d}N/\mathrm{d}\theta^{\gamma}$. Again, no significant variations are seen in the distributions, other than in the $\mathrm{d}N/\mathrm{d}p_t^{\gamma}$ plot where the anomalous couplings do induce an increase in the prediction at high p_t^{γ}.

Chapter 10

Summary and Outlook

Measurements have been made at the H1 experiment at HERA of the charged current cross sections and the radiative CC cross sections. These measurements have been made for different beam energies and lepton types, and the results have been compared with each other and with the Standard Model expectation. In neither analysis has any evidence been found of unexpected behaviour due to processes beyond those in the Standard Model.

For the CC analysis, it has been established that the cross sections agree very well with the SM prediction. The differences in the magnitude of the cross sections for the different lepton beam types have been established.

The radiative CC cross section has been measured for the first time at HERA and has been compared to the `DJANGO` MC, which is known not to contain the full set of matrix elements required to fully describe the radiative CC processes (including initial and final state radiation, and the radiation of the photon from the W). However, this MC does give a reasonable description of the data. The `WWGAMMA` MC was also used as a comparison in order to enable examination of the anomalous couplings $\Delta\kappa$ and λ which contribute to the triple-boson $WW\gamma$ vertex. The predicted cross sections have been calculated using different values of these anomalous couplings and it has been shown that in order to measure any appreciable difference in the couplings from those given by the SM at HERA with this process, it would be necessary for H1 to accumulate at least a factor of 30 more data than it presently has in total.

This leads to the future upgrade of HERA and the H1 experiment which is due to take place in the shutdown period from mid-2000 until mid-2001 [53]. During this upgrade HERA will have new superconducting focussing magnets installed which will increase the luminosity available to the experiments by a factor of ~ 3 per year on that available in the 1999 - 2000 running period, design specifications predicting at least 150 pb^{-1} per year. Eventually, this upgrade will allow the radiative CC analysis to be repeated with a much higher statistical accuracy and the determination of the anomalous coupling constants will become considerably more feasible.

In addition to the luminosity upgrade, a polarisation of the lepton beam is proposed. This will allow the observation of the effect of this on the CC cross section [54]. Only left-handed neutrinos (or right-handed antineutrinos) are believed to couple to charged leptons by the weak interaction; it is believed that neutrinos only interact by the weak interaction. Therefore, for a polarised incoming lepton beam of one helicity the CC cross section will be reduced to nothing, whilst for the other, the CC cross section should be enhanced with respect to the value presented here.

The prospects for physics at HERA*II* are interesting and bring the possibility of producing statistically enhanced and increasingly accurate measurements, whilst allowing the fields of exploration to open further within this unique environment.

Appendix A

Final Radiative CC Event Sample.

The following table A contains details of all 22 events radiative CC events in the final sample for the combined data sets.

Run no.	**Event no.**	p_t^{miss}(GeV)	**log**Q^2(GeV^2)	p_t^γ(GeV)	θ^γ(deg)	ϕ^γ(deg)
84025	219676	42.56	3.565	3.91	140.7	48.3
157185	179335	30.32	3.132	9.40	77.6	43.2
184613	50022	29.08	3.007	12.67	51.1	-10.5
236908	2491	108.42	4.247	4.34	31.5	-6.8
240165	18125	77.10	4.037	7.44	50.9	91.6
240741	154573	50.39	3.563	3.00	61.0	-91.6
251117	32981	80.54	4.033	3.82	124.2	69.8
254476	8025	55.27	3.682	10.87	67.1	-66.2
256762	113907	54.17	3.653	5.16	73.1	-95.2
258035	170995	28.83	3.285	3.46	128.6	120.6
259267	10503	48.44	3.499	3.31	66.7	-95.1
259283	190888	25.53	3.170	4.32	91.0	14.5
263857	16266	33.09	3.795	3.89	45.0	-154.5
265041	10580	28.34	3.054	3.09	73.6	29.0
265530	14193	27.90	3.159	6.70	86.2	-10.2
269537	473	65.05	3.899	10.91	64.0	-175.0
270150	49092	30.81	3.174	6.91	97.1	29.5
274358	31640	72.37	3.955	11.24	26.7	76.1
275354	11031	27.94	3.631	7.33	126.5	160.8
275617	70056	70.32	3.893	3.09	52.9	51.4
277258	122669	68.45	3.836	4.69	28.9	41.1
277544	124901	60.58	3.939	16.24	94.9	-65.6

Table A.1: Events passing full radiative CC selection.

References

[1] M. Breidenbach et al., Phys. Rev. Lett. 23 (1969) 935.

[2] H1 Collab., T. Ahmed et al., Phys. Lett. B299 (1993) 385.

[3] H1 Collab., I. Abt et al., Nucl. Phys. B407 (1993) 515.

[4] ZEUS Collab., M. Derrick et al., Phys. Lett. B316 (1993) 412.

[5] H1 Collab., T. Ahmed et al., Nucl. Phys. B439 (1995) 471.

[6] ZEUS Collab., M. Derrick et al., Z. Phys. B470 (1995) 379.

[7] D.E. Groom et al., 'The Z Boson', Eur. Phys. J. C15 1 (2000).

[8] D.E. Groom et al., 'The Mass of the W Boson', Eur. Phys. J. C15 1 (2000).

[9] H1 Collab., 'Inclusive Measurement of Deep Inelastic Scattering at high Q^2 in Positron-Proton Collisions at HERA', submitted to ICHEP 2000, Osaka, Japan.

[10] J. Englelen, M. Klein and R. Rückl, Proceedings of the 'Physics at HERA' Workshop, volume 1, editors W. Buchmüller and G. Ingleman, DESY (1991) 19.

[11] J. Friedman and H. Kendall, 'Deep Inelastic Electron Scattering' Ann. Rev. Nucl. Part. Sci. 22 (1972) 203-254 and references therein.

[12] J. Feltesse, Proceedings of the Lepton Photon Conference 1989, SLAC, editor M. Riordan, (1989) 13 and references therein.

[13] NMC Collab., P. Amaudruz et al., 'Measurements of R(D) - R(P) and R(CA) - R(C) in deep inelastic muon scattering', Phys. Lett. B294 (1992) 120.

[14] H1 Collab., S. Aid et al., Nucl. Phys. B470 (1996) 3.

[15] Y.L. Dokshitzer, Sov. Phys., JETP 46 (1977) 641,
V.N. Gribov and L.N. Lipatov, Sov. J. Nucl. Phys. 15 (1972) 438 and 675,

G. Altarelli and G. Parisi, Nucl. Phys. B126 (1977) 297,
G. Curci, W. Furmanski and R. Petronzio, Nucl. Phys. B175 (1980) 27,
W. Furmanski and R. Petronzio, Phys. Lett. B97 (1980) 437.

[16] T. Helbig and H. Spiesberger, 'Testing anomalous WWγ couplings in radiative charged current ep scattering', Nuc. Phys. B373 (1992) 73.

[17] H. Aihara et al., 'Anomalous Gauge Boson Interactions', HEP-PH-9503425 (1995).

[18] W. Buchmüller, D. Haidt and W. Hollik, Proceedings of the 'Physics at HERA' Workshop, volume 2, editors W. Buchmüller and G. Ingleman, DESY (1991) 919.

[19] T. Helbig and H. Spiesberger, Proceedings of the 'Physics at HERA' Workshop, volume 2, editors W. Buchmüller and G. Ingleman, DESY (1991) 973.

[20] V.A. Noyes, Proceedings of the workshop on 'Future Physics at HERA', volume 1, editors G. Inglemann, A. De Roeck and R. Klanner, DESY (1996) 190.

[21] H1 Collab., 'W production in ep collisions at HERA', submitted to ICHEP 2000, Osaka.

[22] T. Carli, P. Dingus and Y. Sirois, Proceedings of the 'Physics at HERA' Workshop, volume 2, editors W. Buchmüller and G. Ingleman, DESY (1991) 1112.

[23] H1 Collab., 'A Search for Excited Neutrinos in e^-p Collisions at HERA', submitted to ICHEP 2000, Osaka.

[24] V. Ruhlmann-Kleider, 'New Particle Searches', Int. J. Mod. Phys. : 15 (2000) no.Suppl.1B.

[25] H1 Collab., 'Luminosity Measurement in the H1 Experiment at HERA', submitted to ICHEP'96, Warsaw.

[26] H1 Collab., 'The H1 Detector at HERA', DESY-H1-96-01.

[27] B. Heinemann, Thesis: 'Measurement of Charged Current and Neutral Current Cross Sections in Positron-Proton Collisions at $\sqrt{s} \simeq 300$ GeV', (1999).

[28] A. Schöning, Thesis: 'Untersuchung von Prozessen mit virtuellen und reellen W± -Bosonen am H1-Detektor bei HERA', (1996).

[29] B. Reisert and Th. Schörner, 'TTNT An ntuples interface for the LAr trigger software package TTOOL', H1-500-583 (2000).

[30] A. Mehta, Thesis: 'Measurement of the Diffractive Proton Structure Function and Calibration of the Forward Muon Detector at H1', (1994).

[31] H1 Collab., I. Abt et al., Z. Phys., C66 (1995) 529.

[32] H1 Calorimeter Group, B. Andrieu et al., Nucl. Instr. Meth. A336 (1993) 460.

[33] H. P. Wellish et al., MPI-PhE / 94-03 (1994).

[34] U. Bassler and G. Bernardi, Z. Phys. C76 (1997) 223.

[35] A. Blondel and F. Jaquet, 'Proceedings of the study of an *ep* Facility for Europe', editor U. Amaldi, DESY 79/48 (1979) 391.

[36] G.A. Schuler and H. Spiesberger, Proceedings of the 'Physics at HERA' Workshop, volume 3, editors W. Buchmüller and G. Ingleman, DESY (1991) 1419.

[37] A. Kwiatkowski, H. Spiesberger and H.-J. Mohr̈ing, Proceedings of the 'Physics at HERA' Workshop, volume 3, editors W. Buchmüller and G. Ingleman, DESY (1991) 1294.

[38] G. Ingleman, Proceedings of the 'Physics at HERA' Workshop, volume 3, editors W. Buchmüller and G. Ingleman, DESY (1991) 1366.

[39] T. Sjöstrand, Computer Physics Communicator 39(1986)347, *ibid* 43 (1987)367.

[40] T. Sjöstrand, Computer Physics Communicator 82(1991)71, CERN-TH-6188 (1992).

[41] H. Spiesberger, 'Monte carlo simulation of deep inelastic electron proton scattering including electroweak radiative effects', Proceedings of MC91, Amsterdam (1991) 539.

[42] P. Bate, Thesis: 'High Transverse Momentum 2-Jet and 3-Jet Cross Section Measurements in Photoproduction', (1999).

[43] H1 Collab., 'Measurement of Neutral and Charged Current Cross-Sections in Positron-Proton Collisions at Large Momentum Transfer', Eur. Phys. J. C13 (2000) 609.

[44] E. Chabert et al., H1 internal report, (1998) H1-11/98-556.

[45] Z. Zhang, Habilitation Thesis, LAL, (2000) LAL 00-57.

[46] H1 software package QESCAT.

[47] H1 Collab., 'Measurement of the charged and neutral current cross sections at HERA', submitted to EPS-HEP99, Tampere, Finland.

[48] H1 Collab., 'Measurement of Neutral and Charged Current Cross Sections in Electron-Proton Collisions at High Q^2', *to be submitted to* Eur. Phys. J. (2000).

[49] H. Spiesberger et al., Proceedings of the 'Physics at HERA' Workshop, volume 2, editors W. Buchmüller and G. Ingleman, DESY (1991) 798.

[50] D. Bardin, C. Burdik, P. Christova and T. Reimann, Z. Phys. C42 (1989) 679.

[51] B. Heinemann, S. Riess and H. Spiesberger, 'Radiative Corrections for Charged Current Scattering: A Comparison of Computer Codes', Proceedings of 1998/9 Workshop 'Monte Carlo Generators for HERA Physics', DESY-PROC-1999-02, ISSN 1435-8077 (1999) 530.

[52] LEP Collabs., 'Combined Preliminary Results on Electroweak Gauge Boson Couplings Measured by the LEP Experiments', LEPEWWG/TGC 2000-02 (2000).

[53] M. Seidel et al., 'Overview on the HERA Luminosity Upgrade Project', Proceedings of LP97, (1999).

[54] Jörg Gayler, 'HERA Beyond Year 2000', writeup of talk given at Hadron Structure 98, Slovakia, (1998).

Acknowledgements

I would like to thank many people for their help and support in the production of this thesis and the work which went into it.

Firstly, to my supervisors: Professor Erwin Gabathuler who directed me towards this field of study at the start and then allowed me the freedom to find my own subject within it; Dr. Tim Greenshaw who kept me on track throughout and made sure this thesis made sense at the end (although any mistakes are still mine, not his!). Also to Professor John Dainton for his interest and encouragement during my time in Hamburg and beyond. Financial support was provided by PPARC from October 1997 until October 2000, and subsequently by the University of Liverpool. Thanks to those who were instrumental in securing this funding.

I'm greatly indebted to the friends who I spent my time working with and learning from in Hamburg: Andy Mehta, Eram Rizvi and Beate Heinemann. Their patience and enthusiam has been unwaning. Thanks also to the HiP group and those in the Liverpool H1 group who have coached and enlightened me on so many different aspects of physics analysis.

I must express my gratitude to my Bleicherstrasse housemates - Paul Bate, Rob Waugh, Nick Malden and Angela Wyatt - for all the fun we had partying and painting. Armageddon marked the end of an era, but it came and went remarkably peacefully, fortunately! Dave Milstead must be thanked for the hours spent in the office gossiping and honing my debating skills - it's been a pleasure to know someone so knowledgable! To my other good friends and office mates Gareth Hughes and Michael George for amusements, distractions and exchanges of angst!

The person who has kept me sane and happy - in difficult circumstances! - and who understands my fortes and shortcomings is Julian Phillips. It's been a pleasure to live and work with him during my time as a PhD student and beyond. My love, respect and thanks go to him.

My entire family deserves thanks for repeatedly reminding me that it'll all be worth it in the end! Finally, eternal love and infinite thanks to my parents. Without their support, energetic encouragement and total belief in me, I never would have even started, let alone finished, this doctorate.

How time flies when you're having fun....